

Differential cross sections and photon beam asymmetries
of η photoproduction on the proton at $E_\gamma = 1.3 - 2.4$ GeV

Toshikazu Hashimoto



A dissertation submitted in partial fulfillment of the requirements for
the degree of Doctor of Science
Department of Physics, Kyoto University
April, 2024

Abstract

The η meson photoproduction $\gamma N \rightarrow \eta N$ is a unique tool to investigate nucleon-excited states with large $s\bar{s}$ components. In the high-energy excited region, many excited states with broad widths overlap each other. In order to distinguish each contribution, it is necessary to measure both the photon beam asymmetry and the differential cross section. In recent experimental measurements, a bump structure in the differential cross section at $\cos\theta_{\text{c.m.}}^\eta < -0.6$ above $W = 2.1$ GeV was observed. It has not been determined, however, what's are responsible for this structure. Unfortunately, there exists no other beam asymmetry measurements in this energy region, and the contributions of multiple resonance states cannot be separated. To solve this problem, we carried out an experiment to investigate the single η meson photoproduction on the proton in the LEPS2 beamline at SPring-8. A linearly polarized photon beam was produced by the backward Compton scattering. The polarization was more than 70% above $W = 2.1$ GeV, making it suitable for precise measurement of photon beam asymmetry. Produced particles were measured using the egg-shaped electromagnetic calorimeter and forward trajectory detectors. The $\gamma p \rightarrow \eta p$ reaction was identified by selecting a proton and two γ 's produced from an $\eta \rightarrow \gamma\gamma$ decay. In order to reduce backgrounds, a kinematical fitting was performed. We measured the differential cross sections and photon beam asymmetries of η photoproduction on a proton in a center-of-mass energy W from 1.82 to 2.32 GeV and a polar angle range $\cos\theta_{\text{c.m.}}^\eta$ from -1.0 to 0.6 . We observed an enhancement of the differential cross section in $W = 2.0$ – 2.3 GeV in the backward angle of $\cos\theta_{\text{c.m.}}^\eta < -0.4$. This structure cannot be explained with any u -channel contributions, suggesting the existence of resonance states with high orbital angular momentum. This enhancement is only found in the η differential cross section, not in the π^0 and ω differential cross sections. Therefore the observed structure is likely to associate with the nucleon resonances having a large $s\bar{s}$ component and strongly couple to the ηN channel. We measured, for the first time, the photon beam asymmetries above $W = 2.1$ GeV. Our new data differed from the results of any partial wave analyses calculation. They provide an additional constraint to nucleon resonance studies at high energies.

Contents

1	Introduction	1
1.1	Overview of hadron spectroscopy	1
1.2	Quark model	2
1.2.1	Ground state of hadrons	3
1.2.2	Excited state of baryons	9
1.3	Meson photoproduction	15
1.3.1	Electro-magnetic multipole	19
1.3.2	CGLN amplitudes	20
1.4	Previous experiments	27
1.4.1	η meson photoproduction	27
1.4.2	Experimental status of η photoproduction	27
1.5	Present experiment	31
2	Experiment	37
2.1	SPring-8/LEPS2 facility	37
2.1.1	LEPS2 beamline	37
2.1.2	Backward Compton scattering	39
2.2	LEPS2/BGOegg experimental set up	41
2.2.1	Beam tagging counter	42
2.2.2	Upstream Veto counter	43
2.2.3	Target	43
2.2.4	BGOegg calorimeter	45
2.2.5	Inner plastic scintillator	45
2.2.6	Drift chamber	45
2.2.7	Resistive plate chamber	48
2.2.8	RF signal	49

2.3	Data acquisition system	49
2.3.1	Electronics	50
2.3.2	Trigger	51
2.4	Data summary	52
3	Data Analysis	55
3.1	Photon beam measurement	55
3.1.1	Tagger track reconstruction	55
3.1.2	Beam energy calibration	57
3.1.3	Tagging photon counting	58
3.1.4	Beam transmission	59
3.2	Reaction timing reference	61
3.3	Measurement of final-state particles	61
3.3.1	Reconstruction of particles with the BGOegg calorimeter	62
3.3.2	IPS charge identification	62
3.3.3	DC tracking	63
3.3.4	TOF measurement	63
3.4	Event selection	64
3.4.1	Outline of the event selection	64
3.4.2	Recoil electron track in the tagging system	65
3.4.3	No UpVeto hits	65
3.4.4	Two γ 's identification	67
3.4.5	Proton identification	68
3.4.6	Kinematic fit	70
3.5	Yield estimation with background subtraction	71
3.6	Geometrical acceptance	75
4	Results	77
4.1	Differential cross section $d\sigma/d\Omega$	77
4.1.1	Formalism of $d\sigma/d\Omega$	77
4.1.2	Systematic uncertainties of $d\sigma/d\Omega$	78
4.1.3	Energy distributions of $d\sigma/d\Omega$	79
4.1.4	Angular distributions of $d\sigma/d\Omega$	83
4.2	Photon beam asymmetry Σ	86

4.2.1	Formalism of Σ	86
4.2.2	Systematic uncertainties of Σ	86
4.2.3	Angular distributions of Σ	88
5	Discussion	91
5.1	Differential cross section enhancement in $W = 2.0\text{--}2.3$ GeV . . .	91
5.1.1	u -channel contribution	91
5.1.2	High-spin resonance contribution	92
5.1.3	Comparison with other meson photoproduction results .	92
5.2	Comparison with other experimental results and PWA solutions	94
5.2.1	Differential cross section	94
5.2.2	Photon beam asymmetry	98
5.3	Comparison with the existing PWA results	100
5.4	Jülich-Bonn calculation comparison	103
5.5	Future work	104
6	Summary	105
A	Helicity amplitude	110
B	SPring-8 filling pattern	115
C	Dead time correction	117
D	Photon energy measurement	118
E	Efficiencies	120
E.1	Tagger reconstruction efficiency	120
E.2	Showers contribution	120
E.3	IPS proton detection efficiency	121
E.4	DC track reconstruction efficiency	122
E.5	RPC reconstruction efficiency	122

Chapter 1

Introduction

1.1 Overview of hadron spectroscopy

A question of what matter is made of has been an ongoing mystery in physics. Historically, our understanding on matter has been developed by revealing its internal structure. After establishing the atomic structure, then Rutherford discovered a nucleus at the core of atom. The nucleus of the hydrogen atom discovered by Rutherford was called a proton. Later in 1932, Chadwick discovered a neutron, which was an electrically neutral particle and had slightly heavier mass than a proton. The protons and neutrons were called baryons. Mesons were introduced as the carrier of the "nuclear force" that couples protons and neutrons by Yukawa. Around 1950, accelerators were invented and led to the discovery of new baryons and mesons, which can no longer be regarded as the smallest unit of matter. In the course of classifying these particles, a fundamental particle called a "quark" was introduced, and quark model was proposed in which a baryon is composed of three quarks and a meson is composed of a quark-antiquark pair. Later, study of deep inelastic scattering (DIS) had revealed the internal structure of the proton and the existence of point particles (partons) in a proton was discovered. The partons were found to have same quantum numbers as the "quarks", and the quark picture was established. On the other hand, it was also found that the partons contributed only about half of the total momentum of the proton. The remaining momentum was thought to be carried by gluons, which mediate interactions between quarks. Quantum ChromoDynamics (QCD) was established as a theory to describe the dynamics

of the interaction between quarks and gluons. Quarks and gluons have quantum numbers called color. They have three degree of freedom: red, green, and blue. Only color singlet, which have no colors as a whole, exist in nature as hadrons. The interaction depends on the coupling constant of QCD α_S . The coupling of QCD depends on the energy scale of QCD; the larger the coupling constant, the more valid the perturbative picture becomes. The peculiarity in QCD is the asymptotic freedom of the coupling constant [1]. Namely, at higher energies, the perturbative picture holds better. On the other hand, at low energies, non-perturbative phenomena such as quark confinement dominated so that the coupling constant becomes large. The resulting composite particles of quarks and gluons are called hadrons.

1.2 Quark model

In general, hadrons are classified into baryons and mesons. Baryons are particles with half-integer spins; nucleons such as protons and neutrons are constituent particles of nuclei. Mesons are particles with integer spins; pions are thought to mediate the nuclear force that couple nucleons together. In order to understand the various patterns of baryons and mesons, the constituent quark model (CQM) was proposed. In such models, the effective degrees of freedom to describe each hadron are "constituent quarks" that have the same quantum numbers and different masses as the current quarks. In the CQM, baryons are composed of three quarks (qqq) and mesons are composed of quark-antiquark pairs ($q\bar{q}$). The basic properties of ground state hadrons, including their mass and magnetic moment, were successfully explained in this model. While this model can explain the ground state properties very well, the properties of excited states are not so easy to reproduce. There are some discrepancies between the model and the experimental observations for the excited states. In addition, quark many-body systems that cannot be classified as ordinary baryons (qqq) or ordinary mesons ($q\bar{q}$) in the quark model are discovered [62, 63, 64]. They are called exotic hadrons. Because QCD only requires quark many-body systems to be color singlet states, one type of exotic hadrons is considered to be a multi-quark state consisting of four or more quarks, a glueball (gg) consisting of only gluons, and a hybrid hadron ($q\bar{q}g$ or $qqqg$) consisting of quarks and glu-

ons. In order to understand the structure of exotic hadrons, hadron molecular structures, diquark correlations between two quark pairs inside hadrons, and gluons are newly considered as degrees of freedom other than the constituent quarks. Discovery of these particles, suggests a breakdown of the quark model. Nevertheless, at least hadrons in the ground state and low-lying excited states are well represented by the quark model, which can serve as a guideline for understanding hadrons. In this section, we will discuss how hadrons and mainly baryons have been understood in terms of the quark model.

1.2.1 Ground state of hadrons

In the CQM, ordinary baryons are composed of three quarks (qqq), and ordinary mesons are composed of quark-antiquark pairs ($q\bar{q}$). The quarks have six flavors (u, d, s, c, b, t). The quarks have quantum numbers such as charge Q , baryon number \mathfrak{B} , isospin I_3 , strangeness S , charm C , bottom B , and top T exhibited in Table 1.1.

Table 1.1: Quantum number of each quark.

quarks	charge Q	baryon number \mathfrak{B}	isospin I_3	strangeness S	charm C	bottom B	top T
u	+2/3	+1/3	+1/2	0	0	0	0
d	-1/3	+1/3	-1/2	0	0	0	0
s	-1/3	+1/3	0	-1	0	0	0
c	+2/3	+1/3	0	0	1	0	0
b	-1/3	+1/3	0	0	0	-1	0
t	+2/3	+1/3	0	0	0	0	1

The following relationship holds between these quantum numbers.

$$Q = I_3 + \frac{\mathfrak{B} + S + C + B + T}{2} \quad (1.1)$$

In the discussion that follows, only u, d, and s are treated as flavors of quarks.

Mesons

Mesons are $q\bar{q}$ states. Under the flavor SU(3) symmetry, the $q\bar{q}$ state is represented as a singlet and an octet, as shown in Eq. 1.2,

$$3 \otimes \bar{3} = 1 \oplus 8. \quad (1.2)$$

Because both the quark spin and antiquark spin are $1/2$, a ground-state meson with $q\bar{q}$ in the S wave have a spin of 0 or 1. A ground-state meson with spin 0 is called a pseudoscalar meson and a ground-state meson with spin 1 is called a vector meson. Table 1.2 lists $q\bar{q}$ representations with three flavors, the corresponding light mesons with quantum numbers. Fig. 1.1 shows pseudoscalar mesons in the Y - I_3 space, and Fig. 1.2 does vector mesons. Here, the hypercharge Y is simply given by $Y = \mathfrak{B} + S$, since we are here considering three flavors, u, d, and s. This is simply to align the center of the multiplet with the origin. We have three states where $(I_3, Y) = (0, 0)$, and these are the mixed states of $u\bar{u}$, $d\bar{d}$, and $s\bar{s}$.

 Table 1.2: $q\bar{q}$ representations with three flavors and the corresponding mesons.

quarks	spin	isospin I_3	hypercharge Y	meson
$u\bar{s}$	0	+1/2	+1	K^+
$d\bar{s}$	0	-1/2	+1	K^0
$u\bar{d}$	0	+1	0	π^+
$u\bar{u}, d\bar{d}, s\bar{s}$	0	0	0	π^0, η_8, η_0
$d\bar{u}$	0	-1	0	π^-
$s\bar{d}$	0	+1/2	-1	\bar{K}^0
$s\bar{u}$	0	-1/2	-1	K^-
$u\bar{s}$	1	+1/2	+1	K^{*+}
$d\bar{s}$	1	-1/2	+1	K^{*0}
$u\bar{d}$	1	+1	0	ρ^+
$u\bar{u}, d\bar{d}, s\bar{s}$	1	0	0	$\rho^0, \omega_8, \omega_0$
$d\bar{u}$	1	-1	0	ρ^-
$s\bar{d}$	1	+1/2	-1	\bar{K}^{*0}
$s\bar{u}$	1	-1/2	-1	K^{*-}

We consider the example of pseudoscalar 0^- mesons. The SU(3) singlet η_0 has three flavors in equal proportion. Since π^0 has no $s\bar{s}$ contents, and the remaining η_8 is orthogonal to these, their wavefunction is represented in the

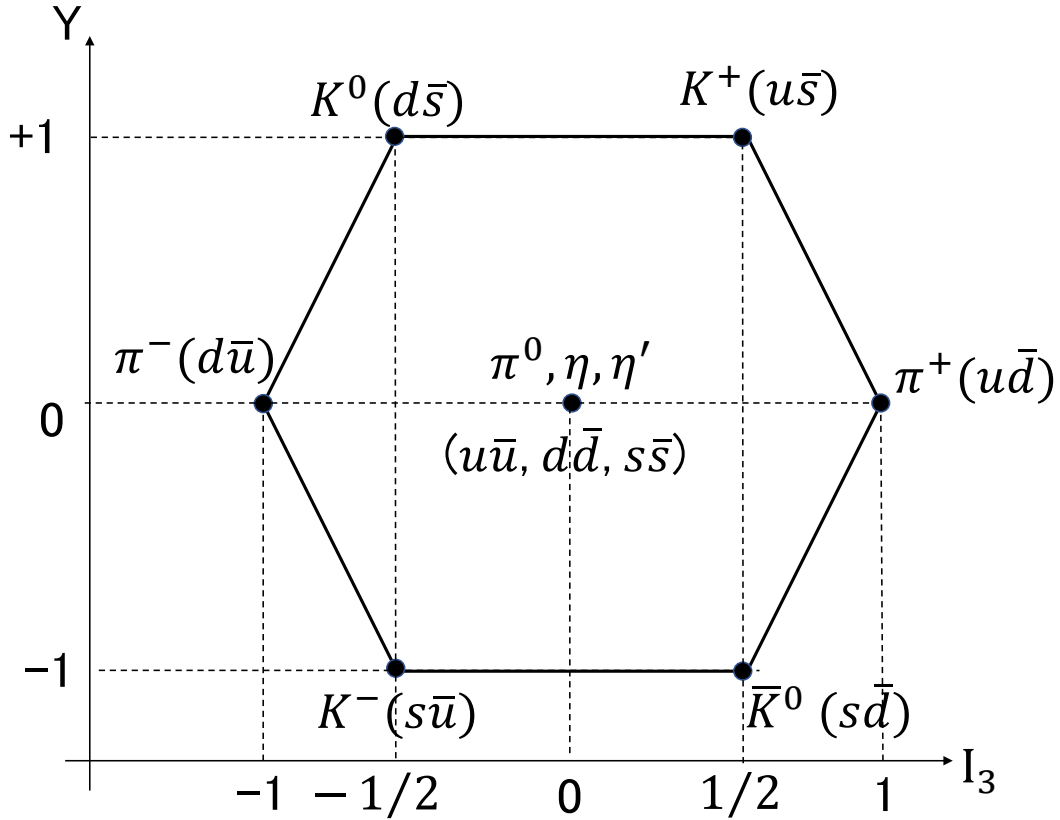


Figure 1.1: Ground states with pseudoscalar 0^- meson.

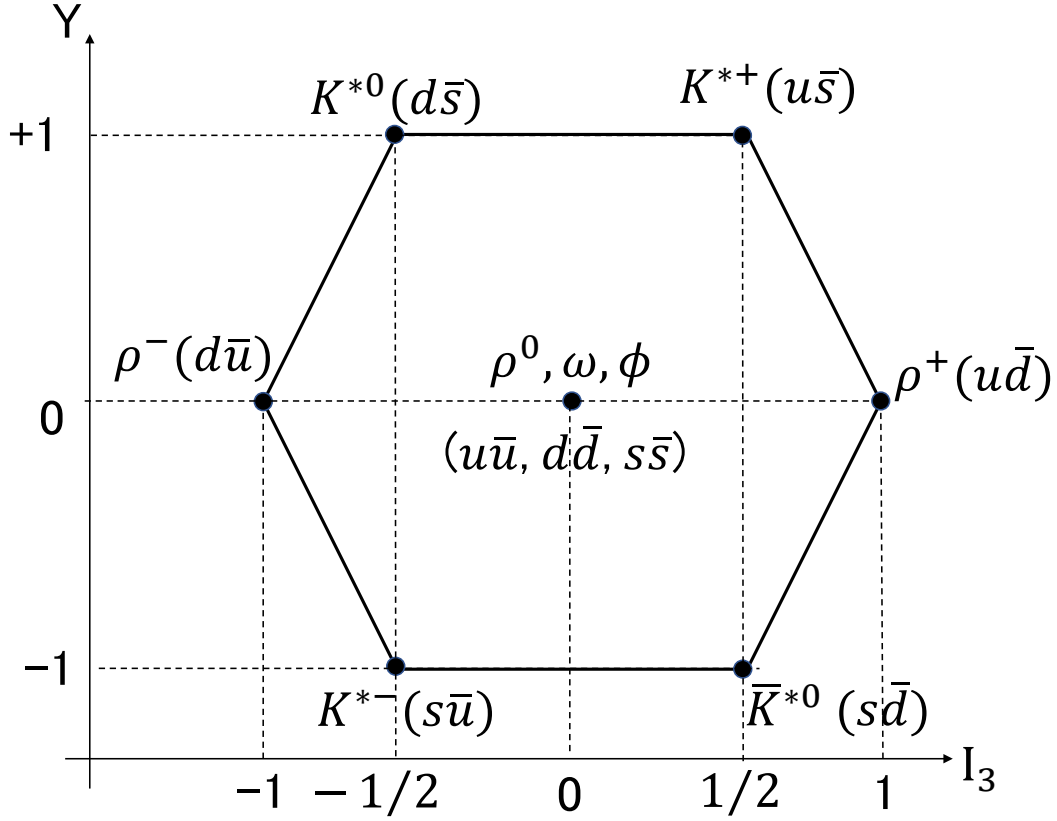
following equations:

$$\begin{aligned}
 |\pi^0\rangle &= \frac{1}{\sqrt{2}}(|u\bar{u}\rangle - |d\bar{d}\rangle), \\
 |\eta_8\rangle &= \frac{1}{\sqrt{6}}(|u\bar{u}\rangle + |d\bar{d}\rangle - 2|s\bar{s}\rangle), \\
 |\eta_0\rangle &= \frac{1}{\sqrt{3}}(|u\bar{u}\rangle + |d\bar{d}\rangle + |s\bar{s}\rangle).
 \end{aligned} \tag{1.3}$$

Since the flavor $SU(3)$ is an approximate symmetry, which is broken in different masses of quarks, the physical η and η' are mixtures of η_0 and η_8 .

$$\begin{aligned}
 |\eta\rangle &= \cos\theta_P|\eta_8\rangle - \sin\theta_P|\eta_0\rangle, \\
 |\eta'\rangle &= \sin\theta_P|\eta_8\rangle + \cos\theta_P|\eta_0\rangle,
 \end{aligned} \tag{1.4}$$

where $\theta_P = -11.3^\circ$ is the mixing angle of η_0 and η_8 [2]. The mixing angles are small, and $\eta(\eta')$ corresponds almost purely to $\eta_8(\eta_0)$ in the flavor $SU(3)$.


 Figure 1.2: Ground state with vector 1^- meson.

The vector 1^- mesons can be similarly expressed as follows:

$$\begin{aligned}
 |\rho^0\rangle &= \frac{1}{\sqrt{2}}(|u\bar{u}\rangle - |d\bar{d}\rangle), \\
 |\omega_8\rangle &= \frac{1}{\sqrt{6}}(|u\bar{u}\rangle + |d\bar{d}\rangle - 2|s\bar{s}\rangle), \\
 |\omega_0\rangle &= \frac{1}{\sqrt{3}}(|u\bar{u}\rangle + |d\bar{d}\rangle + |s\bar{s}\rangle), \\
 |\phi\rangle &= \cos\theta_V|\omega_8\rangle - \sin\theta_V|\omega_0\rangle, \\
 |\omega\rangle &= \sin\theta_V|\omega_8\rangle + \cos\theta_V|\omega_0\rangle,
 \end{aligned} \tag{1.5}$$

where $\theta_V = 39.2^\circ$ is the mixing angle of ω_0 and ω_8 [2]. Since $\sin\theta_V$ is almost $\sqrt{3}$, the ϕ meson is considered to be almost pure $s\bar{s}$ state, and the ω meson is considered to be mixed state of $u\bar{u}$ and $d\bar{d}$ only. This is called ideal mixing.

Baryons

Baryons are composed of qqq states in the CQM. The qqq states are represented in terms of the flavor $SU(3)$ symmetry as in Eq. 1.6,

$$3 \otimes 3 \otimes 3 = 10_S \oplus 8_{MS} \oplus 8_{MA} \oplus 1_A. \quad (1.6)$$

Using the notations S, A, MS, and MA for symmetric, antisymmetric, mixed symmetric, and mixed antisymmetric states, the subscript indicates the symmetry property of the wavefunction. S denotes states that are symmetric under the exchange of any two quarks, while A denotes states that are antisymmetric under such exchange. MS and MA are categorized as symmetric and antisymmetric, respectively, under the exchange of the first and second quarks.

Baryon wave function is expressed as products of flavor $SU(3)$ and spin $SU(2)$ in the quark model. The spin component of the ground state of a baryon composed of three quarks with spin $1/2$ is represented in the following equation,

$$2 \otimes 2 \otimes 2 = 4_S \oplus 2_{MA} \oplus 2_{MS}. \quad (1.7)$$

Taking the flavor $SU(3)$ and combining it with the spin $SU(2)$, we can form $SU(6)$.

$$6 \otimes 6 \otimes 6 = 56_S \oplus 70_{MS} \oplus 70_{MA} \oplus 20_A. \quad (1.8)$$

These supermultiplets decompose under the flavor $SU(3)$ into

$$56_S = {}^4 10 \oplus {}^2 8, \quad (1.9)$$

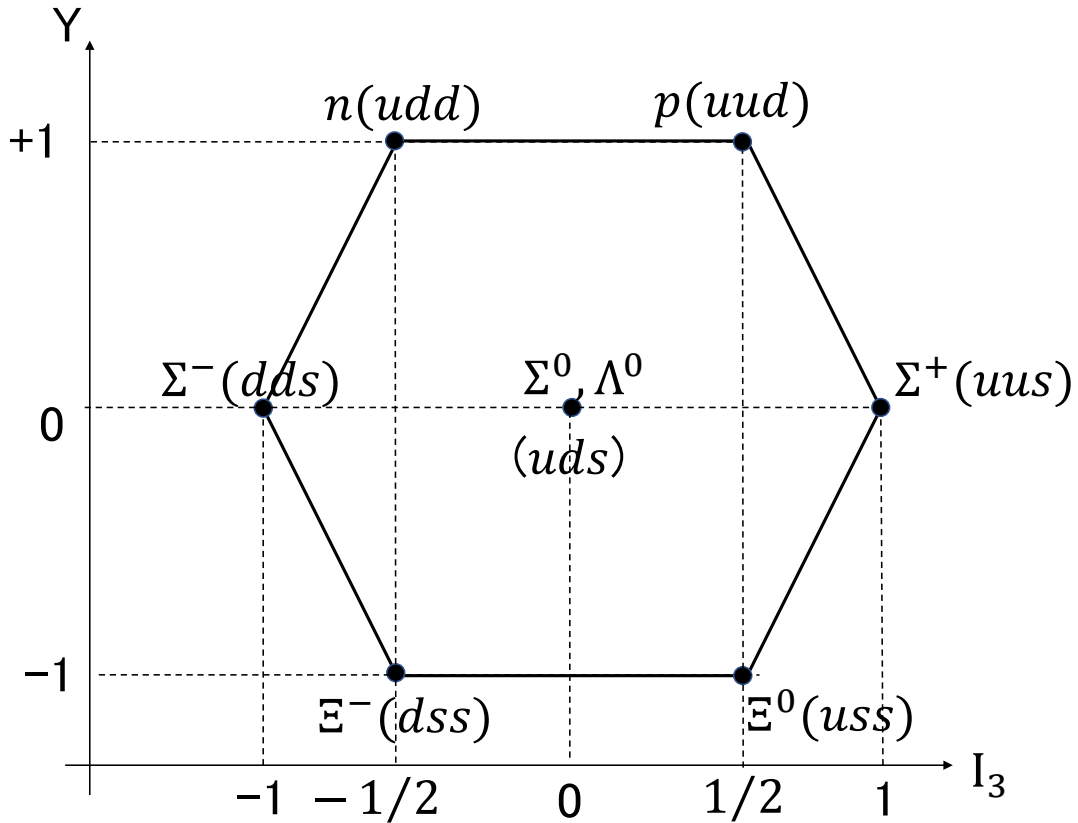
$$70_{MS,MA} = {}^2 10 \oplus {}^4 8 \oplus {}^2 8 \oplus {}^2 1, \quad (1.10)$$

$$20_A = {}^2 8 \oplus {}^4 1, \quad (1.11)$$

where the subscripts are $2S+1$ with the spin S of the baryon. The wavefunction of the ground-state baryons must be symmetric, therefore, these baryons belong to $\mathbf{56}$ and are classified into the $S = 1/2$ octet and the $S = 3/2$ decuplet. Table 1.3 lists the ground-state baryons with spins of $1/2$ and $3/2$, and Fig. 1.3 and 1.4 show the $Y - I_z$ two dimensional plots for them.

Table 1.3: qqq representation with three flavors and the corresponding baryons.

quarks	spin	isospin I_z	hypercharge Y	baryon
uud	$1/2$	$+1/2$	$+1$	p
udd	$1/2$	$-1/2$	$+1$	n
uus	$1/2$	$+1$	0	Σ^+
uds	$1/2$	0	0	Σ^0, Λ_0
dds	$1/2$	-1	0	Σ^-
uss	$1/2$	$+1/2$	-1	Ξ^0
dss	$1/2$	$-1/2$	-1	Ξ^-
uuu	$3/2$	$+3/2$	$+1$	Δ^{++}
duu	$3/2$	$+1/2$	$+1$	Δ^+
ddu	$3/2$	$-1/2$	$+1$	Δ^0
ddd	$3/2$	$-3/2$	$+1$	Δ^-
uus	$3/2$	$+1$	0	Σ^{+*}
uds	$3/2$	0	0	Σ^{0*}
dds	$3/2$	-1	0	Σ^{-*}
uss	$3/2$	$+1/2$	-1	Ξ^{0*}
dss	$3/2$	$-1/2$	-1	Ξ^{-*}
sss	$3/2$	0	-2	Ω^-


 Figure 1.3: Baryon ground states with $S = 1/2$ octet.

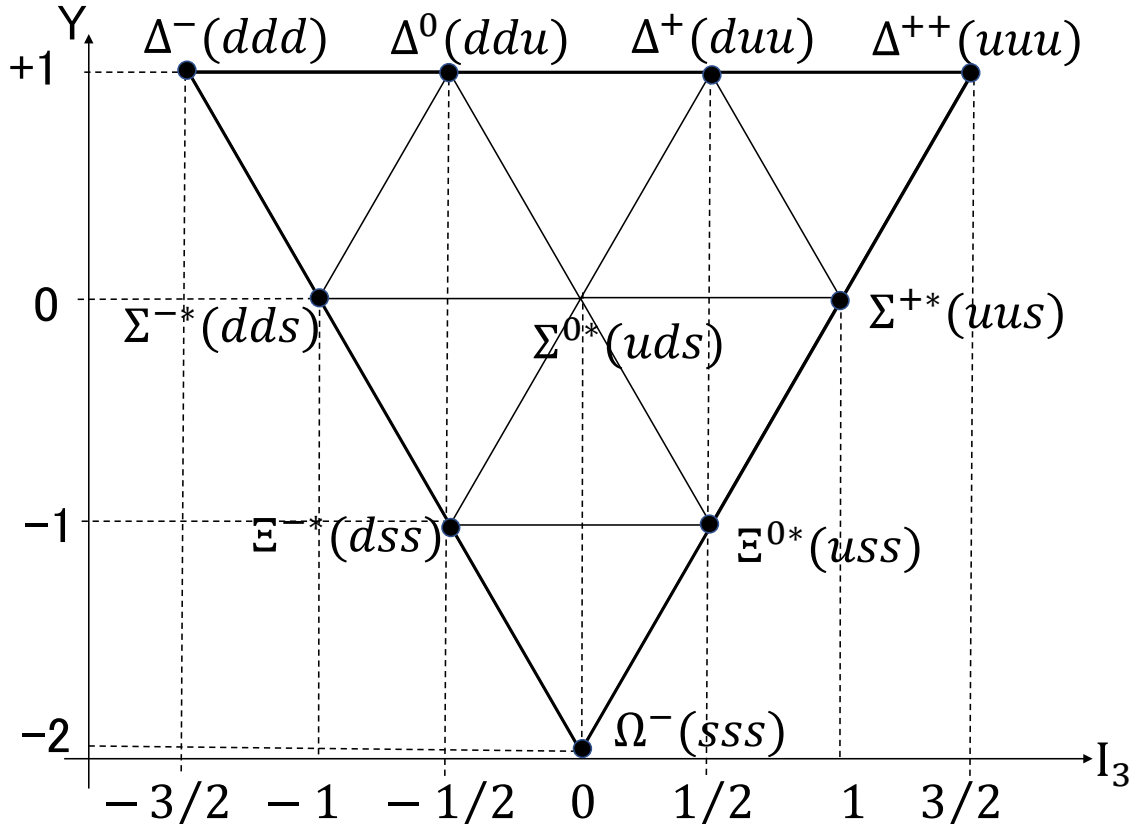


Figure 1.4: Baryon ground states with $S = 3/2$ decuplet.

1.2.2 Excited state of baryons

Now we get ground state baryon of octet and decuplet with $L = 0$. Next, we consider that baryon excitation is caused by orbital excitation of constituent quarks in a harmonic oscillator potential. At this time the quarks have orbital angular momentum L . The total angular momentum of the system $J = L + S$, which is obtained by combining the total spin of the three quarks S with L , is the total spin of baryons. The orbital excitation is represented under $O(3)$. The full symmetry group structure of the quarks in a potential is $SU(6) \times O(3)$. The Hamiltonian of the quarks is:

$$\hat{H} = \left(-\frac{\hbar^2}{2m} \nabla^2 + \frac{1}{2} m \hat{r}^2 \omega^2 \right) \quad (1.12)$$

where m is the mass of quarks, \hat{r} is the position operator, and ω is the angular frequency of the oscillator. The time-independent Schrödinger equation is:

$$\hat{H} \psi_{nlm} = E_{nlm} \psi_{nlm} \quad (1.13)$$

where ψ_{nlm} is the wavefunction, and E_{nlm} is the energy eigenvalue. They are described by using the principal quantum number $n = 0, 1, \dots$, angular momentum $l = 0, 1, 2, \dots$, and magnetic quantum number $m = -l, -l + 1, \dots, +l$. The energy eigenvalue E_{nlm} is represented in the following equation:

$$E_{nlm} = \left(2n + l + \frac{3}{2}\right) \hbar\omega. \quad (1.14)$$

The wavefunction ϕ_{nlm} can be separated as follows:

$$\psi_{nlm} = R_{nl}(r)Y_{lm}(\theta, \phi) \quad (1.15)$$

where $R_{nl}(r)$ is radial wavefunction, and $Y_{lm}(\theta, \phi)$ is spherical harmonics. The radial wavefunction can be expressed by using modified Laguerre polynomial functions

$$L_n^\alpha(x) = \frac{e^x x^{-\alpha}}{n!} \frac{d^n}{dx^n} (e^{-x} x^{n+\alpha}) \quad (1.16)$$

and a harmonic oscillator parameter $b = \sqrt{\hbar/m\omega}$ as follows

$$R_{nl}(r) = (-1)^n \sqrt{\frac{2\Gamma(n+1)}{\Gamma(n+l+3/2)}} \left(\frac{r}{b}\right)^l L_n^{l+1/2}\left(\frac{r^2}{b^2}\right) \exp\left(-\frac{r^2}{2b^2}\right) \quad (1.17)$$

The single-particle wavefunctions are

$$\begin{aligned} R_{00}(r) &= 2\pi^{-1/4} \exp\left(-\frac{r^2}{2b^2}\right), \\ R_{01}(r) &= 2\sqrt{\frac{2}{3}}\pi^{-1/4} \frac{r}{b} \exp\left(-\frac{r^2}{2b^2}\right) = \sqrt{\frac{2}{3}} \frac{r}{b} R_{00}(r), \\ R_{02}(r) &= 4\sqrt{\frac{1}{15}}\pi^{-1/4} \frac{r^2}{b^2} \exp\left(-\frac{r^2}{2b^2}\right) = \sqrt{\frac{4}{15}} \frac{r^2}{b^2} R_{00}(r), \\ R_{10}(r) &= 2\sqrt{\frac{2}{3}}\pi^{-1/4} \left(\frac{r^2}{b^2} - \frac{3}{2}\right) \exp\left(-\frac{r^2}{2b^2}\right) = \sqrt{\frac{2}{3}} \left(\frac{r^2}{b^2} - \frac{3}{2}\right) R_{00}(r), \end{aligned} \quad (1.18)$$

for $1s$ orbit ($n = 0, l = 0$), $1p$ orbit ($n = 0, l = 1$), $1d$ orbit ($n = 0, l = 2$) and $2s$ orbit ($n = 2, l = 0$).

First excitation band

In the ground-state hadrons in the CQM, each of the three quarks occupy the (1s) states in a harmonic oscillator potential, giving the orbital angular momentum $L = 0$ and the parity $P = +$. In the first excited state, a (1p) state is occupied by one of three quarks instead of a (1s) state. This excitation is represented as (1s)²(1p), giving $L = 1$ and $P = -$. Since one quark occupies a different state from the others, we can form symmetric, mixed symmetric, and mixed antisymmetric wavefunctions under O(3). The wavefunction of the (1s)²(1p) state is represented by $\mathbf{r}_1\phi_0, \mathbf{r}_2\phi_0, \mathbf{r}_3\phi_0$ when we assume the ground-state wavefunction is $\phi_0(\mathbf{r}_1, \mathbf{r}_2, \mathbf{r}_3)$ with the quark coordinates $\mathbf{r}_1, \mathbf{r}_2, \mathbf{r}_3$. The symmetric, mixed symmetric, and mixed antisymmetric wavefunctions are

$$\phi_S = \frac{1}{\sqrt{3}}(\mathbf{r}_1 + \mathbf{r}_2 + \mathbf{r}_3)\phi_0, \quad (1.19)$$

$$\phi_{MS} = \frac{1}{\sqrt{6}}(\mathbf{r}_1 + \mathbf{r}_2 - 2\mathbf{r}_3)\phi_0, \quad (1.20)$$

$$\phi_{MA} = \frac{1}{\sqrt{2}}(\mathbf{r}_1 - \mathbf{r}_2)\phi_0. \quad (1.21)$$

If we take the center-of-mass system of the quarks

$$\mathbf{r}_1 + \mathbf{r}_2 + \mathbf{r}_3 = 0, \quad (1.22)$$

the symmetric wavefunction ϕ_S vanishes. So, only mixed symmetric and mixed antisymmetric wavefunctions remain at the first excitation level. Since the overall wavefunction under $SU(6) \times O(3)$ must be symmetric, the $SU(6)$ states must be mixed symmetric or mixed antisymmetric. Hence baryons at the first excitation level belong to 70-plet in $SU(6)$. As expressed in Eq. 1.11, the **70** in $SU(6)$ contains the singlet, octet, and decuplet with $S = 1/2$ and the octet with $S = 3/2$ in $SU(3)$. The spin-parity J^P of each excited state is listed in Table 1.4. Table 1.5 summarizes the first excited states that are experimentally observed. Some resonance states having strangeness have yet to be found.

Table 1.4: First excited states of baryon.

\mathbf{D}	$S \oplus L$	J^P
${}^2_{10}$	$(S = 1/2) \oplus (L = 1)$	$\frac{1}{2}^-, \frac{3}{2}^-$
2_8	$(S = 1/2) \oplus (L = 1)$	$\frac{1}{2}^-, \frac{3}{2}^-$
4_8	$(S = 3/2) \oplus (L = 1)$	$\frac{1}{2}^-, \frac{3}{2}^-, \frac{5}{2}^-$
2_1	$(S = 1/2) \oplus (L = 1)$	$\frac{1}{2}^-, \frac{3}{2}^-$

Table 1.5: Observed baryons in the first excitation band.

$\mathbf{D}; S$	$J^P = 1/2^-$	$J^P = 3/2^-$	$J^P = 5/2^-$
${}^2_8; 1/2$	$N(1535)1/2^-$	$N(1520)3/2^-$	
${}^4_8; 3/2$	$N(1650)1/2^-$	$N(1700)3/2^-$	$N(1675)5/2^-$
${}^2_{10}; 1/2$	$\Delta(1620)1/2^-$	$\Delta(1700)3/2^-$	
${}^2_8; 1/2$	$\Lambda(1670)1/2^-$	$\Lambda(1690)3/2^-$	
${}^4_8; 3/2$	$\Lambda(1800)1/2^-$	missing	$\Lambda(1830)5/2^-$
${}^2_8; 1/2$	$\Sigma(1620)1/2^-$	$\Sigma(1670)3/2^-$	
${}^4_8; 3/2$	$\Sigma(1750)1/2^-$	missing	$\Sigma(1775)5/2^-$
${}^2_{10}; 1/2$	missing	missing	

$N(1535)1/2^-$

$N(1535)1/2^-$ is considered as a first excited state with an excitation energy of $1\hbar\omega$ in the CQM. It was observed in 1960s in the $\pi^-p \rightarrow \eta n$ [3] and $\gamma p \rightarrow \eta p$ [4, 5] reactions near the threshold. The S-wave dominance was suggested by a uniform angular distribution without any asymmetry against 90 degrees. Since $N(1535)1/2^-$ is the lowest negative parity state with a spin of 1/2, it is a candidate for a chiral partner of the ground-state nucleon $N(940)1/2^+$, namely $N(1535)1/2^-$ and $N(940)1/2^+$ form a parity doublet[6]. $N(1535)1/2^-$ strongly couples to ηN in its decay [2]. Since the η meson wavefunction includes the $s\bar{s}$ content, it is possible that $N(1535)1/2^-$ also has the $s\bar{s}$ content [7].

Second excitation band

Let us move on the second excited state. The $(1s)^2(2s)$ excitation is degenerate with both $(1s)(1p)^2$ and $(1s)^2(1d)$. These wavefunctions have a spurious component with $\mathbf{R} = (\mathbf{r}_1 + \mathbf{r}_2 + \mathbf{r}_3)/3$. We can eliminate the \mathbf{R} component by using appropriate linear combinations. These wavefunctions are represented in

the following equations:

$$\begin{aligned}
 \psi_{(1s)^2(2s)} &= \frac{\sqrt{2}}{3} \left\{ \frac{1}{b^2}(r_1^2 + r_2^2 + r_3^2) - \frac{9}{2} \right\} \psi_0, \\
 \psi_{(1s)(1p)^2} &= \frac{2}{3b^2}(\mathbf{r}_1 \cdot \mathbf{r}_2 + \mathbf{r}_2 \cdot \mathbf{r}_3 + \mathbf{r}_3 \cdot \mathbf{r}_1)\psi_0, \\
 \psi_{(1s)^2(1d)} &= \frac{2}{3\sqrt{5}b^2}(r_1^2 + r_2^2 + r_3^2)\psi_0.
 \end{aligned} \tag{1.23}$$

Using the Jacobi coordinates defined as

$$\begin{aligned}
 \mathbf{R} &= \frac{1}{3}(\mathbf{r}_1 + \mathbf{r}_2 + \mathbf{r}_3), \\
 \boldsymbol{\rho} &= \frac{1}{\sqrt{2}}(\mathbf{r}_1 - \mathbf{r}_2), \\
 \boldsymbol{\lambda} &= \frac{1}{6}(\mathbf{r}_1 + \mathbf{r}_2 - 2\mathbf{r}_3),
 \end{aligned} \tag{1.24}$$

Eq. 1.23 can be rewritten as follows.

$$\begin{aligned}
 \psi_{(1s)^2(2s)} &= \frac{\sqrt{2}}{3} \left\{ \frac{1}{b^2}(3R^2 + \rho^2 + \lambda^2) - \frac{9}{2} \right\} \psi_0, \\
 \psi_{(1s)(1p)^2} &= \frac{2}{3b^2} \{3R^2 - (\rho^2 + \lambda^2)\} \psi_0, \\
 \psi_{(1s)^2(1d)} &= \frac{2}{3\sqrt{5}b^2}(3R^2 + \rho^2 + \lambda^2)\psi_0.
 \end{aligned} \tag{1.25}$$

Let us discuss an excited state with $L^P = 0^+$ at first among the second excited states. The $L^P = 0^+$ state can be mixed state of $(1s)^2(2s)$ and $(1s)(1p)^2$ states. When we remove \mathbf{R} using a linear combination of Eq. 1.25, we obtain the wavefunction ψ_{0^+} :

$$\psi_{0^+} = -\sqrt{\frac{2}{3}}\psi_{(1s)^2(2s)} + \sqrt{\frac{1}{3}}\psi_{(1s)(1p)^2} = \sqrt{\frac{1}{3}} \left\{ \frac{9}{2} - \frac{3}{2b^2}(\rho^2 + \lambda^2) \right\} \psi_0. \tag{1.26}$$

Since the ψ_{0^+} is spatially symmetric, it combines with the symmetric 56-plet of SU(6). ψ'_{0^+} , which is orthogonal to ψ_{0^+} , is represented in the following equation:

$$\psi'_{0^+} = \sqrt{\frac{1}{3}}\psi_{(1s)^2(2s)} + \sqrt{\frac{2}{3}}\psi_{(1s)(1p)^2} = \sqrt{\frac{2}{3}} \left(\frac{3}{2} + \frac{R^2}{b^2} \right) \psi_0. \tag{1.27}$$

It means that the internal motion in the ground state and the center of mass in the (2s) excitation. Secondly, we consider the excited state with $L^P = 2^+$, which is a mixed state of $(1s)^2(1d)$ and $(1s)(1p)^2$ states. Similar to the case of 0^+ state, the wavefunction ψ_{2^+} is obtained as follow:

$$\psi_{2^+} = -\sqrt{\frac{5}{6}}\psi_{(1s)^2(1d)} + \sqrt{\frac{1}{6}}\psi_{(1s)(1p)^2} = \sqrt{\frac{1}{6}}(\rho^2 + \lambda^2)\psi_0. \quad (1.28)$$

Since the ψ_{2^+} is also spatially symmetric, it combines with the symmetric 56-plet of SU(6). Table 1.6 and 1.7 lists the experimentally observed states, which are considered candidates as the second excited states. Only a half of the expected states in the CQM has been observed.

$N(1440)1/2^+$

$N(1440)1/2^+$, the so-called Roper resonance, is considered as a second excited state with an excitation energy of $2\hbar\omega$ in the CQM. It was discovered in the partial wave analysis of πN scattering data [8]. Its mass is too low as compared with the expected second excited state in the CQM. The CQM suggests that the radial excitation energy is higher than the orbital excitation energy, indicating the mass-order is reversed between $N(1440)1/2^+$ (radial) and $N(1535)1/2^-$ (orbital). The $N(1440)1/2^+$ can be different from an ordinary qqq baryon. Several possibilities were discussed for its internal structure: the gluon excitation [9] and the σN meson-baryon molecule-like state [10]. Another interpretation is that the observed mass is much lower than its pole position [11]. We do not have a solid identification of the internal structure of $N(1440)1/2^+$.

Table 1.6: Observed baryons with $L^P = 0^+$ in the second excitation band.

$D; S$	N, Δ	Λ	Σ	Ξ
56, 8; 1/2	$N(1440)1/2^+$	$\Lambda(1600)1/2^+$	$\Sigma(1660)1/2^+$	$\Xi(1690)1/2^+$
56, 10; 3/2	$\Delta(1600)3/2^+$		missing	missing
70, 8; 1/2	$N(1710)1/2^+$	$\Lambda(1810)1/2^+$	$\Sigma(1770)1/2^+$	missing
70, 10; 1/2	$\Delta(1750)1/2^+$		$\Sigma(1880)1/2^+$	missing

Table 1.7: Observed baryons with $L^P = 1^+, 2^+$ in the second excitation band.

$\mathbf{D}; S$	$J^P = 1/2^+$	$J^P = 3/2^+$	$J^P = 5/2^+$	$J^P = 7/2^+$
56, 8; 1/2		$N(1720)3/2^+$	$N(1680)5/2^+$	
56, 8; 1/2		$\Lambda(1890)3/2^+$	$\Lambda(1820)5/2^+$	
56, 8; 1/2		$\Sigma(1840)3/2^+$	$\Sigma(1915)5/2^+$	
56, 10; 3/2	$\Delta(1910)1/2^+$	$\Delta(1920)3/2^+$	$\Delta(1905)5/2^+$	$\Delta(1950)7/2^+$
56, 10; 3/2	missing	$\Sigma(2080)3/2^+$	$\Sigma(2070)5/2^+$	$\Sigma(2030)7/2^+$
70, 8; 3/2	$N(1880)1/2^+$	$N(1900)3/2^+$	$N(1870)5/2^+$	$N(1990)7/2^+$
70, 8; 3/2	missing	missing	$\Lambda(2110)5/2^+$	$\Lambda(2020)7/2^+$
70, 8; 3/2	missing	missing	missing	missing (Σ)
70, 8; 1/2		missing	missing	(N, Λ, Σ)
70, 10; 1/2		missing	missing	(Δ, Σ)
20, 8; 1/2	missing	missing		(N, Λ, Σ)

Higher energy states

The existence of most of the higher energy states has not yet been established. For example, Table 1.8 lists the experimentally observed N^* resonances [15]. The number of "*" indicates the certainty of each resonance. Only a few N^* states have been established above 1.8 GeV, where several N^* s have wide widths and overlap each other in a mass spectrum. Unpolarized differential cross sections are not sufficient to extract the contribution of resonance states from the experimental results. Spin observables are required to perform a partial wave analysis (PWA) to separate different N^* s correctly.

1.3 Meson photoproduction

A powerful tool for clarifying the nucleon excitation spectra is photoproduction of mesons on the nucleon. In hadronic processes such as π -induced reaction, specific excited states that strongly couple to the initial state are likely to be dominated, and it becomes difficult to measure other resonances experimentally. In photoproduction processes, more excited states that couple to meson-baryon combinations, e.g., πN , ηN , ωN , or multi-meson final states ($\pi\pi N$, $\pi\eta N$, $\eta\eta N$, and so on) are produced. Therefore, it is advantageous to utilize photon-induced reactions to produce nucleon resonances that have weak coupling to πN channel. In addition, the spin information of intermediate resonances can also be

obtained by utilizing a highly polarized photon beam. Photoproduction experiments are increasingly gaining popularity in baryon physics research.

In the study of baryon excitation, the cross section measurement is essential since the cross section is sensitive to an intermediate resonant state. In the case of the photo-excitation of a proton target, it is possible to induce nucleon resonances. As the resonances decay back to the ground state the study of the decay products allows access to the resonance properties. As a photon interacts with a nucleon, it couples to the nucleon electromagnetic current. This can cause the production of mesons via the decay of an intermediate resonant state of the nucleon. The most common meson photoproduction experiments are those involving the pseudoscalar mesons such as a η meson.

Figure 1.5 shows the diagrams of η photoproduction on the proton. These diagrams include s -channel (a time-like channel), t -channel, and u -channel (space-like channels). The s -channel represents the process in which γ excites the proton and creates a resonance state N^* , which decays into an η meson and a proton. The u - and t -channels represent processes in which γ exchanges an intermediate particle, which is a N^* for the u -channel and a meson for the t -channel.

Generally, the contribution of u -channel is much smaller than t -channel in this energy, which does not include any resonance in the process, however, at the backward decay angle in the center of mass system, u -channel and s -channel are more important than t -channel. Therefore, we can expect that the measurement of the cross section at the backward angle will be more sensitive to the high mass nucleon resonance.

In single pseudoscalar meson photoproduction, there are total of 16 possible observables that can be measured [56]. They are called spin observables. These observables include the unpolarized differential cross section, denoted as $d\sigma_0$, as well as three asymmetries that enter the general cross section to leading order. These three asymmetries are scaled by a single polarization of either the beam, target, or recoil, and are denoted as Σ , T , and P , respectively. In addition to these asymmetries, there are three sets of four asymmetries each, whose leading polarization dependence in the general cross section involves two polarizations. These two polarizations can either be beam-target (BT), beam-recoil (BR), or target-recoil (TR). Photon beam asymmetry Σ is discussed in more detail in

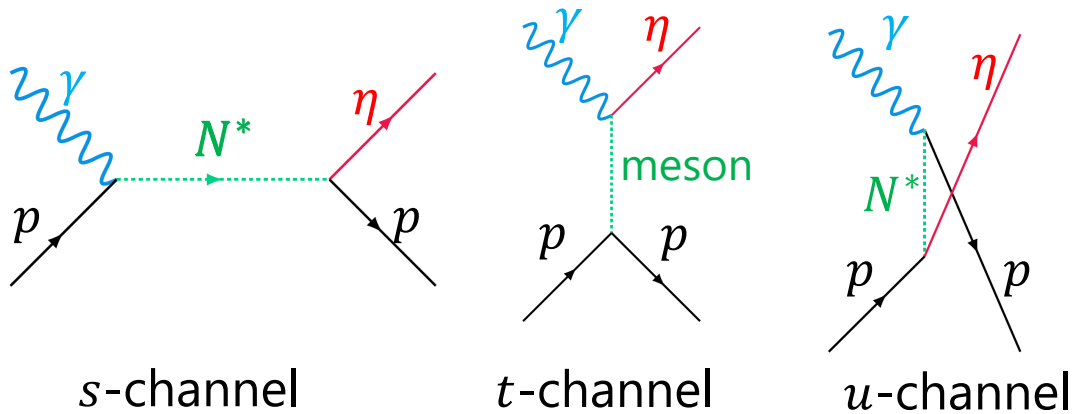


Figure 1.5: The diagrams of η meson photoproduction on the proton

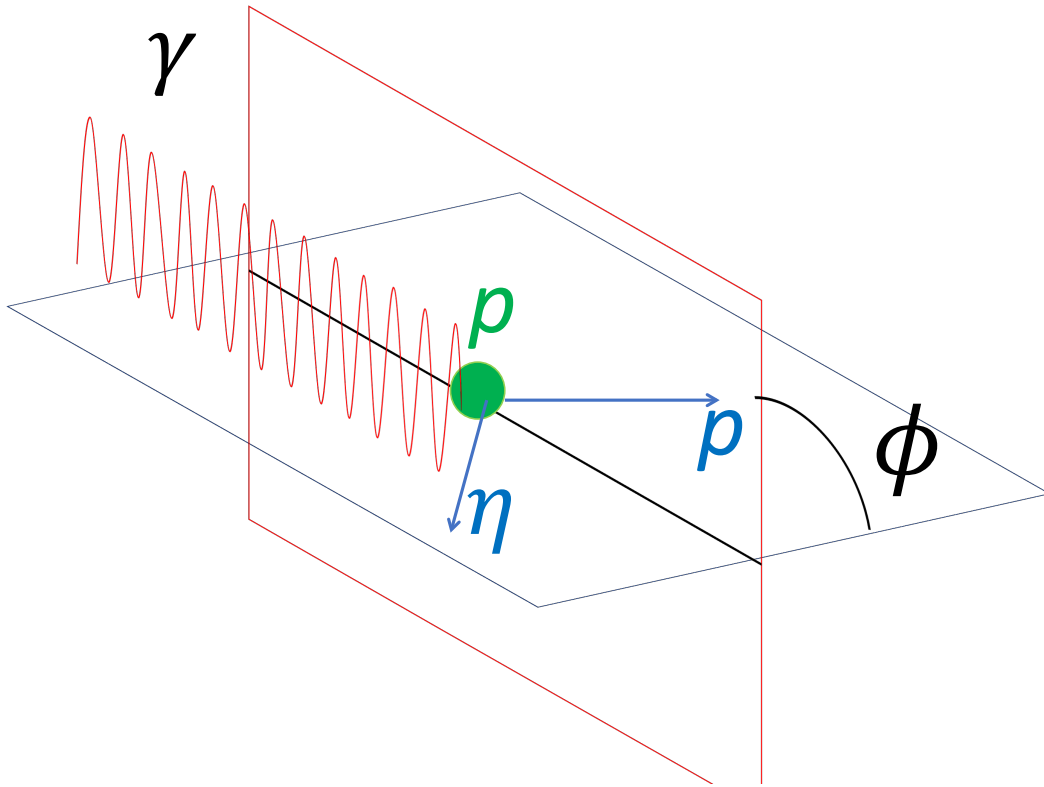
the next section.

Photon beam asymmetry Σ

The differential cross section of the meson photoproduction with a linearly polarized photon beam oscillates depending on the azimuthal angle between the beam polarization plane and the meson production plane. The amplitude of this oscillation is proportional to the photon beam asymmetry Σ . Photon beam asymmetry tends to show interference contributions between partial waves, which helps to separate each of the broad resonances when they are overlapping. The Σ is defined in the center-of-mass system as

$$\frac{d\sigma}{d\Omega} = \frac{d\sigma_0}{d\Omega} (1 - P_\gamma \Sigma \cos(2\Phi)) \quad (1.29)$$

where $\frac{d\sigma_0}{d\Omega}$ is the *unpolarized* differential cross section, P_γ is the degree of linear polarization of the photon beam, and Φ is the azimuthal angle between the linear polarization direction of the photon beam and the reaction plane of the meson photoproduction as showed in Fig. 1.6. Experimentally, two types of beams, one is horizontally polarised and another one is vertically polarised, are used to measure the photoproduction reaction, and the beam asymmetry is obtained from yield differences.


 Figure 1.6: Schematic view of η photoproduction.

1.3.1 Electro-magnetic multipole

In pseudoscalar meson photoproduction an incident photons excites a nucleon with total angular momentum J_γ and a resonance state with is generated as an intermediate state. After that the resonance state decays into a pseudoscalar meson and a nucleon. This reaction diagram is shown in Fig. 1.7. The total angular momentum J_γ is expressed as $|L_\gamma - S_\gamma| \leq J_\gamma \leq |L_\gamma + S_\gamma|$ using the spin of photon S_γ and the orbital angular momentum between the photon and the nucleon L_γ . The parity of photon and nucleon is $-$ and $+$, respectively and therefore the parity of the initial state is $P = (-1)(+1)(-1)^{L_\gamma}$. If P is $(-1)^{J_\gamma}$, transition in the photon radiation is electric, and if P is $-(-1)^{J_\gamma}$, transition in the photon radiation is magnetic, denoted as EJ_γ and MJ_γ , respectively.

We consider the spin-parity J^P of the intermediate state. Since the spin of the nucleon is $1/2$, the spin of the intermediate state is $J = J_\gamma \pm 1/2$. The parity of the intermediate state is the same as one of the initial state. The amplitudes of this reaction are electro-magnetic (EM) multipoles $E_{l\pm}$ and $M_{l\pm}$. In subscripts, l is the orbital angular momentum when the intermediate state

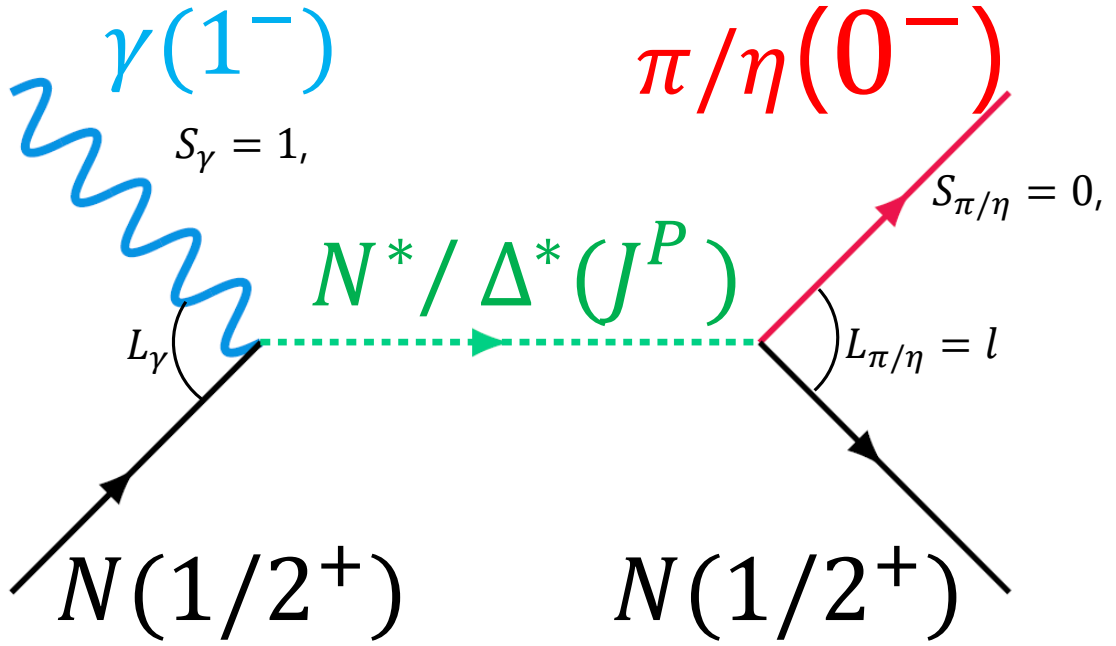


Figure 1.7: The diagram of π or η photoproduction.

is assumed as a πN system, and the sign is $+$ with $J = l + 1/2$ and $-$ with $J = l - 1/2$.

1.3.2 CGLN amplitudes

First, to discuss the commonly used Chew-Goldberger-Low-Nambu (CGLN) amplitude, some kinematic variables should be specified. Four-momenta of the incident photon, the proton in the target, the outgoing meson, and the recoil proton are denoted by $k = (k, \mathbf{k})$, $p_1 = (E_1, \mathbf{p}_1)$, $q = (\omega, \mathbf{q})$, and $p_2 = (E_2, \mathbf{p}_2)$. Helicities of these four particles are λ_k , λ_1 , λ_q , λ_2 , respectively. Since pseudoscalar mesons have spin 0, λ_q is 0. The incident photon has polarization vector. The polarization vector is defined as $\boldsymbol{\varepsilon}$ for incident photons. Figure 1.8 shows the pseudoscalar meson photoproduction in the center-of-mass(c.m.) system. In the c.m. system, the total energy is W , the polar angle and the azimuthal angle of the meson are θ and ϕ .

The differential cross section for pseudoscalar meson photoproduction in the

Table 1.9: The transition in the photon radiation, the spin-parity of the incident photon J_γ^P , the spin-parity of the intermediate state J^P , the orbital angular momentum of the πN system l , and EM multipoles in pseudoscalar meson photoproduction.

Transition in the photon radiation	J_γ^P	J^P	l	Multipole amplitude
E1	1^-	$1/2^-$	0	E_{0+}
		$3/2^-$	2	E_{2-}
M1	1^+	$1/2^+$	1	M_{1-}
		$3/2^+$	1	M_{1+}
E2	2^+	$3/2^+$	1	E_{1+}
		$5/2^+$	3	E_{3-}
M2	2^-	$3/2^-$	2	M_{2-}
		$5/2^-$	2	M_{2+}
E3	3^-	$5/2^-$	2	E_{2+}
		$7/2^-$	4	E_{4-}
M3	3^+	$5/2^+$	3	M_{3-}
		$7/2^+$	3	M_{3+}
E4	4^+	$7/2^+$	3	E_{3+}
		$9/2^+$	5	E_{5-}
M4	4^-	$7/2^-$	4	M_{4-}
		$9/2^-$	4	M_{4+}
E5	5^-	$9/2^-$	4	E_{4+}
		$11/2^-$	6	E_{6-}
M5	5^+	$9/2^+$	5	M_{5-}
		$11/2^+$	5	M_{5+}

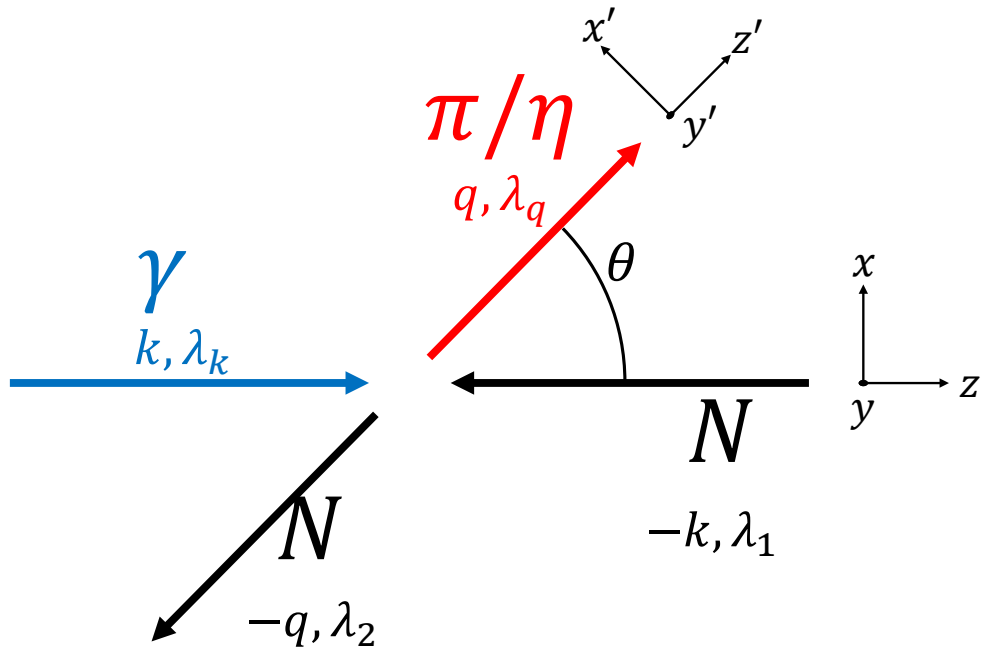


Figure 1.8: Kinematic variables in pseudoscalar meson photoproduction in c.m. system.

c.m. system can be written as

$$d\sigma/d\Omega = \frac{1}{4} \sum_{m_{s_i}=\pm 1/2} \sum_{m_{s_f}=\pm 1/2} \sum_{\gamma\text{-spins}} \frac{1}{4\pi^2} \frac{q}{k} \frac{m_p^2}{W^2} |\mathbf{J}|^2, \quad (1.30)$$

$$\mathbf{J} = \frac{4\pi W}{m_p} \langle m_{s_f} | F_{\text{CGLN}} | m_{s_i} \rangle, \quad (1.31)$$

where $|m_s\rangle$ is the eigenstate of the Pauli operator σ_z and F_{CGLN} is the CGLN amplitude [12]:

$$F_{\text{CGLN}} = \sum_{i=1}^4 O_i F_i(\theta, E) \quad (1.32)$$

with

$$O_1 = \boldsymbol{\sigma} \cdot \boldsymbol{\varepsilon}, \quad (1.33)$$

$$O_2 = [\boldsymbol{\sigma} \cdot \hat{q}][\boldsymbol{\sigma} \cdot (\hat{k} \times \boldsymbol{\varepsilon})], \quad (1.34)$$

$$O_3 = [\boldsymbol{\sigma} \cdot \hat{k}][\hat{q} \cdot \boldsymbol{\varepsilon}], \quad (1.35)$$

$$O_4 = [\boldsymbol{\sigma} \cdot \hat{q}][\hat{q} \cdot \boldsymbol{\varepsilon}], \quad (1.36)$$

where $\boldsymbol{\sigma}$ are Pauli matrices, and \hat{k} and \hat{q} are unit vectors of the photon and the meson. The CGLN amplitude expanded by EM multipole amplitudes can be expressed as follows:

$$F_1 = \sum_{l=0} [(E_{l+} + lM_{l+})P'_{l+1}(\cos\theta) + \{E_{l-} + (l+1)M_{l-}\}P'_{l-1}(\cos\theta)], \quad (1.37)$$

$$F_2 = \sum_{l=1} [(l+1)M_{l+1}P'_l(\cos\theta) + lM_{l-1}P'_l(\cos\theta)], \quad (1.38)$$

$$F_3 = \sum_{l=1} [(E_{l+} - M_{l+})P''_{l+1}(\cos\theta) + (E_{l-} + M_{l-})P''_{l-1}(\cos\theta)E_{l-}], \quad (1.39)$$

$$F_4 = \sum_{l=2} [(-E_{l+} + M_{l+} - E_{l-} - M_{l-})P''_l(\cos\theta)], \quad (1.40)$$

where $P_l(\cos\theta)$ is Legendre polynomials. Since EM multipole amplitudes correspond to resonance states, we can derive the contribution of each resonance state from each CGLN amplitude. Only two EM multipole amplitudes are associated with a resonance with a specified spin-parity. Table 1.10 lists the contribution of each resonance. The differential cross section $d\sigma/d\Omega$ and the

photon beam asymmetry Σ are represented as follows:

$$d\sigma/d\Omega = \frac{q}{k} \text{Re}\{F_1^*F_1 + F_2^*F_2 + \frac{1}{2}(F_3^*F_3 + F_4^*F_4) \sin^2 \theta + (F_2^*F_3 + F_1^*F_4 + F_3^*F_4 \cos \theta) \sin^2 \theta - 2F_1^*F_2 \cos \theta\}, \quad (1.41)$$

$$\Sigma = -\frac{q}{k} \text{Re}\{\frac{1}{2}(F_3^*F_3 + F_4^*F_4) + F_2^*F_3 + F_1^*F_4 + F_3^*F_4 \cos \theta\} \sin^2 \theta. \quad (1.42)$$

We can obtain the angular dependent differential cross section and photon beam asymmetry in each multipole amplitude. These are shown in Table 1.11 and 1.12 and Fig. 1.9.

Table 1.10: The contribution of each resonance state for CGLN amplitudes. Here $\cos \theta$ is replaced with x .

	$1/2^-$	$1/2^+$	$3/2^-$	$3/2^+$
F_1	E_{0+}		$3(M_{1+} + E_{1+})x$	$3(M_{2-} + E_{2-})$
F_2		M_{1-}	$2M_{1+}$	$6M_{2-}x$
F_3			$3(E_{1+} - M_{2+})$	
F_4				$-3(M_{2-} + E_{2-})$
	$5/2^-$		$5/2^+$	
F_1	$\frac{3}{2}(3M_{2+} + E_{2+})(5x^2 - 1)$		$3(4M_{3-} + E_{3-})x$	
F_2	$9M_{2+}x$		$\frac{9}{2}M_{3-}(5x^2 - 1)$	
F_3	$15(E_{2+} - M_{2+})x$		$3(E_{3-} + M_{3-})$	
F_4	$3(M_{2+} - E_{2+})$		$-15(M_{3-} + E_{3-})x$	
	$7/2^-$		$7/2^+$	
F_1	$\frac{5}{2}(3M_{3+} + E_{3+})(7x^3 - 3x)$		$\frac{3}{2}(5M_{4-} + E_{4-})(5x^2 - 1)$	
F_2	$6M_{3+}(5x^2 - 1)$		$10M_{4-}(7x^3 - 3)$	
F_3	$\frac{15}{2}(E_{3+} - M_{3+})(7x^2 - 2)$		$15(E_{4-} + M_{4-})x$	
F_4	$15(M_{3+} - E_{3+})x$		$-\frac{15}{2}(M_{4-} + E_{4-})(7x^2 - 3)$	
	$9/2^-$			
F_1	$\frac{5}{8}(4M_{4+} + E_{4+})(63x^4 - 70x^2 + 3)$			
F_2	$\frac{25}{2}M_{4+}(7x^3 - 3)$			
F_3	$\frac{105}{2}(E_{4+} - M_{4+})(3x^3 - x)$			
F_4	$\frac{15}{2}(M_{4+} - E_{4+})(7x^2 - 3)$			

We could express the physical observables in terms of CGLN amplitudes F_1, F_2, F_3, F_4 .

Table 1.11: Angular dependent differential cross section for a single multipole amplitude.

Photon multipole	Multipole amplitude	$d\sigma/d\Omega$
E1	E_{0+}	$ E_{0+} ^2$
	E_{2-}	$\frac{1}{2} E_{2-} ^2(5 - 3x^2)$
M1	M_{1-}	$ M_{1-} ^2$
	M_{1+}	$\frac{1}{2} M_{1+} ^2(5 - 3x^2)$
E2	E_{1+}	$\frac{9}{2} E_{1+} ^2(1 + x^2)$
	E_{3-}	$\frac{9}{2} E_{3-} ^2(1 + 6x^2 - 5x^4)$
M2	M_{2-}	$\frac{9}{2} M_{2-} ^2(1 + x^2)$
	M_{2+}	$\frac{9}{2} M_{2+} ^2(1 + 6x^2 - 5x^4)$
E3	E_{2+}	$\frac{9}{4} E_{2+} ^2(5 + 6x^2 + 5x^4)$
	E_{4-}	$\frac{9}{8} E_{4-} ^2(17 - 65x^2 + 255x^4 - 175x^6)$
M3	M_{3-}	$\frac{9}{4} M_{3-} ^2(5 + 6x^2 + 5x^4)$
	M_{3+}	$\frac{9}{8} M_{3+} ^2(17 - 65x^2 + 255x^4 - 175x^6)$

Table 1.12: Photon beam asymmetry as a function of the emission angle for a single multipole amplitude.

Photon multipole	Multipole amplitude	Σ
E1	E_{0+}	0
	E_{2-}	$-\frac{3}{2} E_{2-} ^2(1 - x^2)$
M1	M_{1-}	0
	M_{1+}	$\frac{3}{2} M_{1+} ^2(1 - x^2)$
E2	E_{1+}	$-\frac{9}{2} E_{1+} ^2(1 - x^2)$
	E_{3-}	$-\frac{9}{2} E_{3-} ^2(1 - x^2)(1 + 5x^2)$
M2	M_{2-}	$\frac{9}{2} M_{2-} ^2(1 - x^2)$
	M_{2+}	$\frac{9}{2} M_{2+} ^2(1 - x^2)(1 + 5x^2)$
E3	E_{2+}	$-9 E_{2+} ^2(1 - x^2)(1 + 5x^2)$
	E_{4-}	$-\frac{45}{8} E_{4-} ^2(1 - x^2)(3 - 6x^2 + 35x^4)$
M3	M_{3-}	$9 M_{3-} ^2(1 - x^2)(1 + 5x^2)$
	M_{3+}	$\frac{45}{8} M_{3+} ^2(1 - x^2)(3 - 6x^2 + 35x^4)$

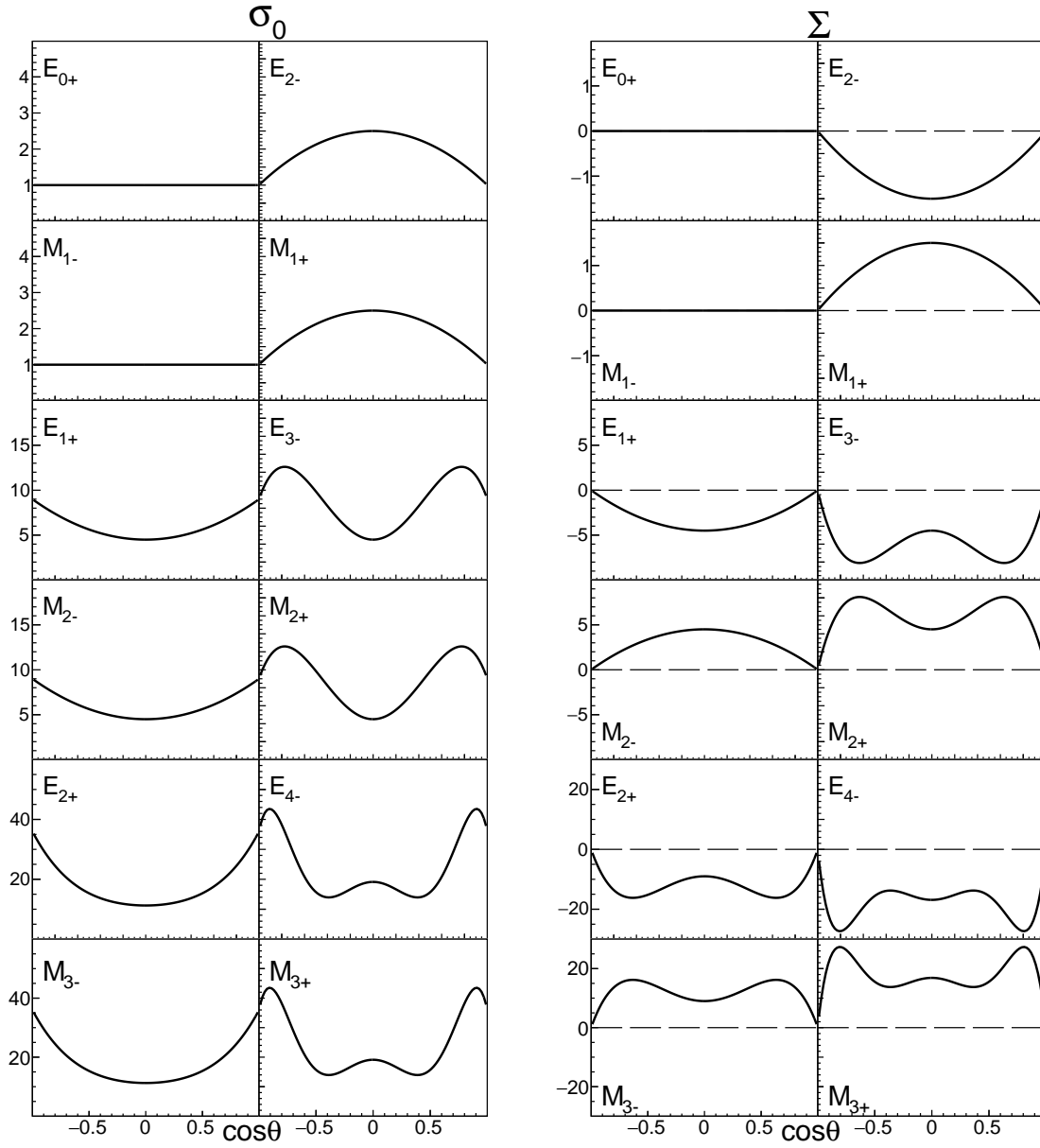


Figure 1.9: The angular distribution for a single EM multipole amplitude. The left shows the differential cross section and the right shows the photon beam asymmetry.

1.4 Previous experiments

1.4.1 η meson photoproduction

Here the photoproduction of an η meson is a prime example of such research subjects. The basic properties of η mesons are described. The mass of η mesons is $547.85 \text{ MeV}/c^2$. The main decay modes and these branching fractions of η mesons are listed in Table 1.13. Since an η meson is the lightest particle containing $s\bar{s}$ component, it is expected to easily couple with the nucleon resonances containing large $s\bar{s}$ component. Moreover, since the isospin of the η meson is 0, the isospin of the ηN state is $1/2$. This means that the intermediate state of the photoproduction reaction is limited to N^* and there is no need to consider the Δ^* contribution.

Table 1.13: Main decay modes and these branching fractions of η meson[15].

mode	branching fraction
$\gamma\gamma$	$(39.41 \pm 0.20)\%$
$3\pi^0$	$(32.68 \pm 0.23)\%$
$\pi^+\pi^-\pi^0$	$(22.92 \pm 0.28)\%$
$\pi^+\pi^-\gamma$	$(4.22 \pm 0.08)\%$

1.4.2 Experimental status of η photoproduction

The resonance state $N(1535)1/2^-$ is dominant near the threshold in the η meson photoproduction process. We introduce several experiments to study $N(1535)1/2^-$. In 2002, the GRAAL Collaboration measured the differential cross sections of $\gamma p \rightarrow \eta p$ reactions from threshold to 1.1 GeV photon [16]. Resonance parameters were obtained by fitting total cross sections near threshold with Breit-Wigner functions. However, the value could not be determined because the resonance widths varied from $152 \pm 4 \text{ MeV}$ to $174 \pm 8 \text{ MeV}$ by changing the fitting range. We introduce several experiments to study $N(1535)1/2^-$. In 2002, the GRAAL Collaboration measured the differential cross sections for $\gamma p \rightarrow \eta p$ reaction from threshold to 1.1 GeV photon [16]. Resonance parameters were derived by fitting total cross sections near threshold with the Breit-Wigner function. However, the value could not be determined because the resonance

width varied from 152 ± 4 MeV to 174 ± 8 MeV by changing the fitting range. In 2005, the CBELSA Collaboration measured the total cross section for the reaction $p(\gamma, \eta p)$ at $E_\gamma = 0.75 - 3$ GeV [17]. Figure 1.10 shows the total cross section for $\gamma p \rightarrow \eta p$ reaction in several experiments.

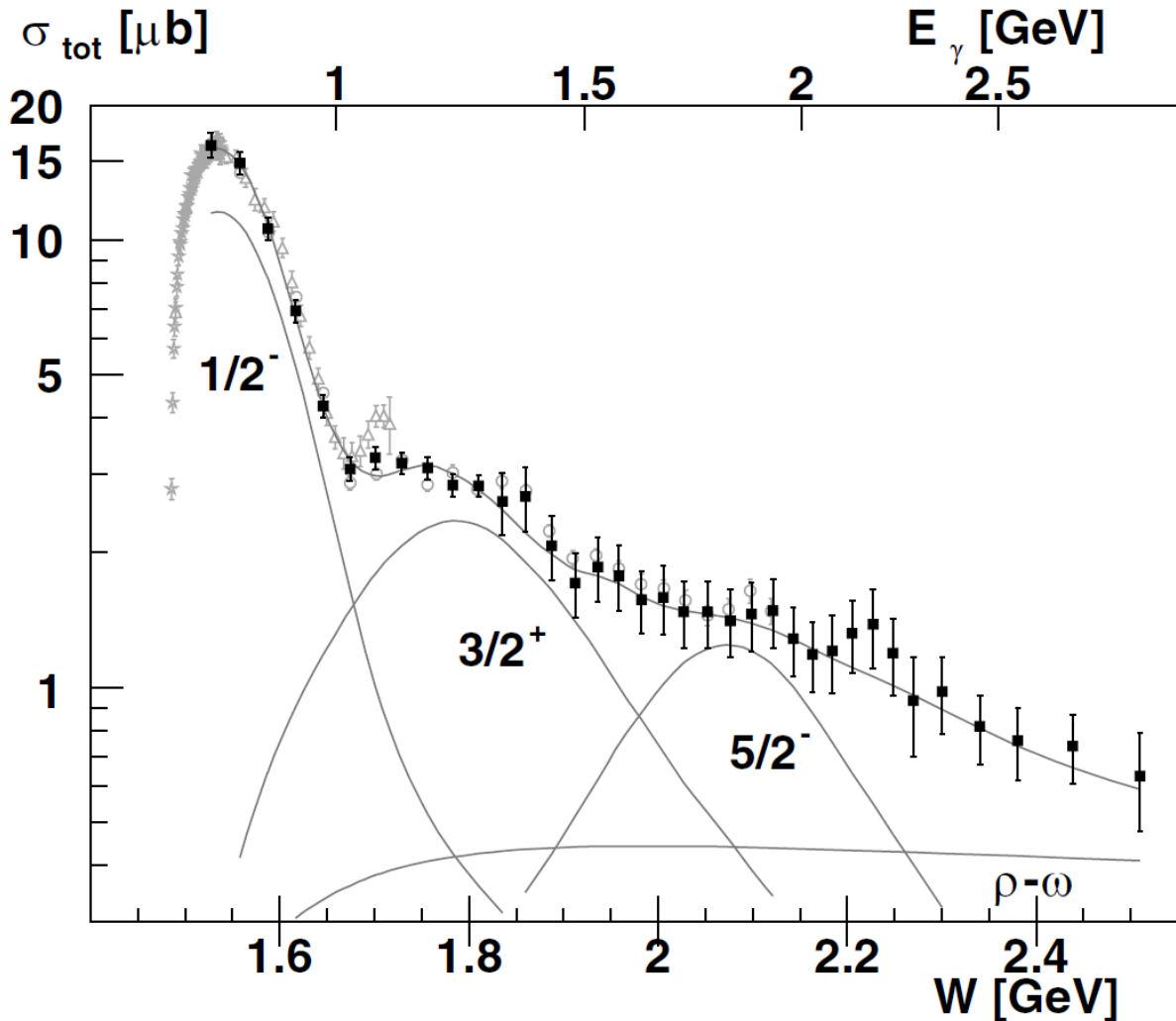


Figure 1.10: Total cross sections of η photoproduction on the proton. The black squares, light gray stars, light gray triangles, and light gray circles come from the TAPS [18], CBELSA [17], GRAAL [16], and CLAS [19] Collaborations.

Several experimental results of $\gamma p \rightarrow \eta p$ reaction around W of 2 GeV have been published. Table 1.14 lists these results.

In 2007, GRAAL Collaboration measured the differential cross section and photo beam asymmetries from threshold to 1.9 GeV [42]. In 2009, CLAS Collaboration and CBELSA/TAPS Collaboration separately reported differential cross sections of η photoproduction on proton in a wide range of angular and energy region [35, 36]. They confirmed the existence of several resonance states,

Table 1.14: Experimental results of $\gamma p \rightarrow \eta p$ reaction.

Observable	Exp.	W (GeV)	$\cos \theta_{\text{c.m.}}^\eta$	Ref.
$d\sigma/d\Omega$	GRAAL(2007)	1.48–1.92	−1.0 – 0.9	[42]
$d\sigma/d\Omega$	CLAS(2009)	1.68–2.84	−0.9 – 0.8	[35]
$d\sigma/d\Omega$	CBELSA/TAPS(2009)	1.57–2.38	−1.0 – 1.0	[36]
$d\sigma/d\Omega$	LEPS(2009)	1.97–2.32	−1.0 – −0.6	[20]
Σ	GRAAL(2007)	1.48–1.92	−1.0 – 0.9	[42]
Σ	CLAS(2017)	1.70–2.10	−0.8 – 0.8	[44]
Σ	CBELSA/TAPS(2020)	1.75–2.05	−1.0 – 1.0	[45]

which are not previously confirmed in πN scattering experiments. In the same year, LEPS Collaboration reported differential cross sections in the backward region and obtained results that suggested the existence of new resonance states [20]. In 2017, the CLAS Collaboration reported photon beam asymmetry of η photoproduction on proton up to 2.1 GeV in total energy for the first time [44]. They observed drastic change in the angular distribution of beam asymmetry. In 2020, CBELSA/TAPS Collaboration also reported photon beam asymmetry and observed singularities of scattering amplitudes such as cusp effects [45]. Each experiment is described in detail below.

GRAAL

The GRAAL facility was set at the European Synchrotron Radiation Facility (ESRF) in Grenoble, France [43]. It produced a polarized photon beam via Compton scattering of laser photons on the 6 GeV electrons. The 4π LA γ RANGE detector detected both neutral and charged particles [43]. The GRAAL Collaboration reported the differential cross sections and photon beam asymmetries for the η meson photoproduction from threshold to 1.9 GeV in 2007 [42]. The η mesons were reconstructed in two neutral decay modes: $\eta \rightarrow 2\gamma$ and $\eta \rightarrow 3\pi^0 \rightarrow 6\gamma$. Their results were compared with three PWA models of MAID, BCC, and Bonn-Gatchina. These models reproduced the behavior of experimental results rather well. Nevertheless contributions of individual resonances were quite different.

CBELSA/TAPS

This experiment was carried out at the electron accelerator facility (ELSA) at the University of Bonn using a combination of the Crystal-Barrel (CB) and TAPS detector. These detectors are electromagnetic calorimeters covering all solid angles and can detect all the photon produced by the decay of the meson. A linearly polarized beam photon was produced via coherent bremsstrahlung. Polarization degree was typically 20% above $W = 2$ GeV [60]. The CBELSA/TAPS Collaboration reported total and differential cross sections of η photoproduction on proton for the photon energies between 0.85 and 2.55 GeV in 2009 [36]. The η mesons are detected in the two neutral decay modes, $\eta \rightarrow \gamma\gamma$ and $\eta \rightarrow 3\pi^0 \rightarrow 6\gamma$, and cover the almost full angular range in $\cos\theta_{\text{c.m.}}^\eta$. The total cross section was nearly saturated with three resonances, the well-known $N(1535)1/2^-$, the $N(1720)3/2^+$, and the new resonance $N(2060)5/2^-$ at the time. Now $N(2060)$ is listed as a *** state by Particle Data Group [15]. This collaboration also measured photon beam asymmetries for tagged photon energies from 1.130 to 1.790 GeV in 2020 [45]. They performed partial wave analyses and observed singularities of scattering amplitudes such as cusp effects. They concluded that the existence of the $N(1895)1/2^-$ resonance was confirmed, and precise resonance parameters were obtained. Now $N(1895)$ is evaluated as a **** state by Particle Data Group [15].

CLAS

The CLAS is a large acceptance spectrometer in the Continuous Electron Beam Accelerator Facility (CEBAF) at the Department of Energy's Thomas Jefferson National Accelerator Facility in Newport News, Virginia. This spectrometer can detect charged particles in $8^\circ < \theta < 140^\circ$. They produce a linearly polarized photon beam by coherent bremsstrahlung using a 4.55 GeV electron. Polarization is typically 30% above $W = 2$ GeV [61]. The CLAS Collaboration measured differential cross sections for the reactions $\gamma p \rightarrow p\eta$ for center-of-mass energies from near the threshold energy up to 2.84 GeV in 2009 [35]. Photon beam asymmetries for center-of-mass energies from incident photon energies from 1.070 to 1.876 GeV in 2017[44]. The η mesons were detected in a charged decay mode: $\eta \rightarrow \pi^+\pi^-\pi^0$. They required p , π^+ , and π^- to be detected

and missing mass of $\gamma p \rightarrow \pi^+\pi^-pX$ reaction to be π^0 . They performed partial wave analyses with the Bonn-Gatchina model and confirmed the evidence for four nucleon resonances: $N(1895)1/2^-$, $N(1900)3/2^+$, $N(2100)1/2^+$, and $N(2120)3/2^-$, which lacked the "****" status in Particle Data Group at that time.

LEPS experiment in 2009

In 2009, the LEPS Collaboration measured differential cross sections for η meson photoproduction on proton targets in the backward angular region in the energy range $E_\gamma = 1.6 - 2.4$ GeV of incident photons. Identification of the η mesons was performed from the missing mass distribution of the $\gamma p \rightarrow pX$ reaction. The results of the LEPS experiment are shown in Fig. 1.11. Bump structures can be seen above the total energy $W = 2$ GeV. The center position of the bump structure shifts to higher energies as the backward angle increases. The position is $W \sim 2.06$ GeV for $-0.7 < \cos \theta_{\text{c.m.}}^\eta < -0.6$ and $W \sim 2.17$ GeV for $-1.0 < \cos \theta_{\text{c.m.}}^\eta < -0.9$. This behavior suggests that this bump structure consists of multiple resonance states with different angular distributions.

1.5 Present experiment

We measured not only differential cross sections but also photon beam asymmetries for the reaction $\gamma p \rightarrow \eta p$ in the LEPS2/BGOegg experiment. The coverage of polar angles is $-1.0 < \cos \theta_{\text{c.m.}}^\eta < 0.6$. We can generate linearly polarized beams at $E_\gamma = 1.3-2.4$ GeV by means of backward Compton scattering, as described in Sec. 2.1.2. The degree of the beam polarization is higher than 70% above $E_\gamma = 1.7$ GeV. The η mesons were detected in a neutral decay mode: $\eta \rightarrow \gamma\gamma$. All the final-state particles were detected, a recoil proton and two γ 's from the η meson decay. To reduce the background contribution, we required the following conditions for selecting the events: the four-momentum conservation between the initial and final states; and the two-photon invariant mass being the nominal η mass.

We have two significant advantages over LEPS experiment. The first one is a wide angular coverage of detecting η mesons. While the LEPS only covers the

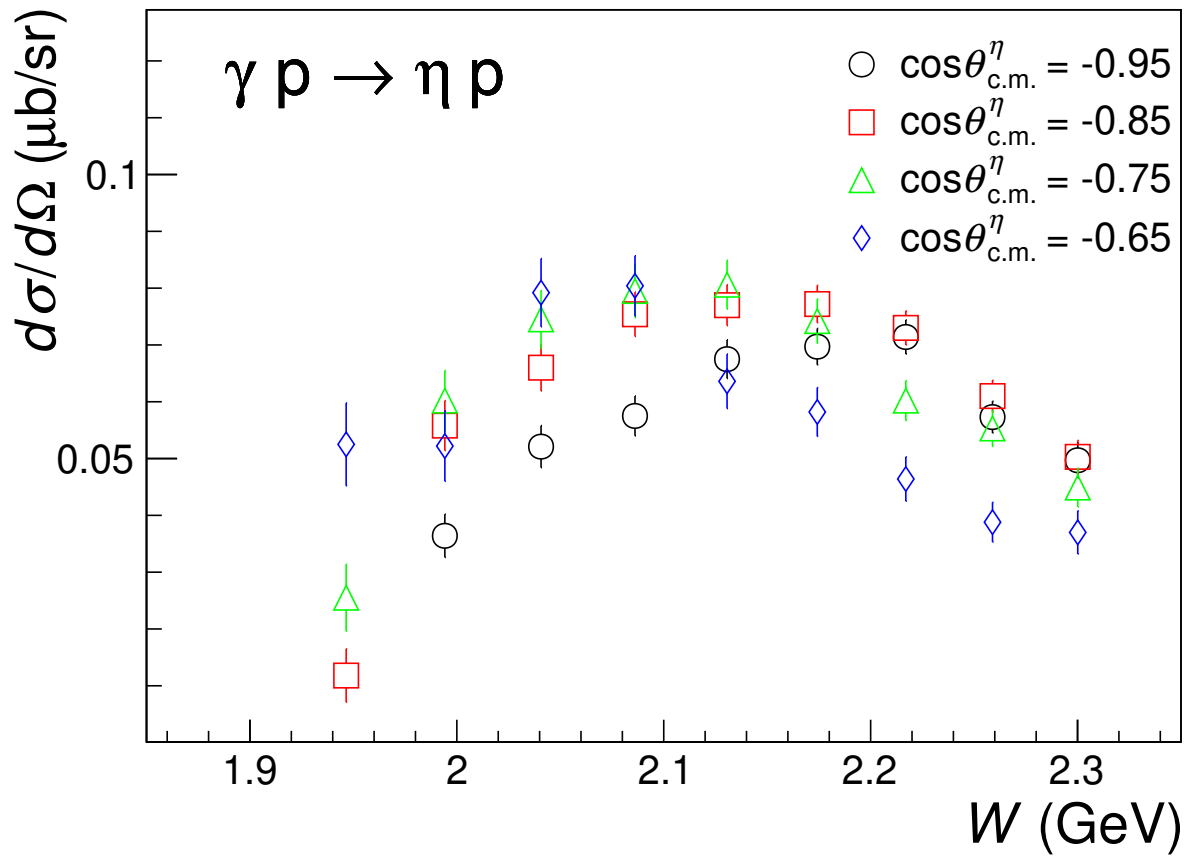


Figure 1.11: The differential cross section for η photoproduction on the proton at LEPS [20].

backward angles, $-1.0 < \cos \theta_{\text{c.m.}}^\eta < -0.6$, the BGOegg also covers the sideways angles, $-1.0 < \cos \theta_{\text{c.m.}}^\eta < 0.6$. Therefore, the behavior of the bump structure observed in the LEPS experiment can be investigated over a wider region. The other is a good signal-to-noise (S/N) ratio. In the LEPS experiment, the S/N ratio was poor because η meson was not directly detected, and therefore the statistics were not sufficient to determine beam asymmetry. In the BGOegg experiment, all particles in the final state are measured and kinematically restricted applying four-momentum conservation, which improves the S/N ratio and makes it possible to measure photon beam asymmetry with the same level of statistics.

Our statistical uncertainties are about half those of CBELSA. CLAS has no acceptance for the most backward region. Therefore, the BGOegg experiment is most suitable to study the enhancement of the differential cross sections in the backward region. In addition, the degree of our beam polarization is many times greater than that from the CBELSA experiment. CBELSA uses a coherent bremsstrahlung technique to generate a linearly polarized photon beam. The intensity and polarization of this photon beam are shown in Fig. 1.12 [21]. The beam polarization is lower than 10% above $E_\gamma = 1.7$ GeV, and hence it is difficult to measure the photon beam symmetry precisely in this incident photon energy region. Thanks to the high polarization in our photon beam, we can measure photon beam asymmetries in high precision. In particular, our measurement is first in the world above $E_\gamma = 1.9$ GeV. This is also an advantage over the CLAS experiment.

We study excited states of nucleons above 2 GeV by measuring the differential cross sections and photon beam asymmetries of η photoproduction on the proton using linearly polarized photons at $E_\gamma = 1.3 - 2.4$ GeV.

The LEPS Collaboration observed a bump structure above $W = 2$ GeV in the backward region of η emission. The peak position of this bump structure shifted with each angle, suggesting the contribution of multiple resonance states. However, this could not be concluded from the differential cross section measurement. In order to investigate the origin of this structure, we measure the photon beam asymmetries in addition to the differential cross sections over a wide angular range in the LEPS2/BGOegg experiment.

By comparing the obtained angular distributions of differential cross sec-

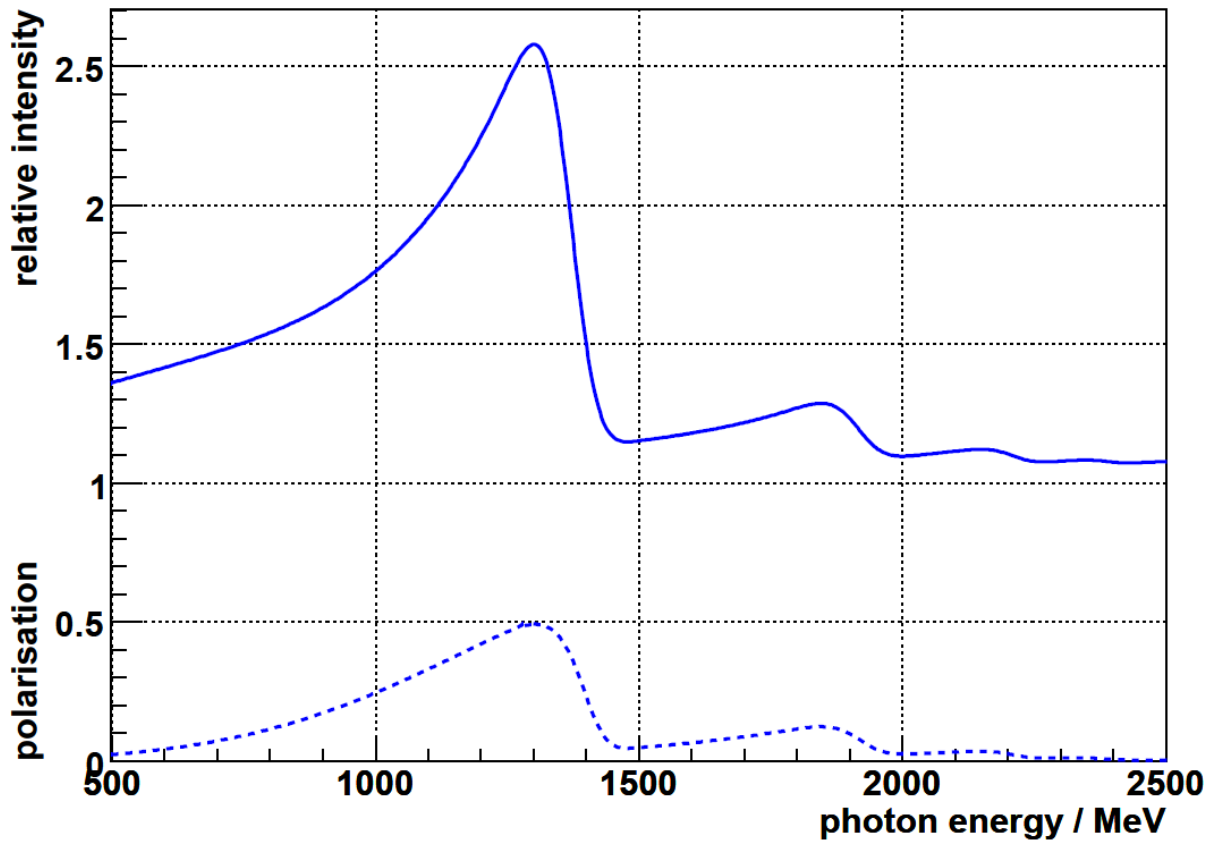


Figure 1.12: Intensity and polarization of the photon beam in CBELSA experiment[21]. The solid and dotted curves show the intensity and the degree of beam polarization obtained in the simulation, respectively, as a function of the photon energy.

tions and photon beam asymmetries with the calculated angular distribution of those as shown in Fig. 1.9, the spin-parity of the candidate resonance state is constrained. We compare our results with several PWA calculations such as EtaMAID [22] and Bonn-Gatchina [23]. Our new beam asymmetry measurement provides strong constraints on the PWA calculations in high energy region.

Chapter 2

Experiment

The experiment was carried out at the LEPS2 beamline at SPring-8. A photon beam was produced by means of Backward Compton Scattering (BCS) of ultraviolet (UV) laser from 8 GeV electrons in the SPring-8 storage ring. Photon beam energy was estimated from the recoil electrons with the tagging counter. The photon beam was transferred to the LEPS2 experimental building and hit a liquid hydrogen target. Produced particles were measured by the BGOegg detector system. The details of the experimental set up are described in this chapter.

2.1 SPring-8/LEPS2 facility

2.1.1 LEPS2 beamline

SPring-8 is a large synchrotron radiation facility located in Harima Science Park City, Hyogo Prefecture, Japan [24]. 100 mA electrons with 8 GeV energies are stored in the storage ring. The beamlines of SPring-8 are shown in Fig. 2.1. The LEPS2 beamline is located at BL31LEP, which is one of the 30 m long straight sections in the storage ring. The electron emittance of long sectors is 14 μrad . Figure 2.2 shows a schematic view of LEPS2 beamline. The photon beam is produced by backward Compton scattering with ultraviolet laser photons injected onto the 8 GeV electrons in the storage ring. The photon beam is transferred to the LEPS2 experimental building located 125 m downstream from the collision point and outside of the storage ring. As mentioned above, the small emittance of the electrons allows the beam size to remain sufficiently

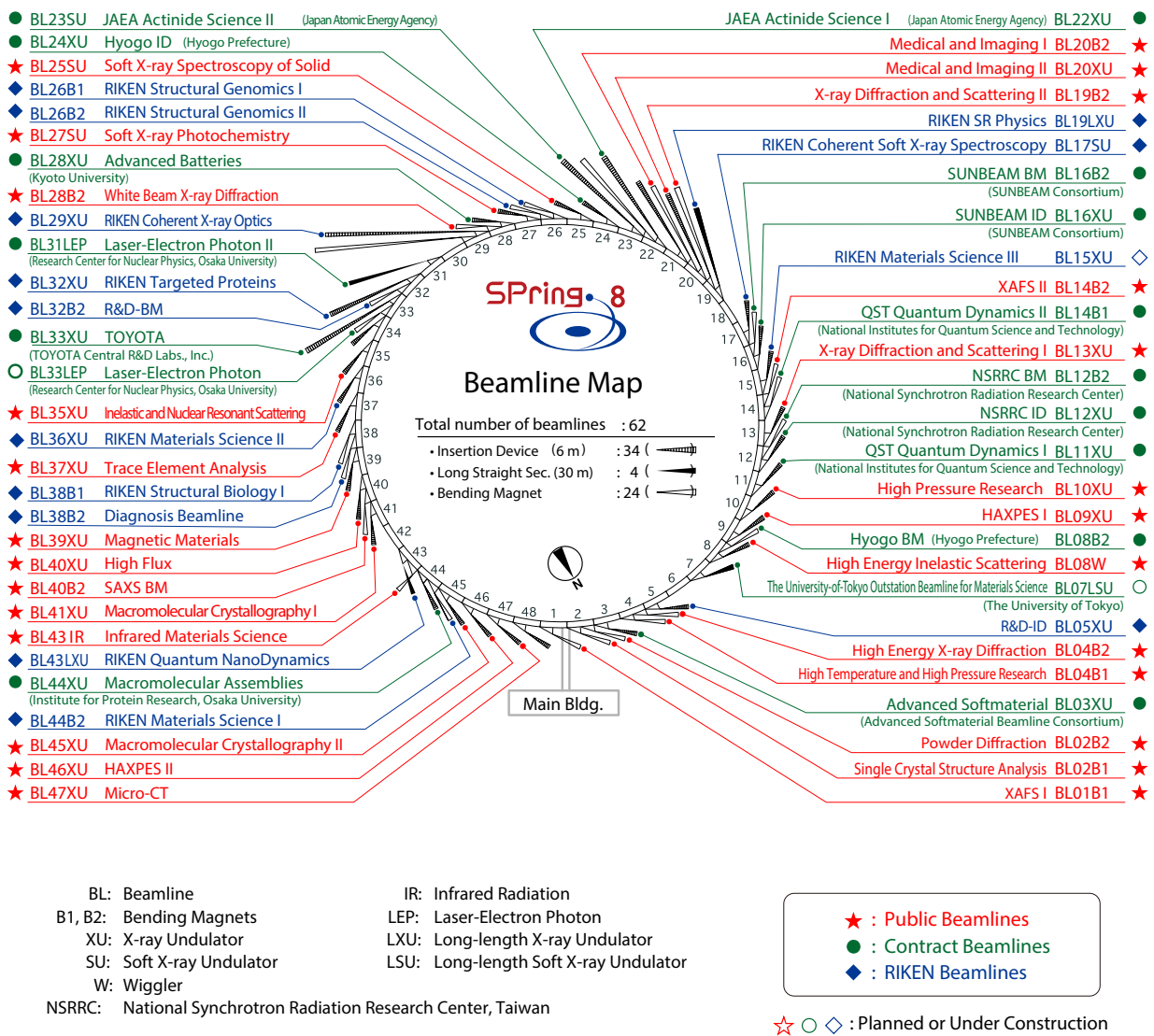


Figure 2.1: The beamline map of SPring-8 [24]. LEPS2 beamline is located at BL31LEP.

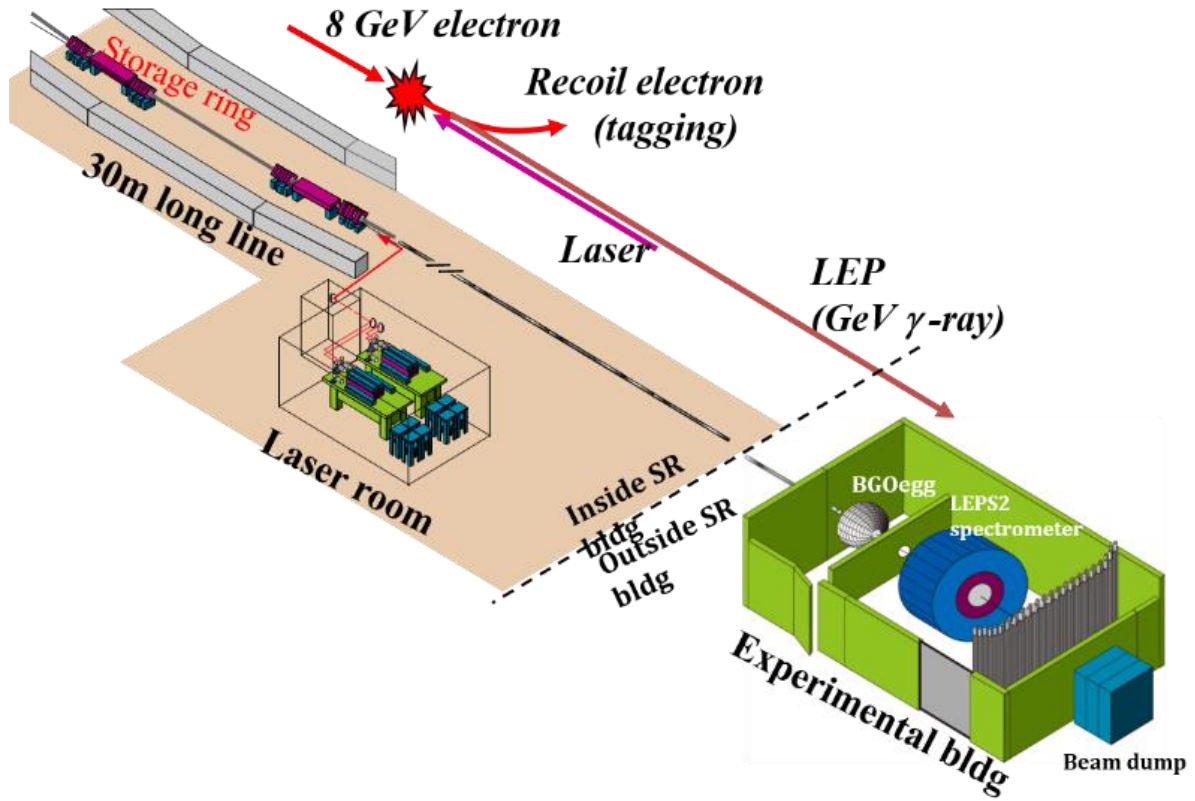


Figure 2.2: A schematic view of LEPS2 beamline.

small after transferring to the LEPS2 experimental building. The standard deviation in the x- and y-axis directions are 7.86 mm and 8.66 mm, respectively. The recoil electrons are detected by the tagging counter to measure the energies of produced photons.

2.1.2 Backward Compton scattering

Here, we describe the principle of generating a photon beam by backward Compton scattering. When a laser photon with energy k_1 strikes an electron with energy E_e as shown in Fig. 2.3, the energy of scattered photon E_γ is calculated as follows:

$$E_\gamma = k_1 \frac{1 - \beta \cos \theta_1}{1 - \beta \cos \theta_2 + (k_1/E_e)(1 - \cos(\theta_1 - \theta_2))}, \quad (2.1)$$

where θ_1 and θ_2 are defined as the angles between an electron and a laser photon and the angles between an electron and a scattered photon as shown in Fig. 2.3. β denotes the incoming electron velocity in units of the speed of light c . In the

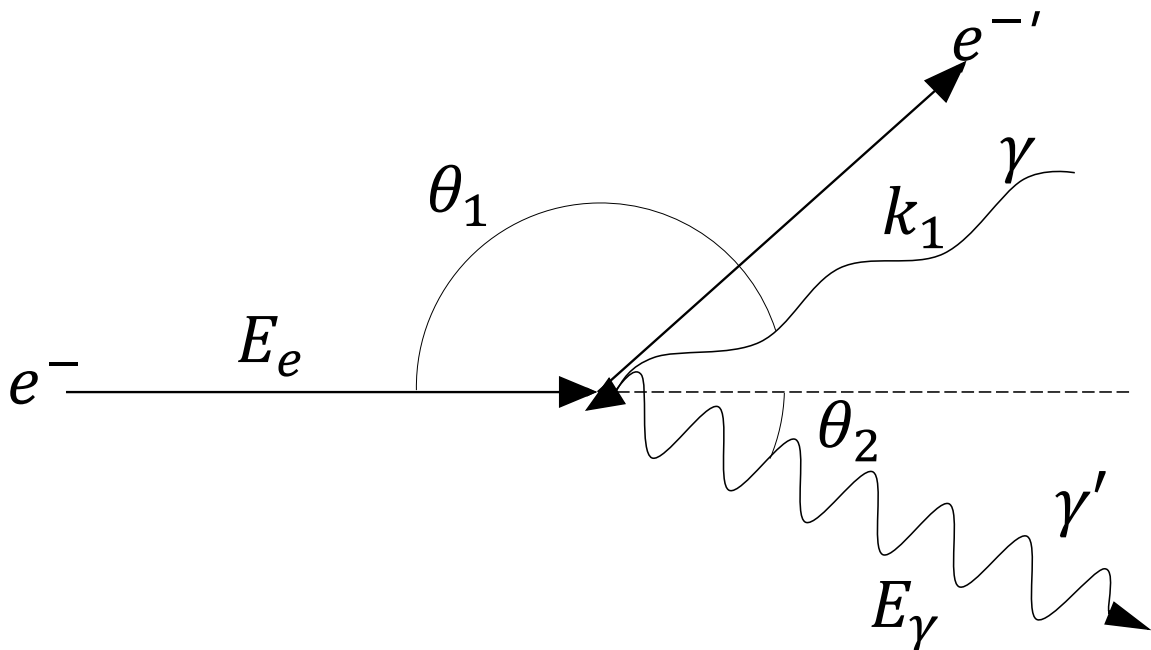


Figure 2.3: A schematic drawing of a backward Compton scattering.

LEPS2/BGOegg experiment, $\beta \simeq 1$, $\theta_1 \simeq 180^\circ$, and $\theta_2 \simeq 0^\circ$. Then, Eq. 2.1 can be written as

$$E_\gamma = \frac{4E_e^2 k_1}{m_e^2 + 4E_e k_1 + \theta_2^2 \gamma^2 m_e^2}, \quad (2.2)$$

where m_e is electron mass and γ is Lorentz factor. The BCS photons have the maximum energy when θ_2 is 0° . In this work, E_e is 7.975 ± 0.003 GeV and k_1 is 3.49 ± 0.00 eV with a wavelength of 355 nm, therefore the maximum BCS photon energy E_γ^{\max} are calculated to be 2.385 GeV. The differential cross section for Compton scattering in the laboratory frame is written as follows [25]:

$$\frac{d\sigma}{dE_\gamma} = \frac{2\pi r_e^2 a}{E_\gamma^{\max}} (\chi + 1 + \cos \alpha^2), \quad (2.3)$$

where

$$a = \frac{m_e^2}{m_e^2 + 4E_e k_1}, \quad (2.4)$$

$$\chi = \frac{(E_\gamma/E_\gamma^{\max})^2(1-a)^2}{1 - (E_\gamma/E_\gamma^{\max})(1-a)}, \quad (2.5)$$

$$\cos \alpha = \frac{E_\gamma^{\max} - E_\gamma(1+a)}{E_\gamma^{\max} - E_\gamma(1-a)}. \quad (2.6)$$

r_e is the classical electron radius and its value is 2.818 ± 0.000 fm. The degree of linear polarization of the scattered photon P_γ is proportional to that of the laser beam P_{laser} as follows [25]:

$$P_\gamma = P_{\text{laser}} \frac{(1 - \cos \alpha)^2}{2(\chi + 1 + \cos \alpha^2)}. \quad (2.7)$$

Figure 2.4 shows the E_γ dependence of the differential cross section for the BCS process (left) and the degree of linear polarization (right).

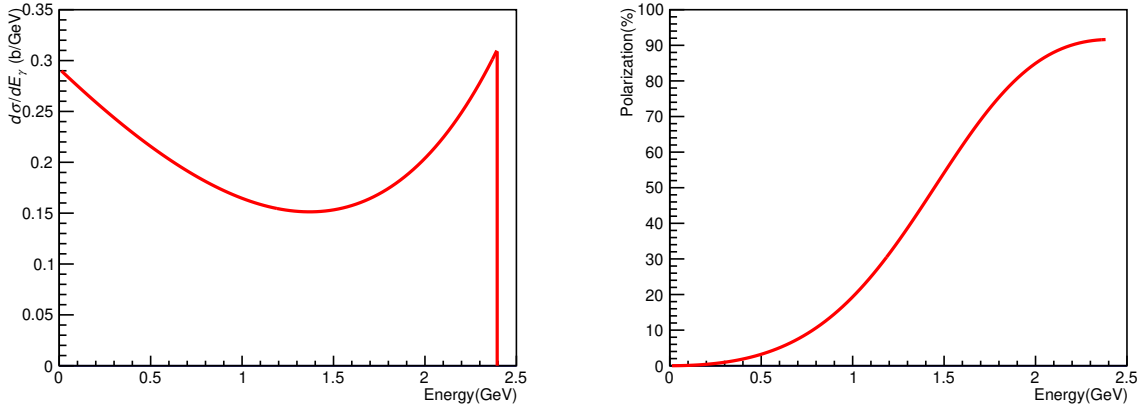


Figure 2.4: A left figure shows differential cross section for the BCS process. A right figure shows linear polarization of the BCS photons, assuming that the degree of the laser polarization P_{laser} is 97.5%.

2.2 LEPS2/BGOegg experimental set up

We measured the $\gamma p \rightarrow \eta p \rightarrow \gamma \gamma p$ reaction. The photon energy was evaluated by measuring a recoil electron of the BCS process with a tagging counter located near the storage ring. Figure 2.5 shows the experimental set up. Events

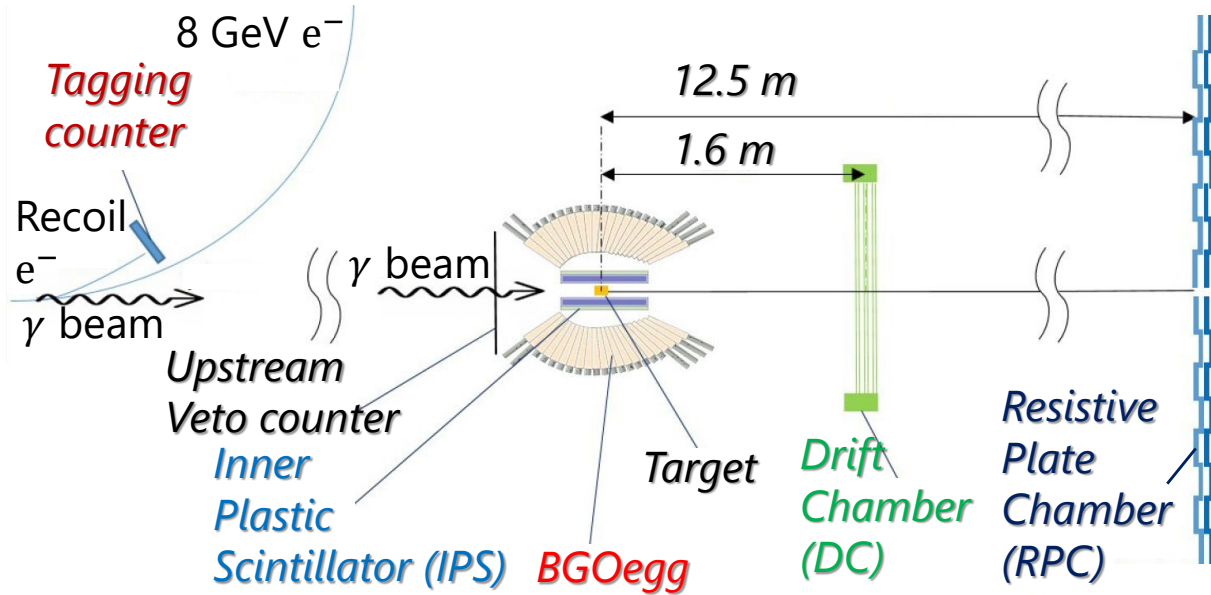


Figure 2.5: A schematic drawing of LEPS2/BGOegg experimental setup (Top view).

in which an incident photon were converted to an e^+e^- pair when it was transmitted to the experimental hall was excluded using an Upstream Veto counter. The η mesons were identified from the invariant mass of $\gamma\gamma$ s with the BGOegg calorimeter. Charge identification for particles incident on the BGOegg calorimeter was performed by Inner Plastic Scintillator (IPS). The scattered protons were detected using the BGOegg calorimeter or the Drift Chamber (DC). Details of each detector are described in the following sections.

2.2.1 Beam tagging counter

The energy of a BCS photon is measured by reconstructing the track of a recoil electron with the tagging counter system (tagger). Figure 2.6 shows a schematic drawing of the tagger. The tagger consists of two layers of 1 mm-wide scintillating fiber bundles (Tagger-fiber) and two layers of 8 mm-wide plastic scintillators (Tagger-PL). The Tagger-fiber has 80 counters per layer and the Tagger-PL has 12 counters per layer. The position of the recoil electron hit at the Tagger-fiber corresponds to the momentum of the recoil electron, and hence the photon beam energy. The Tagger-PL is used to generate a tagger logic signal, which makes a trigger for data acquisition. The hit rate of the tagger logic signal is counted by a scaler to monitor the photon beam flux.

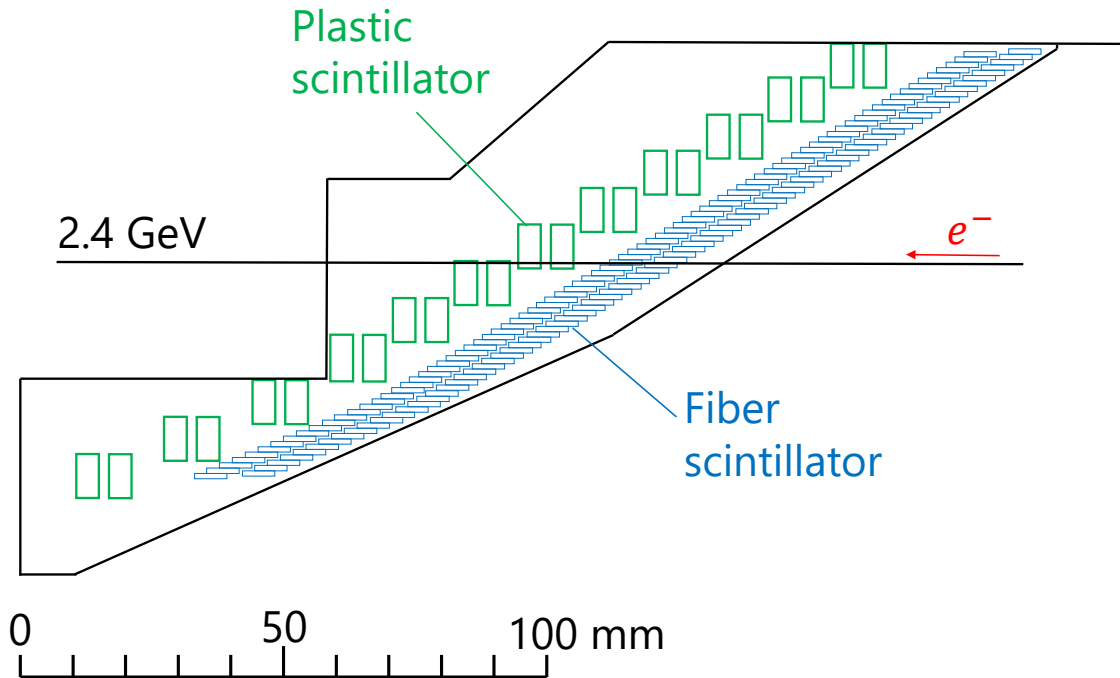


Figure 2.6: A schematic drawing of the tagging counter

2.2.2 Upstream Veto counter

The Upstream Veto (UpVeto) counter is a plastic scintillator for detecting charged particles. Figure 2.7 shows a photograph of the UpVeto counter. It was placed 1.0 m upstream of the target to exclude events in which the photon beam is converted to an e^+e^- pair before reaching the target due to the materials in the beamline. This counter is 620 mm high, 620 mm wide and 3 mm thick. A fine mesh PMT, HAMAMATSU Photonics H6614-70mod, is connected to the plastic scintillator with a light guide. The overveto rate by UpVeto counter was estimated to be $99.878 \pm 0.004\%$. The overveto loss is negligibly small.

2.2.3 Target

A liquid hydrogen target was used in this experiment. A cylindrical target cell, made of thin polyimide films, is placed in the center of the BGOegg calorimeter. A refrigerator that is connected to a hydrogen gas tank liquefies a part of the sealed gas, and fills the target cell with liquid hydrogen. The measured thickness

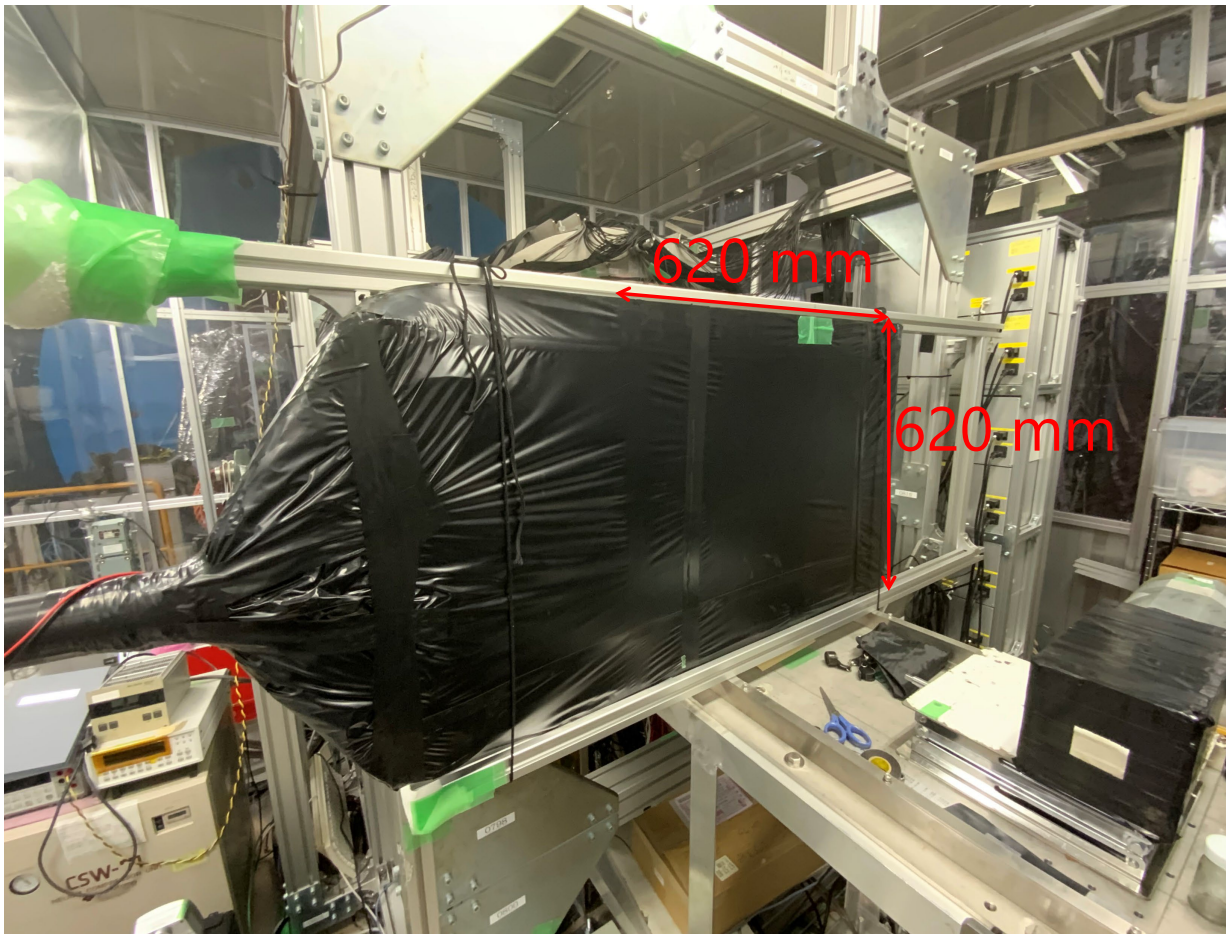


Figure 2.7: A photograph of the UpVeto counter

of the target cell is 54.0 mm, and the density is 0.0708 g/cm³.

2.2.4 BGOegg calorimeter

The BGOegg calorimeter is an egg-shaped electro-magnetic calorimeter, which consists of 1320 bismuth germanate (BGO) crystals. Figure 2.8 shows a schematic view of the BGOegg calorimeter. The BGOegg calorimeter has 22 layers in the polar angular direction, covering from 24 to 144 degrees. Each layer consists of 60 crystals and covers whole azimuthal angles. No support frames are inserted between the crystals, and thus there is no insensitive area. The length of each crystal in the radial direction is 220 mm, which value corresponds to 20 radiation lengths. The energy calibration for each crystal has been done by iteration so that a distribution for the invariant mass of two γ 's, one of which deposits the largest fraction of its energy to the calibrated crystal, should have a peak at the nominal π^0 mass [15]. The energy resolution of the BGOegg calorimeter was evaluated to be 1.4% at the incident γ energy of 1 GeV [28]. The invariant mass resolution of the π^0 is 6.7 MeV/ c^2 with a 20 mm thick carbon target. These resolutions are the world's best among the experiments conducted in a similar energy range.

2.2.5 Inner plastic scintillator

The Inner Plastic Scintillator (IPS) is a hodoscope in order to identify charged particles incident on the BGOegg calorimeter. The IPS is located between BGOegg and the target. Figure 2.9 shows a schematic drawing of the configuration of BGOegg and IPS. IPS consists of 30 slats of 453 mm-long and 5 mm-thick scintillators side by side in a cylindrical shape as shown in Fig. 2.10. The energy deposition signal of a charged particle was read out by Multi-Pixel Photon Counters (MPPC) from the upstream end of individual IPS slats.

2.2.6 Drift chamber

The Drift Chamber (DC) is a wire chamber for detecting charged particle tracks. Figure 2.11 shows a schematic drawing of the DC. The DC consists of six hexagonal planes whose circumscribed circle has a diameter of 1600 mm. Figure

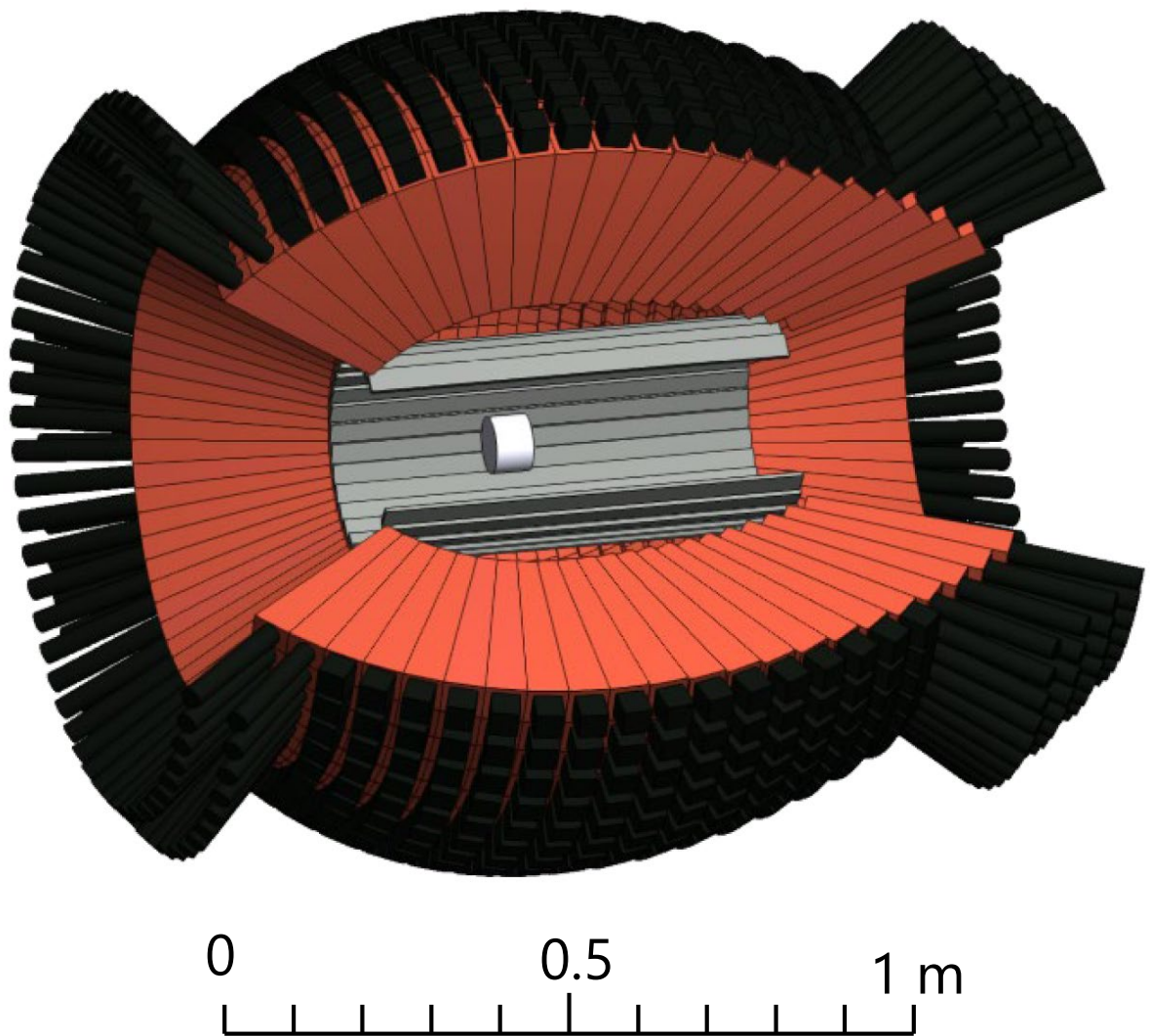


Figure 2.8: A schematic drawing of the BGOegg calorimeter

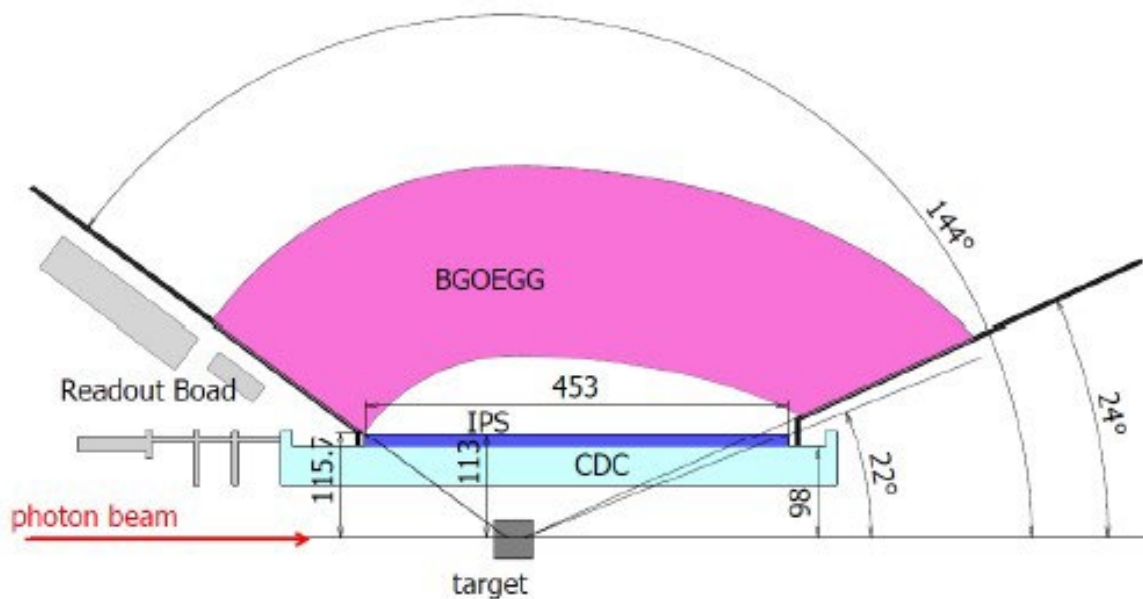


Figure 2.9: A schematic drawing of the configuration of BGOegg and IPS.

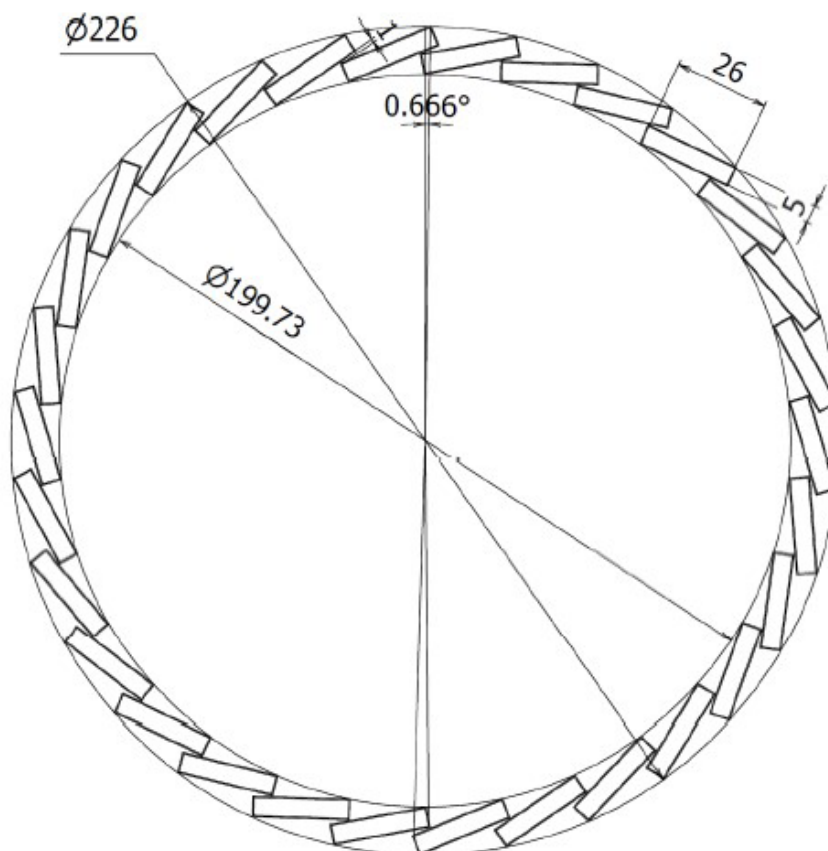


Figure 2.10: A front view of IPS.

2.12 shows an internal structure of the DC. These six planes are classified by wire directions and named X, X', U, U', V, and V'. The tilt angles of X, U, and V are 0, 60, and -60 degrees, respectively. The coordinates that can be measured by the DC are those perpendicular to the wire directions, which we define as y , u , and v in the laboratory system as shown in the Fig. 2.12. Each plane has 80 sense-wires and 81 potential-wires with a wire interval of 8 mm. As shown in Fig. 2.12, the wire structure is shifted by 8 mm between pair planes with the same direction. The position resolution at each plane when reconstructing the charged particle trajectory with a straight line fit is about $300 \mu\text{m}$. The detailed values are listed in Table. 2.1. The DC is placed at 1.6 m downstream of the target, covering polar angles less than 21 degrees.

Table 2.1: Position resolutions at each plane

Plane	Position resolution (μm)
X	326.8
X'	321.9
U	301.2
U'	319.1
V	289.7
V'	293.1

2.2.7 Resistive plate chamber

The Resistive Plate Chambers (RPCs) are gas chambers for measuring a Time-Of-Flight (TOF) of charged particles. Figure 2.13 shows a schematic drawing of a TOF wall consisting of 32 RPCs. The TOF wall is located at a distance of 12.5 m from the target to measure the momentum of protons emitted to very forward angles ($< 6.8^\circ$). An RPC is 250-mm wide and 1000-mm long [29, 30]. There are eight readout strips along the vertical direction in a chamber, and hit signals are read at both top- and bottom-ends. The timing resolution of the RPC varies from individual to individual and is 60–90 ps. It provides a good momentum resolution of less than 1% for an incident proton of 2 GeV/c.

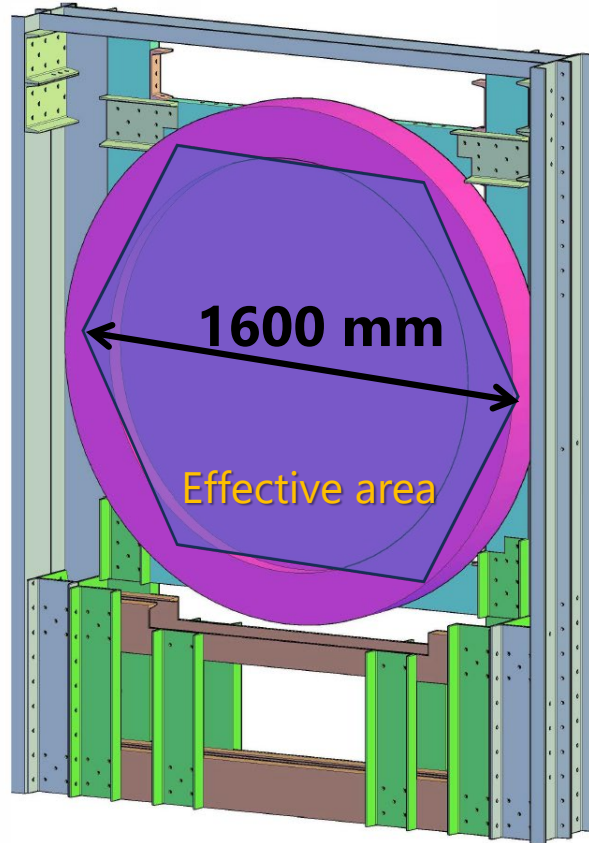


Figure 2.11: A schematic drawing of the DC.

2.2.8 RF signal

SPRING-8 uses the 508.579343 MHz radio frequency (RF) system to accelerate an electron beam. Therefore, the electrons in the storage ring have a bunch structure, where the time interval between successive bunches is 1.966 ns. There are 2436 packets in total, but not all packets are filled with electrons. Several bunch-filling modes are summarized in Appendix B. The timing resolution of the RF signal is 12 ps, which is far better than the other detectors' timing resolutions. We used the RF signal to accurately determine the event start timing for the TOF measurement.

2.3 Data acquisition system

In this section, we describe the readout electronics and the trigger system in the LEPS2/BGOegg experiment.

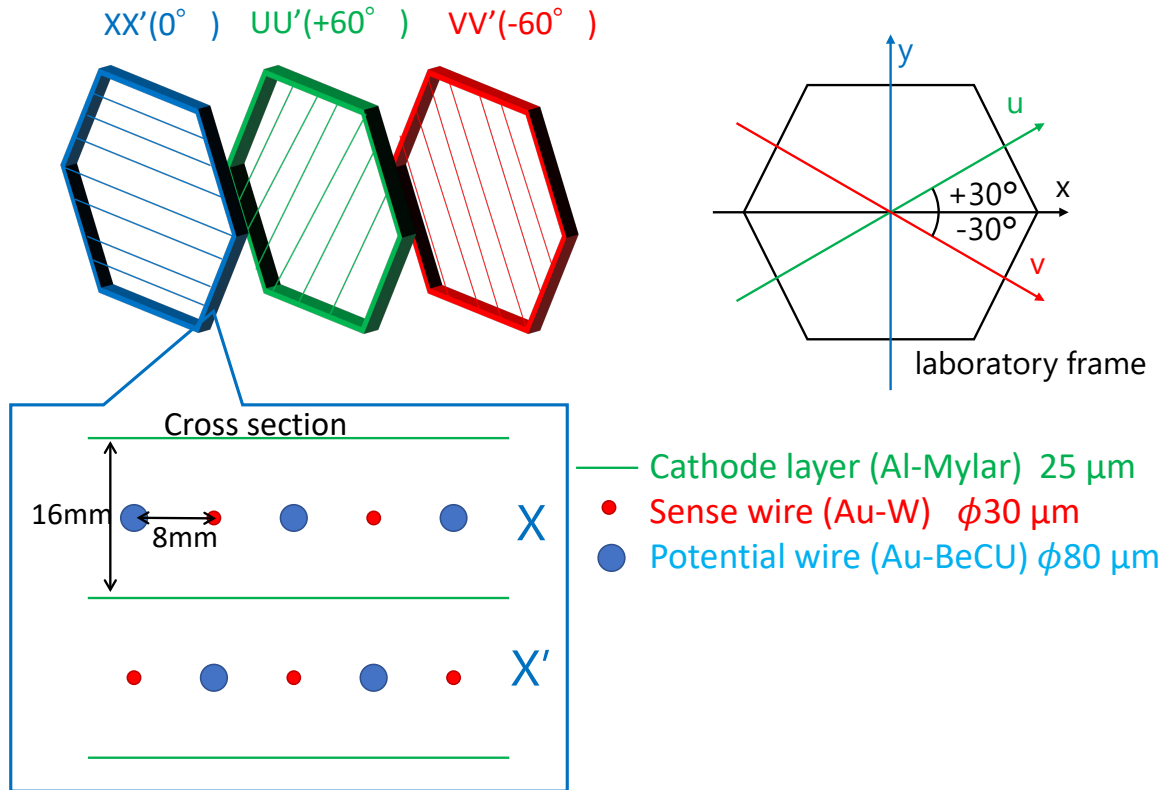


Figure 2.12: An internal structure of the DC.

2.3.1 Electronics

Table 2.2: Digitizers for each detector

Detector	ADC	TDC
Tagger-PL	VME V792	VME V1190
Tagger-fiber	none	VME V1190
UpVeto	VME V792	VME V1290N
BGOegg	FERA 4300B	VME V1190
IPS	VME V792	VME V1290A
DC	none	LeCroy 3377
RPC	FERA 4300B	VME V1290A
RF	none	VME V1290A/N

Table 2.2 summarizes the digitizers to read out the signals from the LEPS2/BGOegg detector. We used two types of the analog-to-digital converter (ADC) to measure signal charge. LeCroy FERA (Fast Encoding and Readout ADC) 4300B modules were used for BGOegg and RPC. For Tagger-PL, UpVeto, and IPS, CAEN VME (Versa Module Europe) V792 ADC modules were used. Timing information was recorded using three types of the time-to-digital converter (TDC)

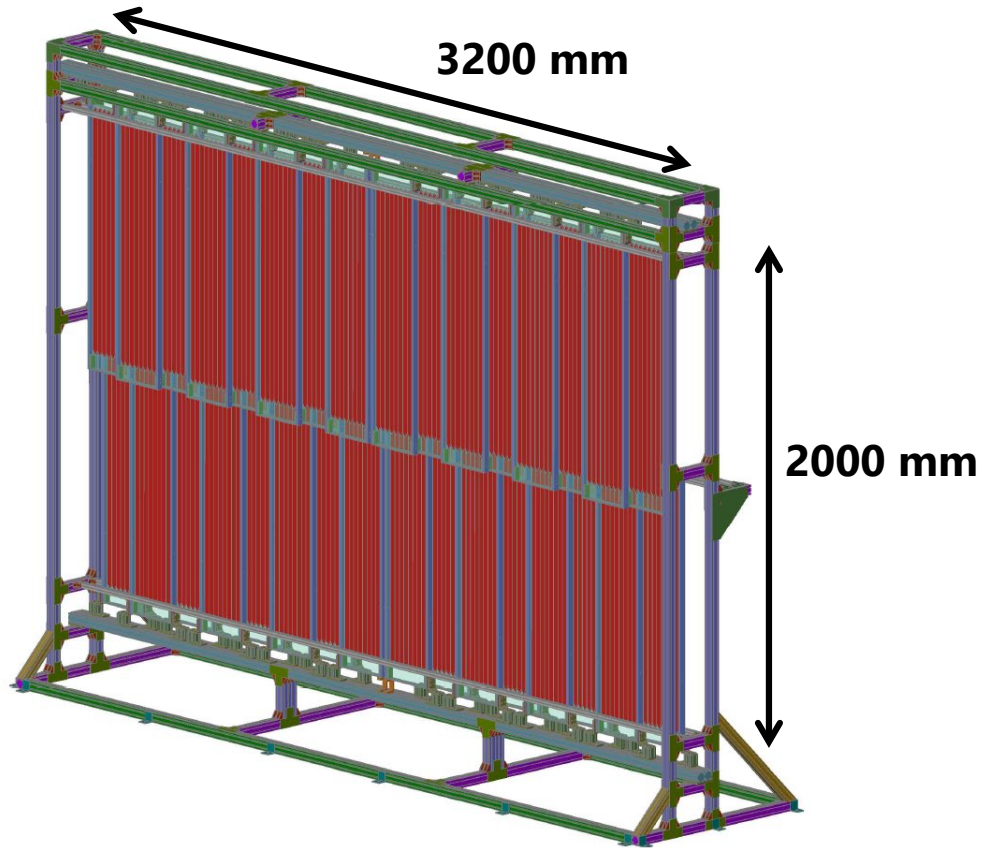


Figure 2.13: A schematic drawing of the RPC wall

modules. CAEN VME V1190 TDC modules were used for the Tagger-PL, Tagger-fiber, and BGOegg. For the UpVeto, IPS, and RPC, CAEN VME V1290 TDC modules were used. The difference between the V1290A and V1290N is the number and shape of input channels. We utilize LeCroy 3377 TDC modules for DC.

2.3.2 Trigger

Trigger signals for data acquisition were generated from the tagging system and the BGOegg calorimeter. A schematic drawing of the trigger logic is shown in Fig. 2.15. In the tagging system, when paired tagger plastic scintillators both have hits, a Multi-Purpose Logic Module (MPLM4) [31] generated a trigger signal. For the BGOegg calorimeter, when more than two crystals of the BGOegg calorimeter had hits, a GeV- γ 139 module [32] generated a trigger signal. The LeCroy 4413 discriminator module used for BGOegg has a current sum output. It gave a signal proportional to the number of channels which exceed the threshold. This threshold corresponded to an energy deposition of 10 MeV.

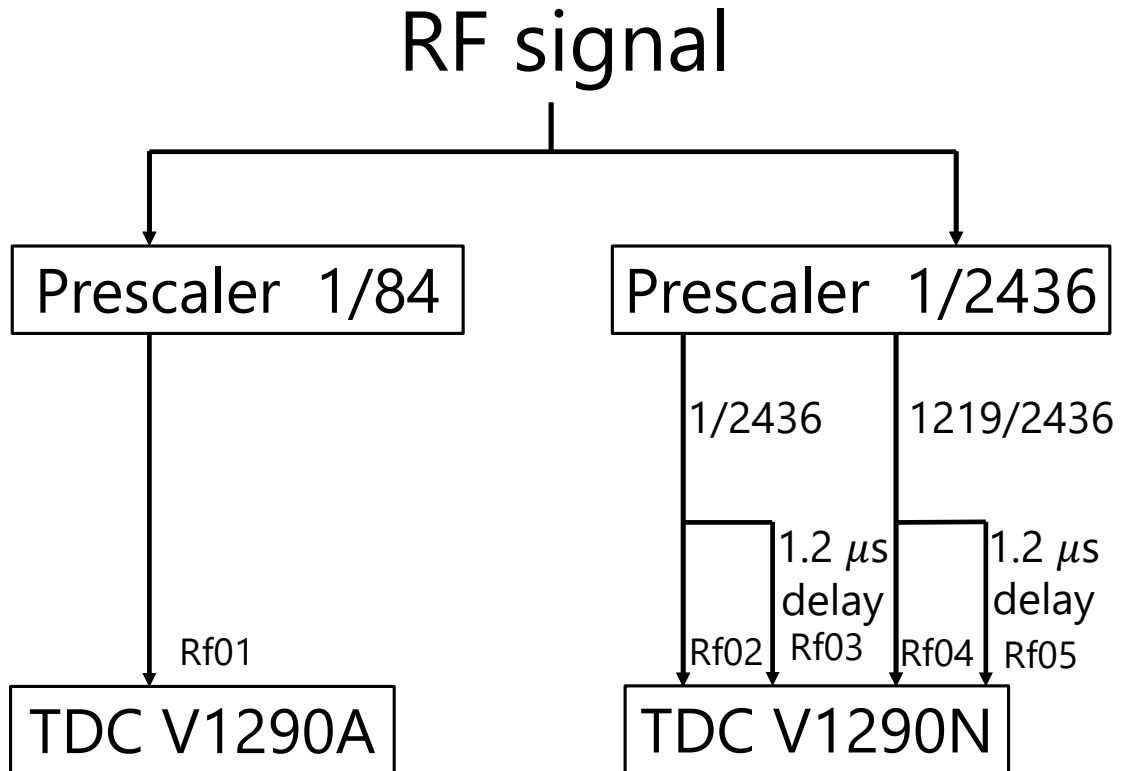


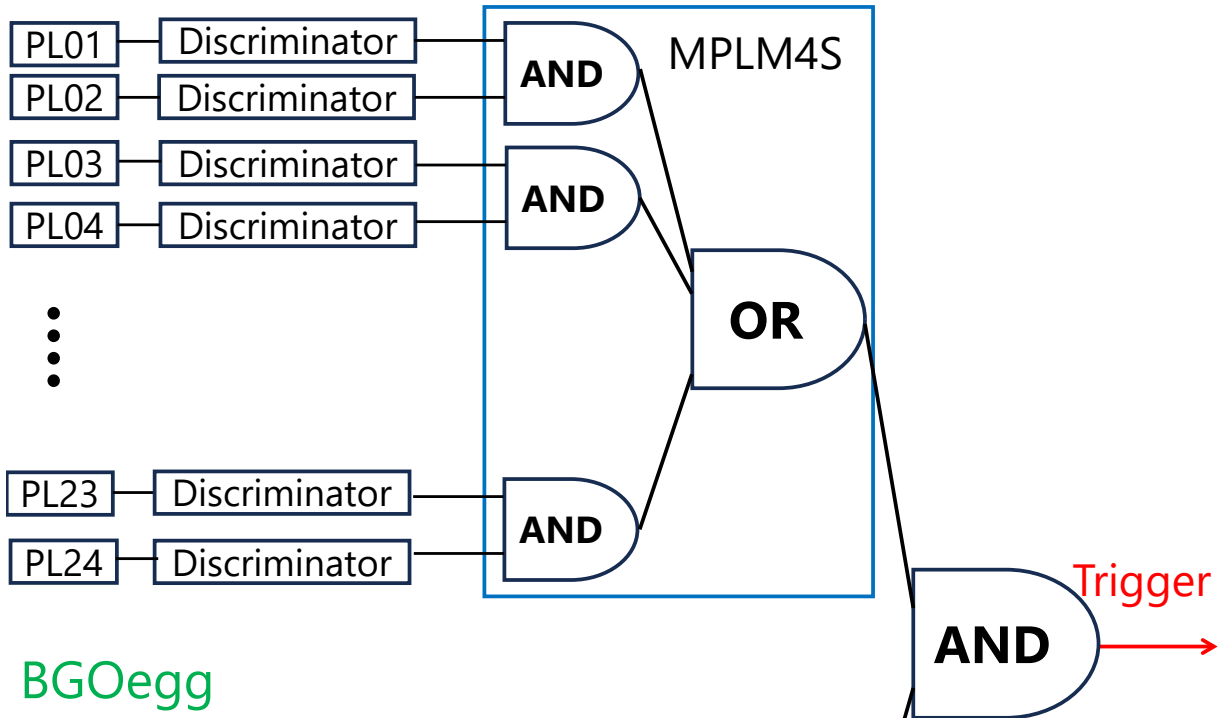
Figure 2.14: A schematic drawing for the RF signal readout.

The GeV- γ 139 module summed up signals from all the discriminators. Trigger signal was generated when two or more crystals of the BGOegg calorimeter had hits. This was the minimum bias trigger for BGOegg to detect more than two γ 's. Matching timing hits were required for the tagger signal and the BGOegg signal.

2.4 Data summary

The experiment was carried out from November in 2014 to February in 2015. The total number of BCS photons was 3.593×10^{12} after considering DAQ efficiency and dead time correction of scaler, which details were shown in Sec. 3.1.3. Multiplying this by the transmission ratio gave the number of photons incident on the target. The transmission ratio is described in Sec. 3.1.4.

Tagger



BGOegg

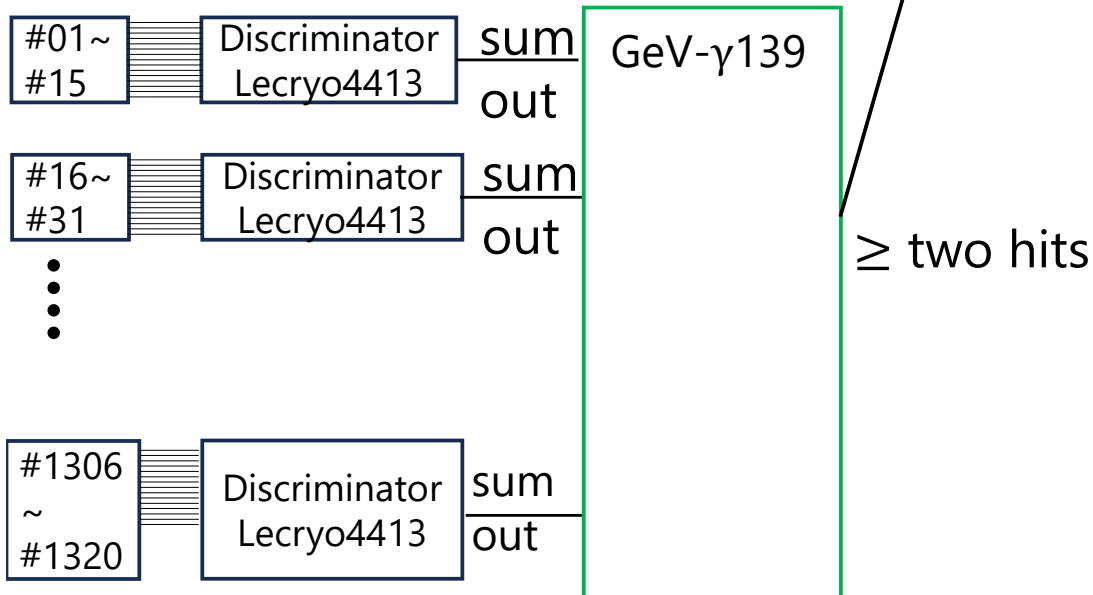


Figure 2.15: A schematic drawing of the trigger logic.

Chapter 3

Data Analysis

This chapter describes the data-analysis procedure to obtain differential cross sections and photon beam asymmetry for η photoproduction on the proton. An η meson is identified by detecting γ 's from its neutral decay: $\eta \rightarrow \gamma\gamma$. The branching ratio of this decay is $39.41 \pm 0.20\%$. These decay products are detected with the BGOegg calorimeter and a recoil proton is detected with the BGOegg calorimeter or the DC.

3.1 Photon beam measurement

3.1.1 Tagger track reconstruction

A BCS photon was identified by the corresponding recoil electron track. The following procedure was used to reconstruct the recoil electron track. First, the recoil electron must hit one or two layers of the scintillating fibers and both geometrically corresponding plastic scintillators. Second, the timing difference between the plastic scintillators was required to be within ± 0.8 ns as shown in Fig. 3.2 to remove electron tracks coming from other electron bunches existing every 2 ns. The plastic scintillator hit timings were finally averaged to obtain a detection time of the reconstructed track. Its timing resolution is 170 ps, which is good enough to distinguish the reconstructed track with the tracks coming from other electron bunches. Third, the timing cut was applied for the timing difference between the plastic scintillators and scintillating fibers as shown in Fig. 3.3. The cut region was -2.5 to 2.0 ns. Since the energy of the photon beam could not be uniquely determined when there were multiple reconstructed

tracks, events with only one reconstructed track were used for analysis.

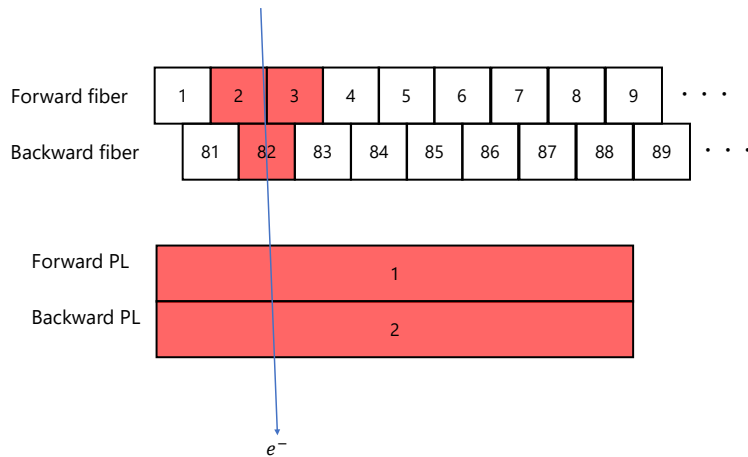


Figure 3.1: A schematic drawing of the tagger and an example of an electron track.

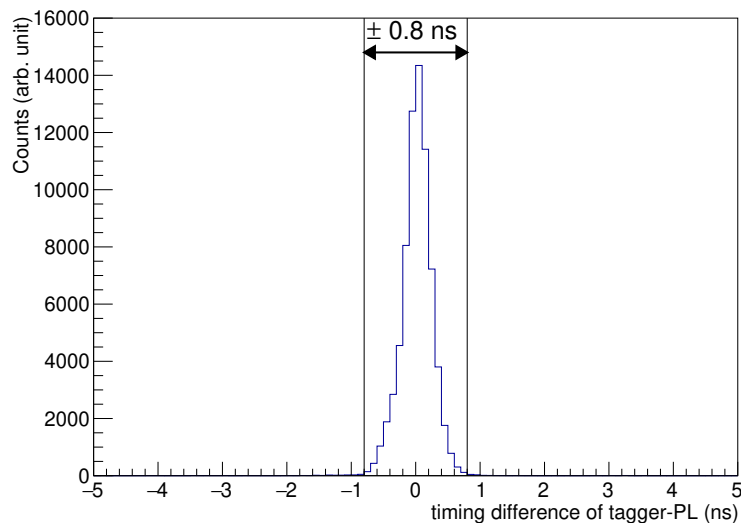


Figure 3.2: The timing difference between the tagger plastic scintillators.

The tagger reconstruction efficiency was evaluated by using $\gamma p \rightarrow \pi^0 \pi^0 p$ reaction to compensate for the signal loss due to track reconstruction failure in the analysis, multi-track detection in the tagger, and inefficiencies of tagger fibers. The reconstruction efficiency varies from 0.86 to 0.93 depending on the photon beam energy. The typical uncertainty of this reconstruction efficiency is 0.7%. Details are provided in the Appendix E. The electromagnetic shower contamination rate due to high momentum recoil electrons hitting the walls

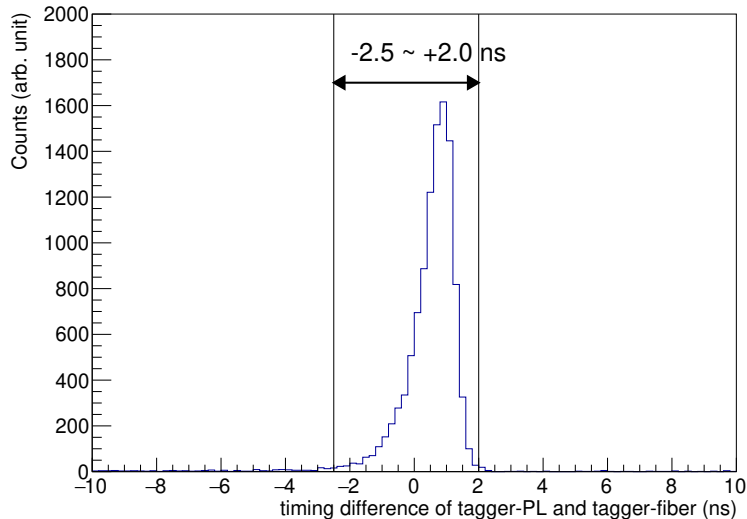


Figure 3.3: The timing difference between the tagger plastic scintillators and scintillating fibers.

of the vacuum chambers upstream of the tagger was estimated to be 0.0424 ± 0.0006 at the tagger trigger level.

3.1.2 Beam energy calibration

The energy of a BCS photon is uniquely determined from the momentum of a recoil electron. Since the momentum of the recoil electron corresponds to the hit position of the tagging system, the photon beam energy of each event is obtained from the hit position in the tagger. We evaluated the photon energy functions as a fourth-order polynomial of the Tagger-fiber hit position. Since Tagger-fiber has two layers, forward and backward, we prepared photon energy functions for forward ($E_{\gamma f}$) and backward ($E_{\gamma b}$) fiber layers corresponding to the Tagger-fiber forward (x_f) and backward (x_b) hit position, respectively as

$$E_{\gamma f} = a_f + b_f \times x_f + c_f \times x_f^2 + d_f \times x_f^3 + e_f \times x_f^4 (\text{MeV}), \quad (3.1)$$

$$E_{\gamma b} = a_b + b_b \times x_b + c_b \times x_b^2 + d_b \times x_b^3 + e_b \times x_b^4 (\text{MeV}), \quad (3.2)$$

When a track contained both of forward and backward fiber hits, the photon beam energy E_γ was obtained as the average of $E_{\gamma f}$ and $E_{\gamma b}$. We derived these photon energy functions using a kinematic fit in the $\gamma p \rightarrow \pi^0 \pi^0 p$ reaction. By

Table 3.1: Coefficients of photon energy functions

coefficient	value	coefficient	value
a_f	1250.7 ± 0.9	a_b	1266.0 ± 1.5
b_f	34.912 ± 0.069	b_b	34.486 ± 0.25
c_f	-0.27172 ± 0.00203	c_b	-0.25291 ± 0.00478
d_f	$0.55498 \pm 0.00489 \times 10^{-2}$	d_b	$0.49325 \pm 0.03234 \times 10^{-2}$
e_f	$-0.77346 \pm 0.01052 \times 10^{-4}$	e_b	$-0.72442 \pm 0.07751 \times 10^{-4}$

measuring the momentum of all particles in the final state using the BGOegg and RPC, the beam energy was back-calculated from the energy and momentum conservation laws to obtain the correspondence with the Tagger-fiber hit position. More details are provided in the Appendix D. The photon energy resolution was evaluated using the $\gamma p \rightarrow \pi^0 \eta p$ reaction. MC simulation was used to obtain the resolution of the momentum of mesons such as π^0 and η reconstructed by using the BGOegg calorimeter and a proton detected by using the RPC. From these resolutions, the resolution of the predicted photon beam energy was calculated, and the standard deviation of the difference between the measured photon beam energy and predicted photon beam energy from a kinematic fit was obtained. By subtracting the contribution of the predicted photon beam energy, the measured photon beam energy resolution was estimated to be 12.1 ± 0.7 MeV. This resolution was predominantly influenced by the electron beam emittance in the SPring-8 storage ring.

3.1.3 Tagging photon counting

The photon beam flux was obtained by counting the tagger logic signals. The tagger logic signals have a finite width of 20 ns, which causes them to be miscounted. It is necessary to estimate and correct the miscount rate to obtain accurate photon beam flux. This miscount rate depends on the tagger rate and the electron filling pattern at SPring-8 [33]. Therefore, correction factors should be obtained for each filling pattern. Details of calculating correction factors are provided in the Appendix C. The integrated counts of tagger scalers after considering these correction factors reach of 3.593×10^{12} in this analysis.

3.1.4 Beam transmission

A part of the BCS photons did not reach the target because of pair creations at materials in the LEPS2 beamline. A photon beam transmission T_γ was evaluated to be 0.772 based on a calculation considering the amount of materials. The uncertainty given by the measurement accuracy of the material thickness was smaller than 1%. In addition, the beam transmission requires a beam energy-dependent correction factor F_{trans} . As shown in Fig. 3.4, when the injected laser light was focused in the wrong point from the designed BCS point unexpectedly, a peripheral region of the photon beam was cut off at a collimator, located 25 m downstream from the designed BCS point.

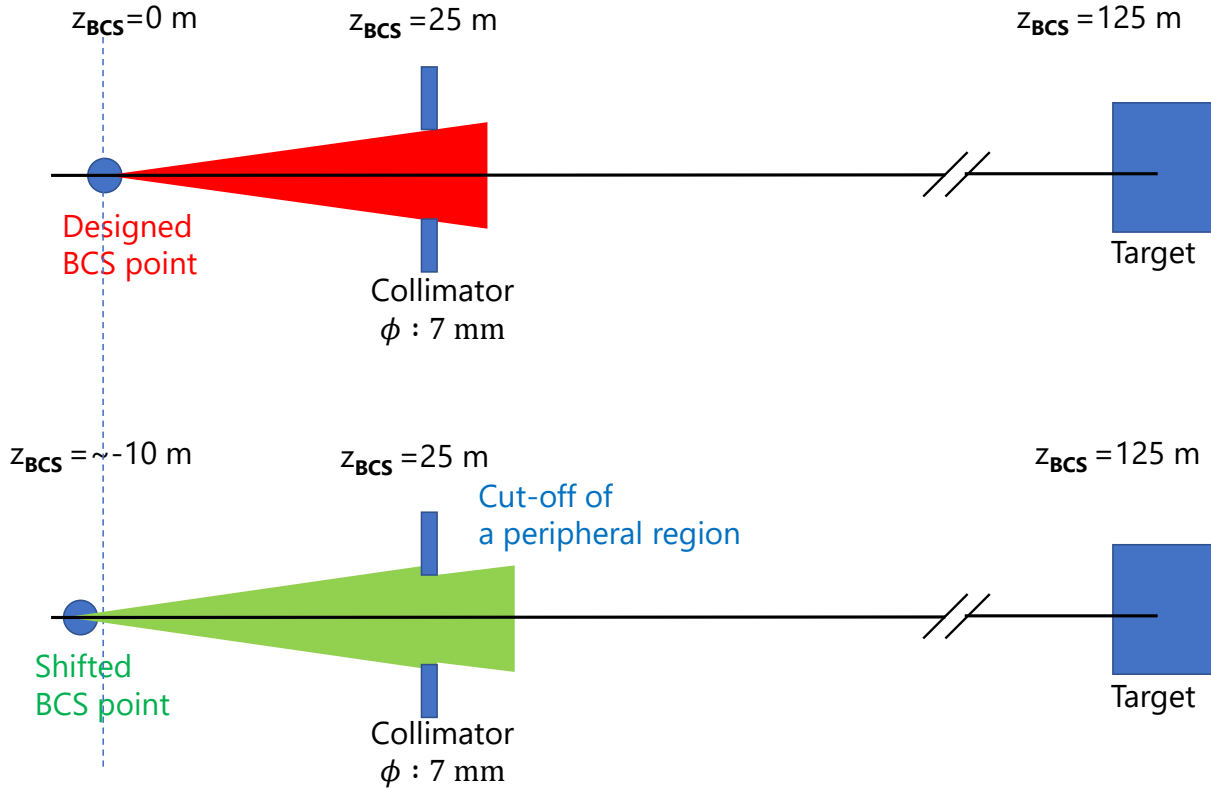


Figure 3.4: A schematic drawing of beam transmission

As expressed in Eq. 2.2, when the cone angles θ_2 is large, the energy of the BCS photon is low. Therefore, the photon beam loss is greater at lower energies. The correction factor F_{trans} was derived from the ratio of inclusive π^0 yields to tagging photon counts in each energy bin. Assuming that the detection efficiency of π^0 mesons at the BGOegg calorimeter and the target length was constant, the variation in the number of photons reaching the target

was estimated from the variation in the ratio of π^0 yields to tagging photon counts ($R_{\pi^0/\gamma_{\text{tag}}}$). First, in the period with a good laser focal length, the BCS happened at the ideal position as shown in the upper part of the Fig. 3.4, therefore the beam transmission is constant regardless of the photon beam energy. For this period, we let $R_{\pi^0/\gamma_{\text{tag}}}^{\text{good}}$ be the ratio of π^0 yields to tagging photon counts. Second, the $R_{\pi^0/\gamma_{\text{tag}}}$ for the entire period was normalized using the $R_{\pi^0/\gamma_{\text{tag}}}^{\text{good}}$. Since the cone angles θ_2 was small at higher energies, the beam loss due to the shift of the BCS point did not occur. The obtained value at the highest energy bin was 1 within the statistical uncertainty. Finally, we renormalized the correction factor to 1 at the highest energy bin. The energy-dependent transmission correction factor was obtained as below

$$F_{\text{trans}}(E_\gamma) = 1 + a_{\text{trans}} \times (2300 - E_\gamma) + b_{\text{trans}} \times (2300 - E_\gamma)^2,$$

$$a_{\text{trans}} = 1.206 \pm 2.954 \times 10^{-5}, b_{\text{trans}} = -1.113 \pm 0.370 \times 10^{-7},$$

as shown in Fig. 3.5.

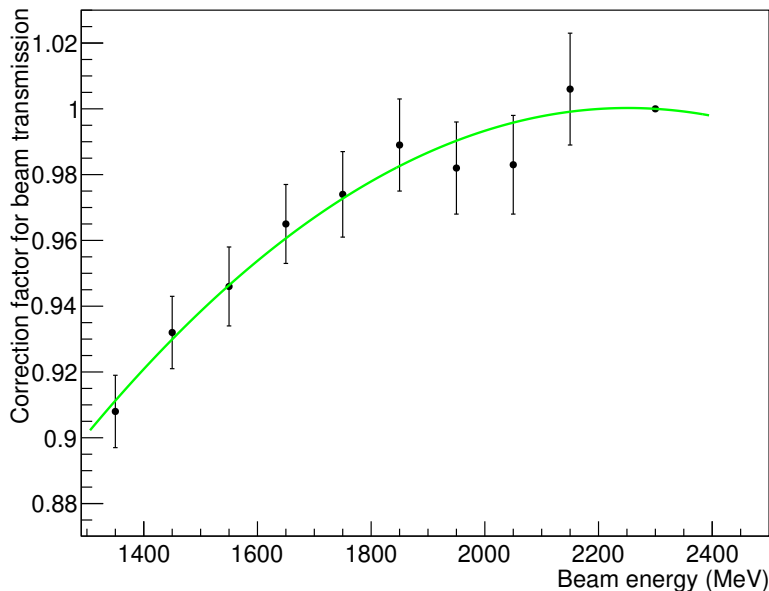


Figure 3.5: The energy-dependent correction factor for beam transmission.

3.2 Reaction timing reference

Since the electron beam at SPring-8 is synchronized with the RF signal, the BCS reaction with the laser photon also occurs in synchronization with the RF signal. The RF signal timing was used as a reference of the reaction timing at the target. The RF signal was prescaled with a factor $1/84$, and the recorded RF signal timing did not necessarily coincide with the electron bunch that caused the BCS photon. The RF signal timing has $1.966 \times n$ ns ambiguity when determining the BCS reaction timing, where 1.966 ns is the electron bunch interval in the SPring-8 storage ring, and n is an integer from 0 to 83. To resolve the ambiguity, we used the tagger timing. Figure 3.6 shows the timing difference between the tagger plastic scintillator hit and the prescaled RF signal.

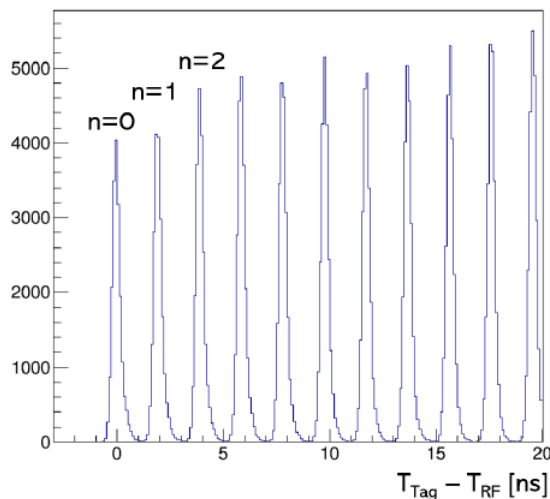


Figure 3.6: The timing difference between the tagger plastic scintillator hit and the RF signal.

3.3 Measurement of final-state particles

In this analysis, we detected two photons and one proton as the final-state particles. The BGOegg calorimeter was able to detect both photons and charged particles in the polar angular range from 24 to 144 degrees. The charged particles in this region deposited energy in the IPS, and could be distinguished from photons. On the other hand, charged particles emitted at a polar angle

of less than 21 degrees and 4.4 degrees were detected using the DC and RPC, respectively. The details of the analyses are described in the following sections.

3.3.1 Reconstruction of particles with the BGOegg calorimeter

The BGOegg calorimeter can detect both photons and charged particles. The four-momenta of photons were obtained from the energy and angle information, whereas, only the angles of charged particles with respect to the target were measured. The details of the analysis procedure are described below. γ 's from a meson decay are detected by using the BGOegg calorimeter. The front size of individual BGO crystals is a little smaller than the Moliere radius for BGO, which is 22.3 mm. Therefore, an electromagnetic shower of a γ leaves its energy in multiple crystals around a core where the γ is incident. The crystals with energy depositions were grouped into a "cluster". This cluster consists of several hits in main crystals whose energies were larger than the discriminator threshold set at 10 MeV and neighboring peripheral crystals with smaller energies. The cluster energy was a sum of all the cluster members. A crystal with the largest energy was adopted as the core of a cluster. The timing of a cluster was determined by using the core crystal. The center of a cluster was evaluated from the energy-weighted average of the hit crystal positions. The four-momentum of a γ was reconstructed assuming that this γ came from the center of the target. A charged particle was also reconstructed using the same method as the γ , but in many cases the charged particle penetrated the calorimeter, so the magnitude of this momentum could not be measured.

3.3.2 IPS charge identification

The IPS was used to identify the charge of a cluster. First, we selected the IPS channel that located on the line connecting the center of the cluster and the target center. Second, we obtained the energy deposition and the timing of the corresponding IPS channel. If the energy loss in this IPS channel was greater than 0.8 times that of minimum ionizing particles and the timing difference between the RF signal and the IPS hit was within $3 \sigma_{\text{IPS}}$, where σ_{IPS} stands for the standard deviation of the timing difference and its value was 0.22 ns,

then we treated the corresponding cluster as a charged cluster. Otherwise, all other clusters were treated as neutral clusters. In this analysis, we treat neutral clusters as γ 's and charged clusters as protons. The proton detection efficiency of IPS was evaluated to be 0.9863 ± 0.0009 .

3.3.3 DC tracking

The DC measured the track of a charged particle. Charged particles ionized the gas inside the DC as they pass through the DC. The electrons produced by ionization drifted in the electric field, producing a signal. The hit positions of the charged particle's were determined by taking into account the drift time of the electrons. Straight line tracking was performed using hit positions on each of the six planes in DC to obtain angular information on the track of the charged particle. To improve the position resolution, the fit was performed by assuming the charged particles came from the target and including the target position as an additional constraint. Tracks were considered to be correctly reconstructed when the χ^2 probability of fitting was greater than 0.01. The tracking efficiency was evaluated to be 0.9824 ± 0.0044 . This efficiency included both the detection and reconstruction efficiency.

3.3.4 TOF measurement

The RPC measured the TOF of a charged particle. The start time is when the reaction occurs in the target, which is determined by the RF signal. Next, the flight-length was determined from the hit position in the RPC and the target position, and the velocity of a charged particle was calculated. The hit positions in the horizontal (x) and vertical (y) directions were obtained from the channel number of the hitting strip and the timing difference of the hit signals that were read out at the top- and bottom-ends of a strip, respectively. The position resolutions in the two directions were $\sigma_x = 7.5$ mm and $\sigma_y = 16$ mm. The reconstruction efficiency of an RPC hit was 0.931 ± 0.023 . The momentum of the detected particle was determined by assuming the proton mass. Protons are separated from charged pions and electrons by the velocity information requiring that some meson is detected at the BGOegg calorimeter.

3.4 Event selection

3.4.1 Outline of the event selection

In the present analysis, the $\gamma p \rightarrow \eta p$ events were extracted from the data collected with the liquid hydrogen target by identifying the η meson in the decay mode into $\gamma\gamma$, whose branching fraction was 0.3941 ± 0.0020 [15]. We determined the photon beam energy with the tagger by measuring the position of the recoil electron tracks. We selected one recoil electron track because if multiple recoil electron tracks were detected we could not uniquely determine the photon beam energy. We required that there was no hits in the UpVeto to exclude events in which a beam photon was converted to an e^+e^- pair while it was transmitted to the experimental hall. An η meson that was produced in the γp reaction immediately decayed into two γ 's in the target. We measured the energies of the γ 's from the energy deposition in the BGOegg calorimeter, and the directions of γ 's as the angle from the target center to the cluster centers in the BGOegg calorimeter. If we found more than two neutral clusters, we rejected the events. We measured the emitted direction of a proton with the BGOegg calorimeter or the DC. We required only one charged track candidate to reduce background events in which multiple charged particles were emitted. We identified η mesons in the invariant mass distribution of two γ 's. We rejected events in which a γ was detected at the edge layer of the BGOegg calorimeter to measure the energy deposition correctly. We performed a kinematic fit with the five constraints: the four-momentum conservations and the $\gamma\gamma$ invariant mass to be consistent with the nominal η mass. In summary, we required the following conditions:

1. One recoil electron track in the tagger,
2. No charged particles detected with the UpVeto,
3. Two neutral clusters at the BGOegg,
4. One charged cluster at the BGOegg or one charged track at the DC,
5. No neutral clusters at the edge layer of the BGOegg calorimeter,
6. χ^2 probability of kinematic fit is more than 0.01.

Table 3.2 summarizes the reduction factor for each cut condition.

Table 3.2: Cut conditions and reduction factors in real data

cut name	input	output	reduction factor
Tagger tracks cut	6.37×10^8	2.98×10^8	2.14
No UpVeto hits cut	2.98×10^8	1.50×10^8	1.98
Number of clusters cut	1.50×10^8	1.49×10^7	10.1
DC tracks cut	1.49×10^7	1.28×10^7	1.17
No edge cluster cut	1.28×10^7	6.87×10^6	1.86
Kinematic fit cut	6.87×10^6	6.60×10^4	104

3.4.2 Recoil electron track in the tagging system

It is necessary to select a recoil electron track that corresponds to the beam photon that caused the reaction at the target. We selected the event in which the timing difference between the RF signal corresponding to the reaction at the target and the BCS reaction was within ± 1.0 ns. However, the BCS reaction may occur more than once in the same electron bunch, in which case the energy of the BCS photon cannot be uniquely determined. To exclude such events, we required that there was only one recoil electron track whose timing matched the RF signal corresponding to the reaction at the target. Figure 3.7 shows the number of recoil electron tracks corresponding to the reaction at the target. Events in which the beam-photon energy that caused a reaction at the target was able to be uniquely determined were about half of all data.

3.4.3 No UpVeto hits

We excluded the events in which a photon beam converted to an e^+e^- pair before reaching the target. Figure 3.8 shows the signal timing of the UpVeto counter relative to the RF signal, $t_{\text{UpVeto}} - t_{\text{RF}}$ in a unit of the timing resolution of the UpVeto counter ($\sigma_{\text{UpVeto}} = 0.48\text{ns}$). The events around $\frac{t_{\text{UpVeto}} - t_{\text{RF}}}{\sigma_{\text{UpVeto}}} = 0$ were produced by e^+e^- pairs from the beam conversion. We required the following conditions: $\frac{t_{\text{UpVeto}} - t_{\text{RF}}}{\sigma_{\text{UpVeto}}} < -3$ or $\frac{t_{\text{UpVeto}} - t_{\text{RF}}}{\sigma_{\text{UpVeto}}} > 5$.

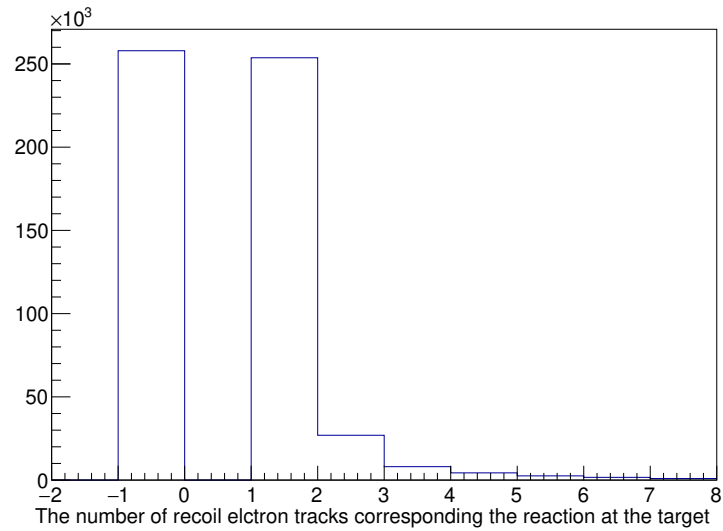


Figure 3.7: The number of recoil electron tracks corresponding to the reaction at the target. Events with a track count of -1 represent events where no track was found in the reaction at the target.

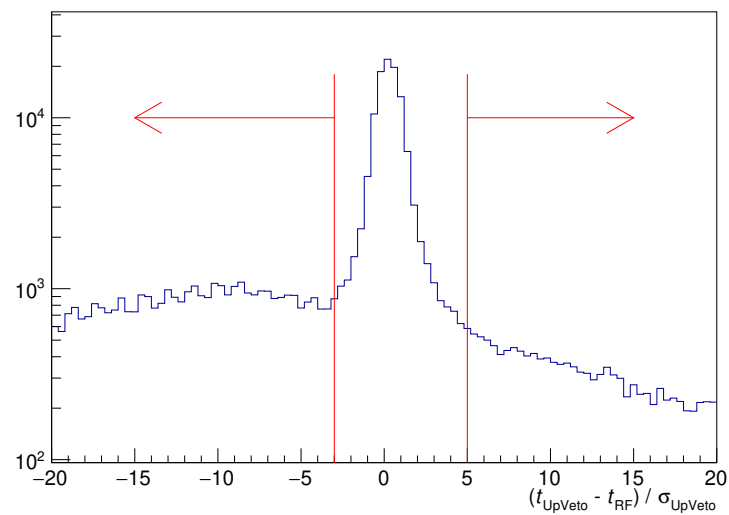


Figure 3.8: The timing difference between the UpVeto counter and the RF signal in a unit of the timing resolution of the UpVeto counter. The red lines and arrows present survived region after the UpVeto cut.

3.4.4 Two γ 's identification

We selected an event with two neutral clusters in the BGOegg calorimeter that satisfied the following conditions as a signal candidate:

1. The energy of a cluster was greater than 50 MeV.
2. The timing difference between a cluster and the RF signal was within ± 3.0 ns.

The details are as follows. As shown in Fig. 3.9, when one γ is incident on the BGOegg calorimeter, two clusters may be produced due to electromagnetic shower leakage. The ones with the smallest energy are called a "leak cluster". The energy of the leak cluster is much smaller than the energy of the incident γ on the BGOegg calorimeter.

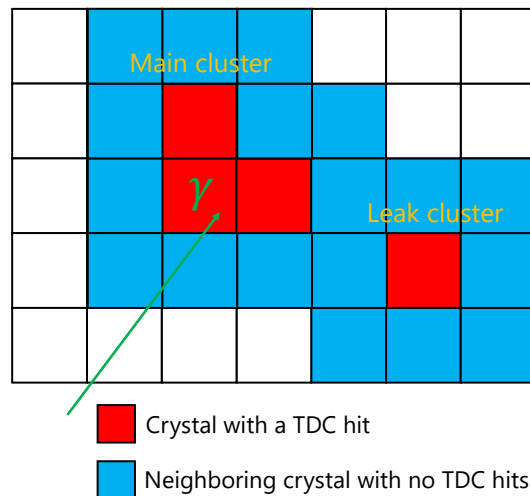


Figure 3.9: An example of a leak cluster.

Figure 3.10 (a) shows the energy distribution of each cluster in MC simulation of an η photoproduction process. The peak at low energy is caused by the leak cluster. Therefore, we required the minimum energy of each cluster to be 50 MeV to reject the leak cluster in counting the number of neutral clusters. The black histogram in Fig. 3.10 (b) shows the timing difference between

the neutral cluster and the RF signal. We required that this timing difference was within ± 3.0 ns in order to remove the events that originated from other electron bunches.

When γ is incident on the most forward or backward edge layer of the BGOegg calorimeter, the electromagnetic shower leaks out of the BGOegg calorimeter. Therefore, the correct cluster energy is not able to be measured. Such events were rejected in reconstructing an η meson.

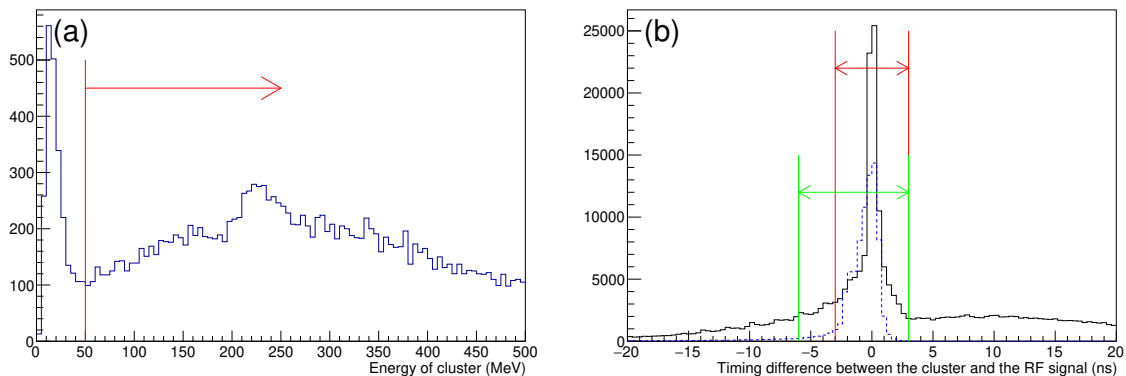


Figure 3.10: The panel (a) shows the energy distribution of a cluster in the MC simulation of an η photoproduction process. The red vertical line presents the energy threshold. The panel (b) shows the timing differences between the cluster and the RF signal. The solid and dashed histograms presents the timing difference using the neutral cluster and charged cluster. The red and green vertical lines present the timing cut region.

3.4.5 Proton identification

A charged particle was measured in the large polar angular range by using the BGOegg calorimeter or the DC. Since it is not possible to identify the type of particle, the analysis proceeded assuming that the charged particles are protons. The BGOegg calorimeter covered the angular range of $24 < \theta_{\text{lab}}^p < 144$ degrees ($-0.5 < \cos \theta_{\text{c.m.}}^\eta < 0.6$). The emitted direction of the charged particles was calculated from the vector connecting the target center position and the position of the core crystal of the charged cluster. The minimum energy condition of the charged cluster was the same as that of the neutral cluster. The timing condition of the charged cluster was a little looser than that of the neutral cluster in order to save the charged particle with low momentum. The blue dashed histogram in Fig. 3.10 (b) shows the timing difference between

the charged cluster and the RF signal. Unlike the case of neutral clusters, the charged clusters with cores in the edge layers of the BGOegg calorimeter were accepted because only the emission angle could be measured.

Charged particles emitted at the angles $\theta_{\text{lab}}^p < 21$ degrees ($\cos \theta_{\text{c.m.}}^\eta < -0.5$) were measured using the DC. We required that the track satisfied the following conditions:

1. Good χ^2 track fitting.
2. Track originated from the target.
3. Not a track derived from e^+ or e^- .

First, we required that the χ^2 probability of the track fitting was larger than 0.01 to select good track fitting. Figure 3.11 shows the χ^2 probability distribution of DC tracking. Secondly, we required that both the x and y coordinates of the track at the target location ($z = 0$ mm) be within ± 50 mm to ensure that the charged particle were generated from a reaction in the target. Thirdly, in order to reject e^+ or e^- tracks, we excluded the tracks that hit the DC in $|x| < 50$ mm or $|y| < 50$ mm. In the case of extremely forward emission angles $\theta_{\text{lab}}^p < 6.8$ degrees ($\cos \theta_{\text{c.m.}}^\eta < -0.95$), it was possible to determine the momentum of the proton because the TOF was measured using the RPC. The total number of charged particles in a reconstructed event was limited to one.

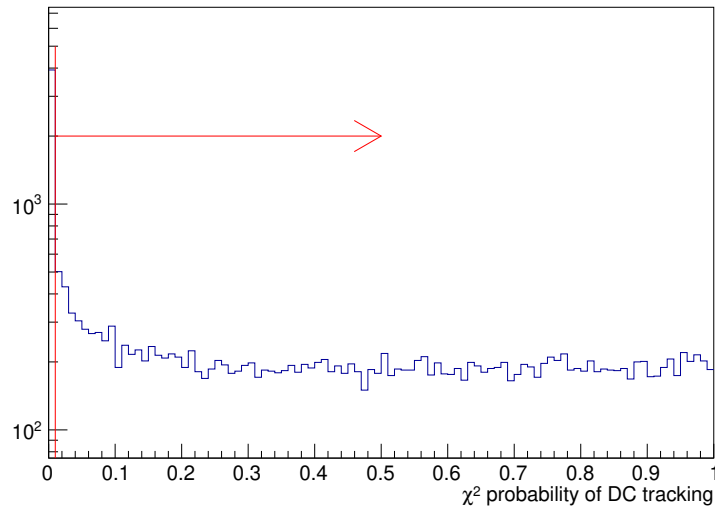


Figure 3.11: The χ^2 probability of DC tracking.

3.4.6 Kinematic fit

After measuring all the final-state particles, a kinematic fit was performed by assuming the reaction $\gamma p \rightarrow \eta p \rightarrow \gamma\gamma p$. Figure 3.12 shows all the variables and constraints in the kinematic fitting method. The constraints were the nominal η mass constraint for the $\gamma\gamma$ invariant mass and the four-momentum conservation between the initial and final states. In the equations of the four-momentum conservation, we assumed that the target was a proton at rest and that the scattered charged particle has the mass of the proton. We treated the absolute value of proton momentum as an unmeasured variable. The measured energy, polar and azimuthal angles were floating parameters that could be within the uncertainties due to the detector resolutions. The position of the reaction vertex along the photon beam direction was adjusted while taking into account the constraint imposed by the target size. The uncertainties of those floating variables in the kinematic fit were estimated by using the GEANT4 [34] based simulation package. Figure 3.13 shows the χ^2 probability distribution of the kinematic fit distribution.

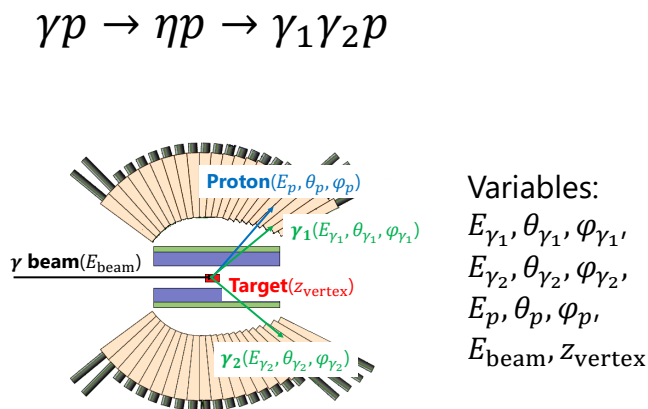


Figure 3.12: The variables and constraints of kinematic fit.

Finally, we required the χ^2 probability of the kinematic fit was greater than 0.01. Figure 3.14 shows the invariant mass distributions for $\gamma\gamma$ pairs detected with the BGOegg calorimeter. The kinematic fit cut successfully removed most of the continuous background. However, the 4-momentum conservation constraints was imperfect because the magnitude of the proton momentum was

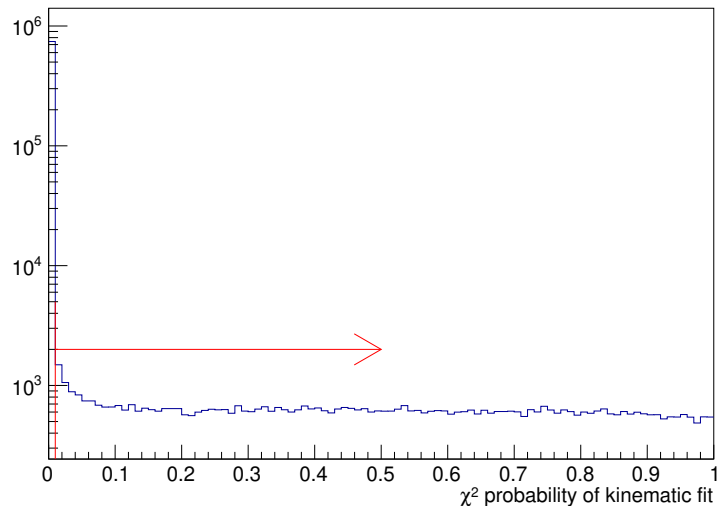


Figure 3.13: The χ^2 probability of the kinematic fit.

not measured. The background contamination after applying kinematic fit cut remained. The typical contamination rate was 10%. The background contamination is discussed in the next section.

3.5 Yield estimation with background subtraction

In order to extract signal yields, we evaluated background contributions in the event sample after applying the selection described in Sec. 3.4.1. After the kinematic fit cut, kinematical distributions of signals and backgrounds become too similar to be distinguished from each other. Therefore, in order to estimate the final contamination rate with the kinematic cut, the contamination rate was determined from the behavior of the individual background shapes using by the template fitting when the loose cut conditions were applied. The loose cut conditions were that the invariant mass of $\gamma\gamma$ must be between 300 MeV/ c^2 and 800 MeV/ c^2 , the missing mass of $\gamma\gamma$ must be between 700 MeV/ c^2 and 1400 MeV/ c^2 , and the opening angle $\cos\theta_{\text{c.m.}}^{\text{opening}}$ between the detected proton and the missing momentum of a $\gamma\gamma$ pair was greater than 0.98 .

Three background reactions were taken into account in the template fitting: $\gamma p \rightarrow \pi^0\pi^0p \rightarrow 4\gamma p$, $\gamma p \rightarrow \pi^0\eta p \rightarrow 4\gamma p$, and $\gamma p \rightarrow \omega p \rightarrow \pi^0\gamma p \rightarrow 3\gamma p$, in which the mesons decayed into multiple γ 's. At first, the signal and above-mentioned

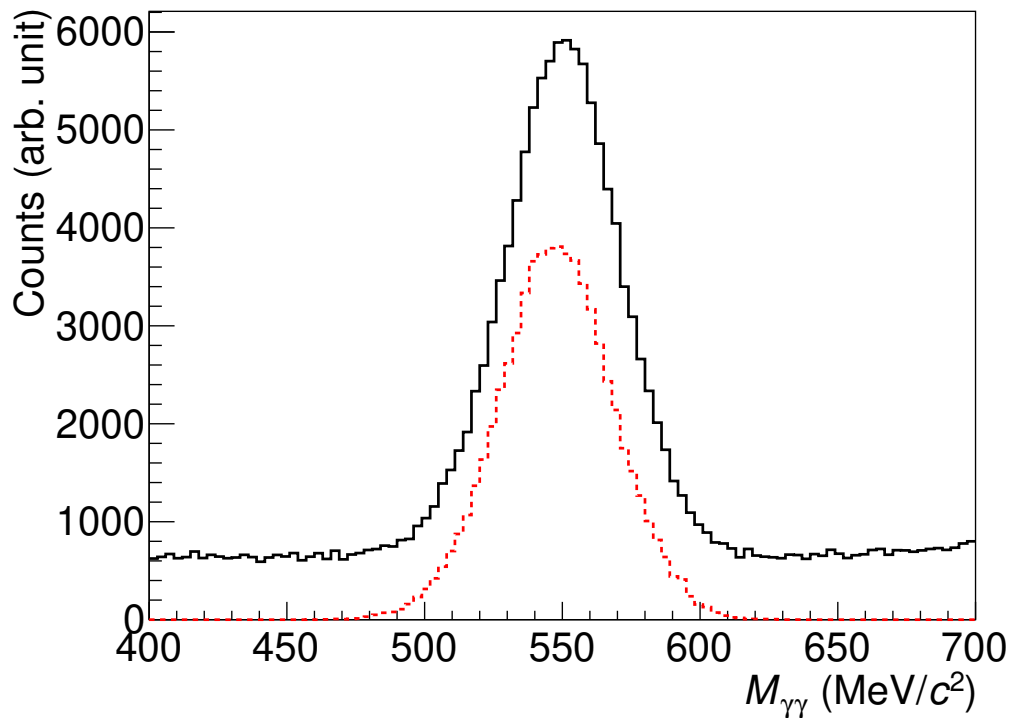


Figure 3.14: The invariant mass distribution for $\gamma\gamma$ pairs detected by using the BGOegg calorimeter. The black solid histogram shows the survived events after the missing mass cut. This cut means that the missing mass of a $\gamma\gamma$ pair is less than $1200 \text{ MeV}/c^2$. The red dashed histogram shows the survived events after applying the kinematic fit cut. The continuous background is successfully removed.

background processes were generated in MC simulations. Template spectra of the invariant and missing mass distributions for $\gamma\gamma$ pairs were prepared using loose event selection criteria. Characteristic shape for $\pi^0\pi^0$ photoproduction reaction appeared in side-band region of the invariant mass distribution. This background was main component of the continuous background, especially on the low mass side. The background from ω photoproduction reaction appeared as a bump structure in high mass side of the invariant mass distribution. The missing mass of background processes had higher tail than one of signal process. In particular, the background from $\eta\pi^0$ photoproduction reaction had the highest peak of missing mass. Finally, the invariant and missing mass distributions in the real data were simultaneously fitted using all template spectra with the yield of each reaction as a parameter at individual kinematic bins. The event samples were separated in five center-of-mass energies W , four polar angles $\cos\theta_{\text{c.m.}}^\eta$, and eight azimuthal angles ϕ .

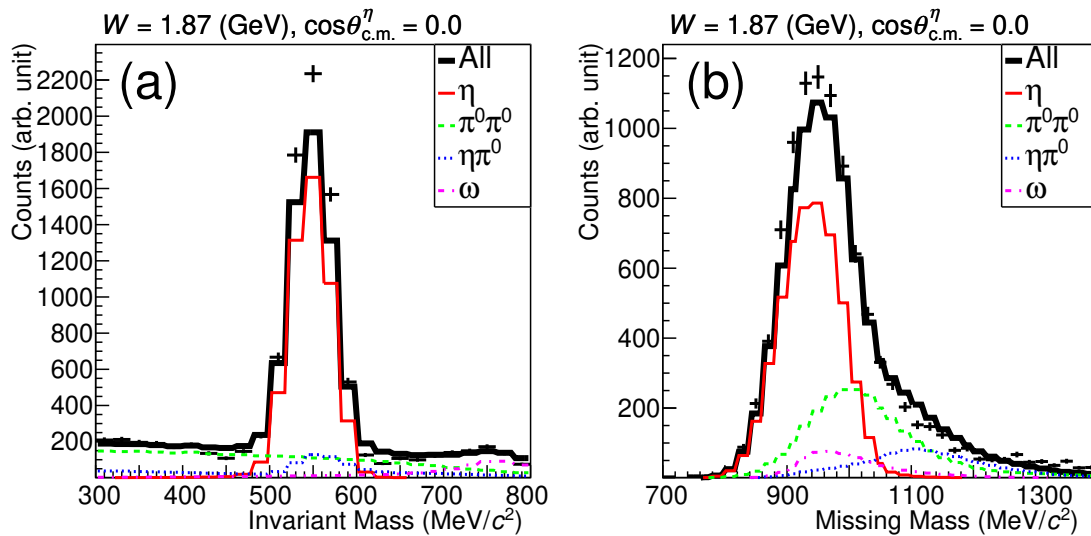


Figure 3.15: The template fitting at the kinematic bin of $W = 1.87$ GeV and $\cos\theta_{\text{c.m.}}^\eta = 0$. The left figure labeled (a) shows the invariant mass spectrum for $\gamma\gamma$ pairs in the real data and several MC samples. The black plots with statistical uncertainties represent the real data. The red solid, green dashed, blue dotted, and magenta dash-dotted histograms show the template mass spectra obtained from MC simulations of the η , $\pi^0\pi^0$, $\eta\pi^0$, and ω photoproduction processes, respectively. A sum of all the template spectra is represented by the solid thick black line. The right figure labeled (b) show the missing mass spectrum of a $\gamma\gamma$ pair in the real data and several MC samples. The correspondence between the color and style of the lines and each reaction is the same as in (a).

Figure 3.15 shows an example of the template fitting in a certain kinematic bin. Through this fitting process, the normalization factors for simulated background samples were established relative to the size of the real data. The contamination rate of each background after the kinematic fit cut was then evaluated by applying this cut to individual simulated background samples and taking into account the obtained normalization factors. Finally, the signal yields in individual kinematic bins were derived by subtracting the estimated background amounts.

In order to verify the validity of this template fitting approach, we assessed systematic variations in signal yields using two additional fitting methods. Firstly, we excluded the contribution of the ω meson from the fitting process to reduce the number of free parameters. To achieve this, we implemented a tight invariant mass cut to suppress any contamination from the ω meson. The yield difference compared to the original template fitting was less than 2% in all kinematic region. Secondly, we conducted a template fitting solely based on the invariant mass distribution to avoid a possible bias in signal extraction arising from simultaneous fitting to the missing mass distribution. In this method, we fixed the relative ratios of the three backgrounds based on the original template fitting, treating the total background amount as a free parameter. Notably, the yield difference from the original estimation was less than 6% across all kinematic regions.

In the current dataset, the number of events that passed the kinematic fit cut was 6.2×10^4 events. The background ratio varied across kinematic bins, ranging from 3.1% to 36.9%. Notably, this ratio exhibited an upward trend with increasing center-of-mass energy W . Following background subtraction, the estimated number of signal yields amounted to 5.5×10^4 events. We evaluated the background contribution originating from the target container by analyzing the data obtained with an "empty" target configuration. During this measurement, the target cell was filled with vaporized hydrogen gas. Few events remained after the kinematic fit cut, and we concluded this background contribution was negligible.

3.6 Geometrical acceptance

The geometric acceptance was evaluated by using a GEANT4-based MC simulation package developed for our experiment. Events for the process $\gamma p \rightarrow \eta p$ were generated with an isotropic angular distribution. The resulting cross sections from this acceptance determination were then integrated back into the MC simulation to incorporate realistic kinematic distributions for a subsequent round of acceptance calculation. This iterative process continued until the change in the differential cross section from the previous step became less than 1%. Typically, the acceptance rate is around 50% for backward η angles and decreases for forward angles. The acceptance coverage is $-1.0 < \cos \theta_{\text{c.m.}}^\eta < 0.6$.

Chapter 4

Results

In this chapter, we show the differential cross sections $d\sigma/d\Omega$ and the photon beam asymmetries Σ for the $\gamma p \rightarrow \eta p$ reaction in the energy range of $1.82 < W < 2.32$ GeV and the polar angle range of $-1.0 < \cos\theta_{\text{c.m.}}^\eta < 0.6$. First, Sec. 4.1 presents the formalism, systematic uncertainties, and energy distributions of the differential cross sections. In addition, the another results for $d\sigma/d\Omega$ obtained by an independent analysis of the same data set by using the RPC to provide reliability to the present results. Next, Sec. 4.2 presents the formalism, systematic uncertainties, and angular distributions of the photon beam asymmetries.

4.1 Differential cross section $d\sigma/d\Omega$

4.1.1 Formalism of $d\sigma/d\Omega$

The differential cross section $d\sigma/d\Omega$ is derived from the following equation:

$$\frac{d\sigma}{d\Omega} = \frac{Y_\eta}{N_\gamma \cdot T_\gamma \cdot F_{\text{trans}} \cdot \rho_N \cdot A \cdot \text{Br}_\eta \cdot \epsilon \cdot \Delta\Omega}. \quad (4.1)$$

Y_η represent the yield of η photoproduction within a specific kinematic bin, utilized for cross-section measurement. This value was derived by counting the number of events after the signal selection and background subtraction, as described in Sec. 3.5. N_γ is the number of beam photons after the dead time correction of the scaler as described in Sec. 3.1.3. T_γ is the calculated trans-

mission rate (0.772) as described in Sec. 3.1.4. F_{trans} is the energy-dependent correction factor for the beam transmission as described in Sec. 3.1.4. ρ_N is the number density of protons in the liquid hydrogen target. A is the geometrical acceptance in the BGOegg experiment for each kinematic bin as described in Sec. 3.6. Br_η is the branching fraction of the $\eta \rightarrow \gamma\gamma$ (0.3941). ϵ is the product of all other efficiency factors, and they are the tagger reconstruction efficiency, the fraction of true tagger tracks after removing shower contributions, and the proton detection efficiency of the IPS or the DC. Derailed descriptions of these efficiencies can be found in Sec. 3.1 and Sec. 3.3.

4.1.2 Systematic uncertainties of $d\sigma/d\Omega$

Systematic uncertainties affecting the measurement of differential cross sections are outlined in Table 4.1. Details regarding uncertainties originating from the template fitting method are provided in Sec. 3.5. Consistently, uncertainties related to the energy-dependent transmission and target length are the same as those reported in Ref. [51]. The impact of the transverse shift of the photon beam is also described in Ref. [51]. Although the magnitude of the shift aligns with that in Ref. [51], its effect on geometrical acceptance varies depending on the angular distribution of each reaction. Consequently, possible changes in geometrical acceptance factors were re-evaluated in individual kinematic bins via MC simulation. The estimated variations of the cross section values ranged from 0.01% to 8.8% depending on the kinematic bin. In this analysis, the 99% confidence level cut was applied to select signals after the kinematic fit. For estimating the uncertainty due to the cut point, the differential cross section was recalculated by adjusting the requirement on the χ^2 probability to exceed 5%, thereby selecting a flat region in the probability distribution. The resulting variations ranged from were 0.01% to 3.4%. Other sources of systematic uncertainties arise from the measurement of tagger reconstruction efficiency, shower contribution, and proton detection efficiency, detailed in Appendix E. Additionally, the uncertainty of the branching fraction of the $\eta \rightarrow \gamma\gamma$ decay was factored in based on the Particle Data Group value [15]. The total systematic uncertainties were evaluated to be in the range of 3.4% to 13%, obtained by summing the listed uncertainties in quadrature.

Table 4.1: Systematic uncertainties of the differential cross section measurement

Source of systematic uncertainty	Typical value
Template fitting	
Fitting excl. the ω contribution	0.1–2.4%
Fitting with invariant mass	0.8–5.9%
Energy dependent transmission	
Fit function dependence	0.2–1.0%
Normalization method	2.8%
Energy dependence	0.3–2.0%
Target length	1.3%
Beam position shift	0.01–8.8%
Kinematic-fit cut dependence	0.01–3.4%
Tagger reconstruction efficiency	0.57–0.92%
Shower contribution	1.4%
Proton detection efficiency	0.09% (IPS) 0.45% (DC)
Branching ratio ($\eta \rightarrow \gamma\gamma$)	0.50%

4.1.3 Energy distributions of $d\sigma/d\Omega$

Figures 4.1-4.4 show the differential cross sections as a function of total energy W . The binning of energy W and polar angle $\cos\theta_{c.m.}^\eta$ are 0.25 MeV and 0.1, respectively. The current results are depicted using red solid circles, denoting statistical uncertainties. Corresponding systematic uncertainties are represented by gray histograms. Detecting all the final-state particles, including a proton and two γ 's produced by the decay of an η meson, made the present analysis precise. Overall, the results exhibit a decreasing trend in the differential cross sections as energy increases in the region where $\cos\theta_{c.m.}^\eta > 0$. A distinctive bump structure emerges at higher energies within the region where $\cos\theta_{c.m.}^\eta < 0$, with its prominence increasing as the emission angles of η become more backward. Specifically, the bump is centered at $W = 1.97$ GeV for $\cos\theta_{c.m.}^\eta$ ranging from -0.1 to 0 , and slightly shifts to $W = 2.02$ GeV for $-0.7 < \cos\theta_{c.m.}^\eta < -0.6$. Notably, the peak position undergoes more rapid changes at the most backward angles, reaching $W = 2.25$ GeV within the range $-1 < \cos\theta_{c.m.}^\eta < -0.9$.

To ensure the reliability of the present results, an independent analysis of the same dataset was conducted, focusing on proton detection at the RPC. The RPC is capable of measuring the momentum of a forward proton via its TOF

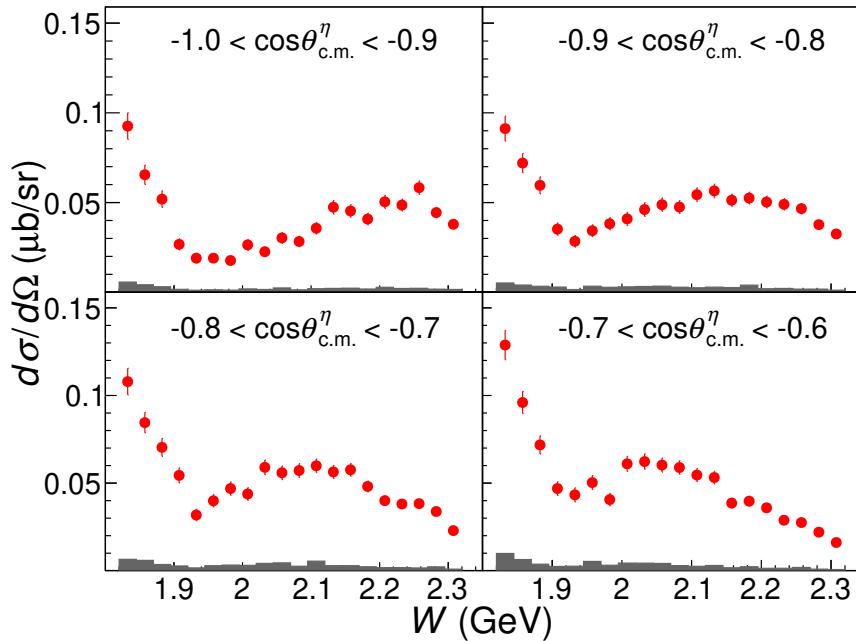


Figure 4.1: Differential cross sections $d\sigma/d\Omega$ as a function of W for the reaction $\gamma p \rightarrow \eta p$ at the polar angle $\cos\theta_{\text{c.m.}}^\eta$ from -1.0 to -0.6 . The current results are depicted using red solid circles, denoting statistical uncertainties. Corresponding systematic uncertainties are represented by gray histograms.

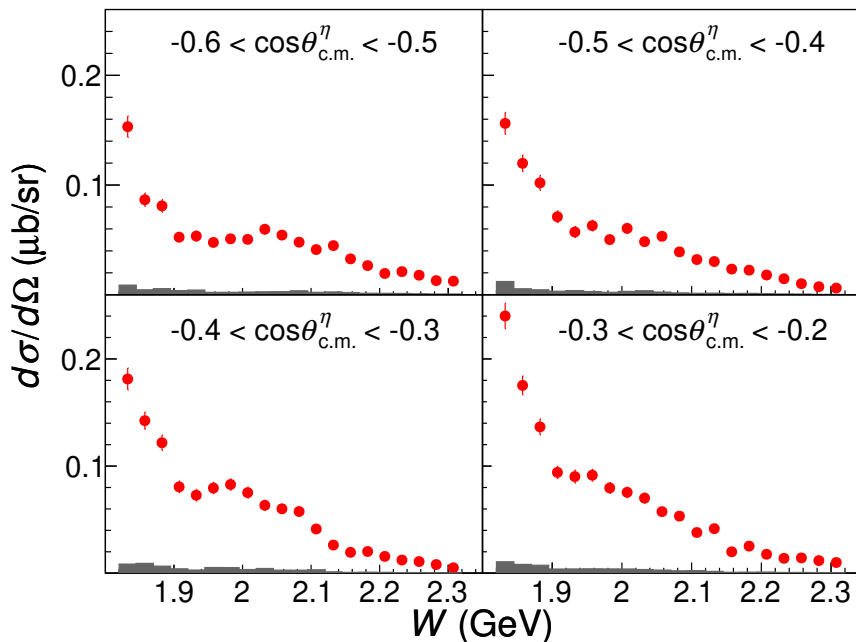


Figure 4.2: Differential cross sections $d\sigma/d\Omega$ as a function of W for the reaction $\gamma p \rightarrow \eta p$ at the polar angle $\cos\theta_{\text{c.m.}}^\eta$ from -0.6 to -0.2 . The current results are depicted using red solid circles, denoting statistical uncertainties. Corresponding systematic uncertainties are represented by gray histograms.

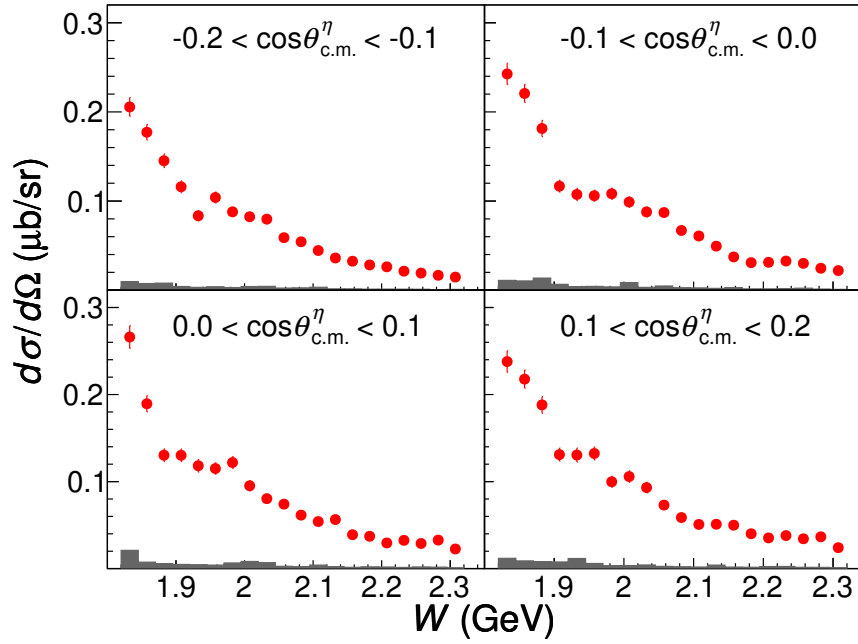


Figure 4.3: Differential cross sections $d\sigma/d\Omega$ as a function of W for the reaction $\gamma p \rightarrow \eta p$ at the polar angle $\cos \theta_{\text{c.m.}}^\eta$ from -0.2 to 0.2 . The current results are depicted using red solid circles, denoting statistical uncertainties. Corresponding systematic uncertainties are represented by gray histograms.

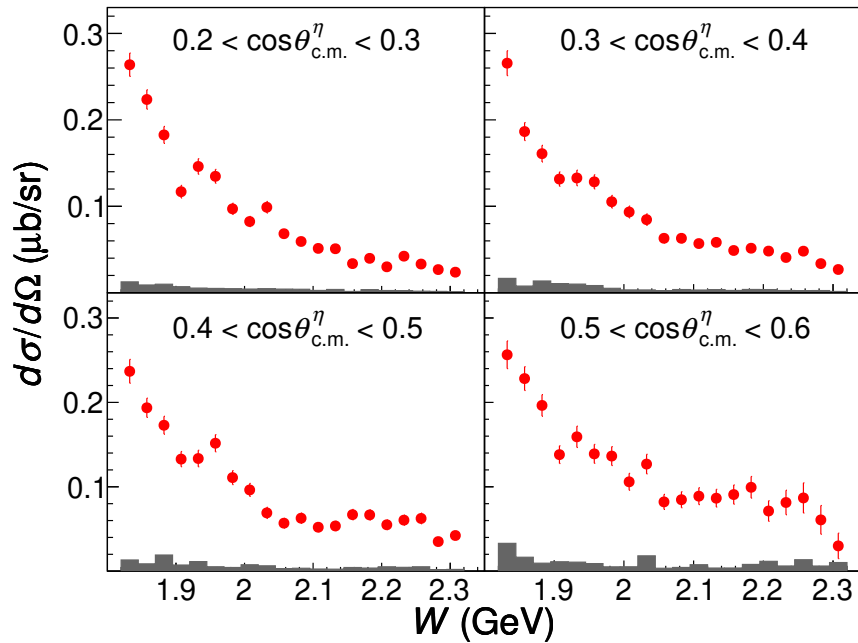


Figure 4.4: Differential cross sections $d\sigma/d\Omega$ as a function of W for the reaction $\gamma p \rightarrow \eta p$ at the polar angle $\cos \theta_{\text{c.m.}}^\eta$ from 0.2 to 0.6 . The current results are depicted using red solid circles, denoting statistical uncertainties. Corresponding systematic uncertainties are represented by gray histograms.

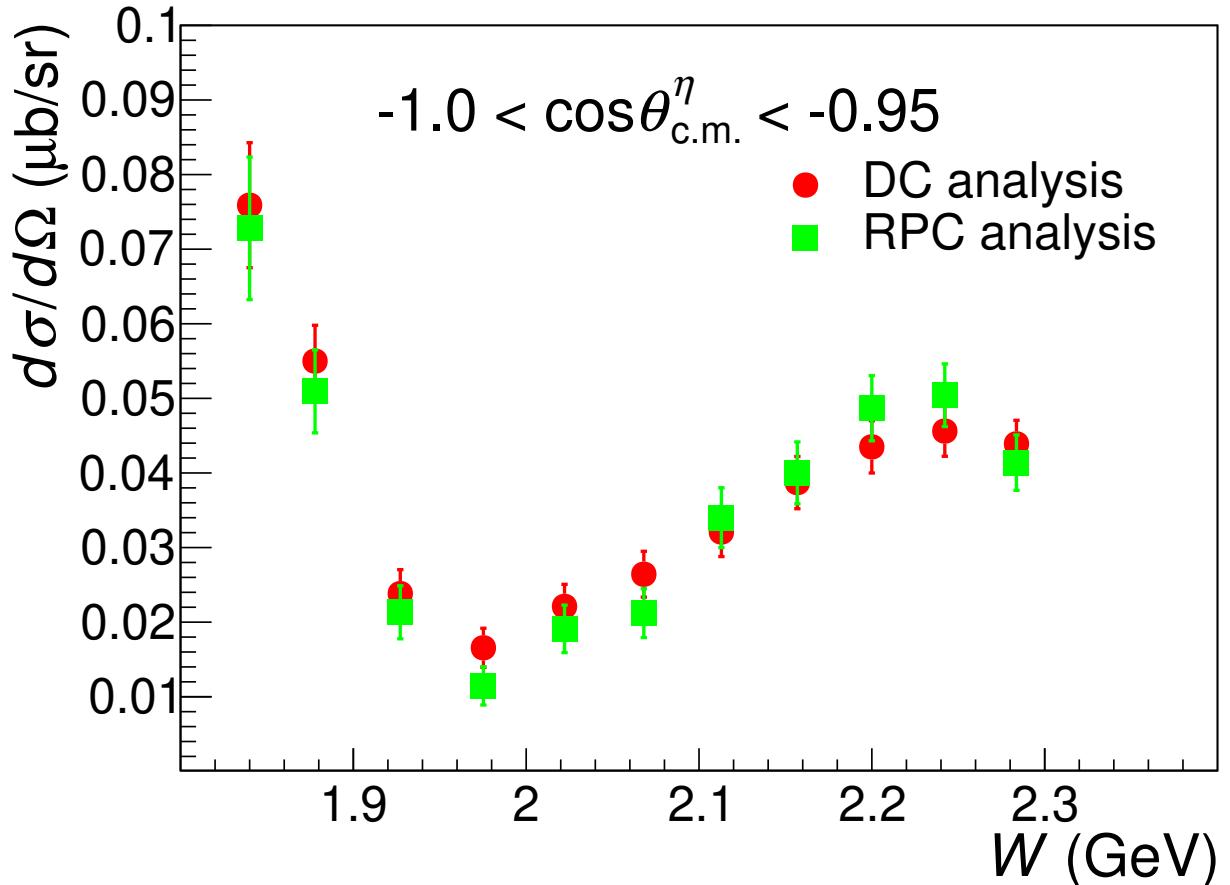


Figure 4.5: Comparison of the differential cross sections from two independent analyses in the extremely backward η angle regions $-1.0 < \cos \theta_{\text{c.m.}}^{\eta} < -0.95$. The red solid circles represents the results by using the DC. The green solid squares represents the results by using both the RPC and DC.

at extremely backward η angles ($-1.0 < \cos \theta_{\text{c.m.}}^\eta < -0.95$). This enables the RPC to provide complete kinematic information, allowing for four-momentum conservation in the kinematic fit without any unmeasured variables. Figure 4.5 illustrates a comparison of the differential cross sections obtained using the RPC (green squares) against those obtained using the DC (red circles), limited to the overlapping acceptance region. Notably, these two analyses exhibit excellent agreement both in terms of energy dependence and the overall magnitude of the differential cross sections.

4.1.4 Angular distributions of $d\sigma/d\Omega$

Figures 4.6-4.9 show the differential cross sections as a function of polar angle $\cos \theta_{\text{c.m.}}^\eta$. A backward rise of the differential cross section can be seen above $W = 2.1$ GeV and the peak position is shifted as energy increases. In the energy region where W is around 2.11 GeV, the peak is at the point where $\cos \theta_{\text{c.m.}}^\eta$ is -0.75 . And as the energy increases, the peak position moves toward $\cos \theta_{\text{c.m.}}^\eta = -1$, and in the region where W is above 2.25 GeV, the shape of the differential cross section is leftward.

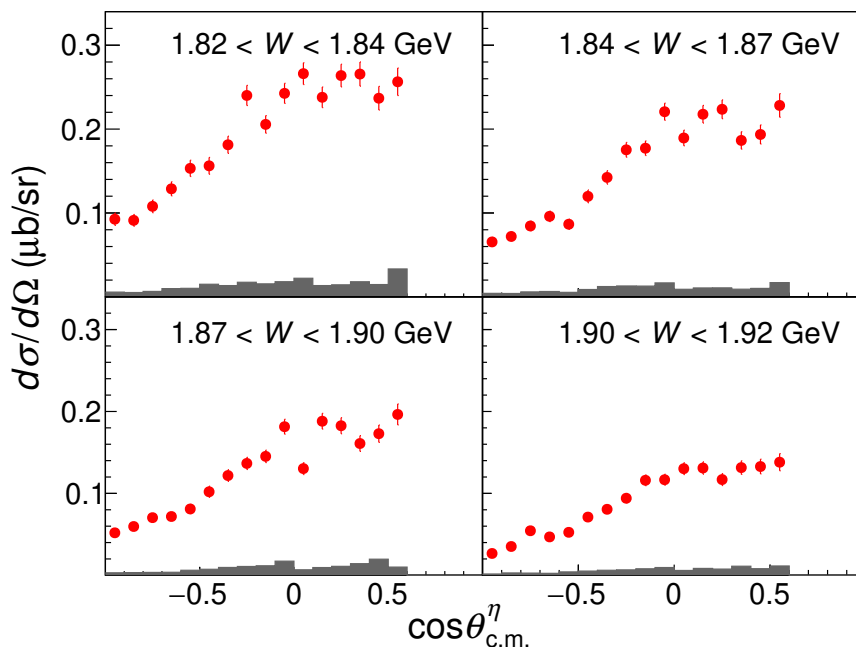


Figure 4.6: Differential cross sections $d\sigma/d\Omega$ as a function of $\cos \theta_{\text{c.m.}}^\eta$ for the reaction $\gamma p \rightarrow \eta p$ in the total energy W from 1.82 to 1.92. The current results are depicted using red solid circles, denoting statistical uncertainties. Corresponding systematic uncertainties are represented by gray histograms.

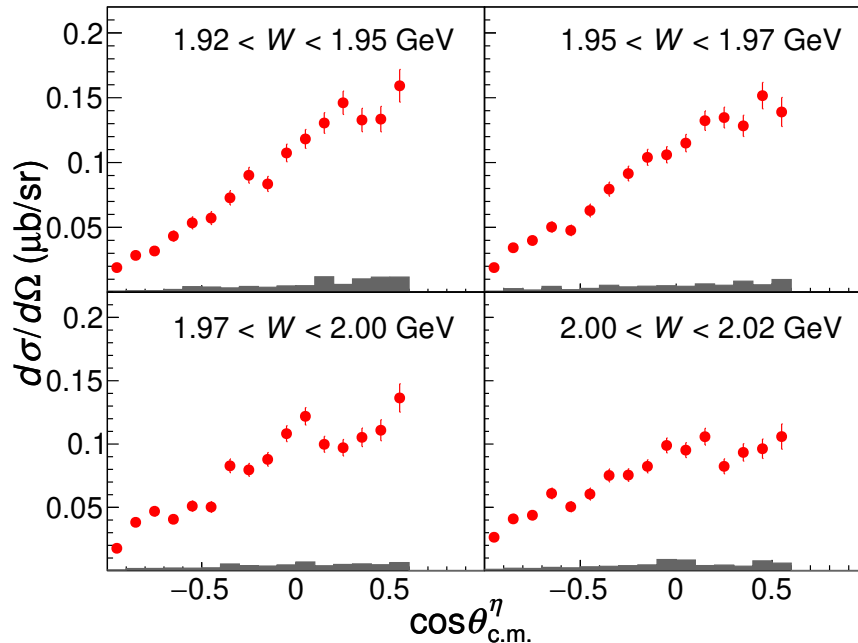


Figure 4.7: Differential cross sections $d\sigma/d\Omega$ as a function of $\cos\theta_{\text{c.m.}}^\eta$ for the reaction $\gamma p \rightarrow \eta p$ in the total energy W from 1.92 to 2.02. The current results are depicted using red solid circles, denoting statistical uncertainties. Corresponding systematic uncertainties are represented by gray histograms.

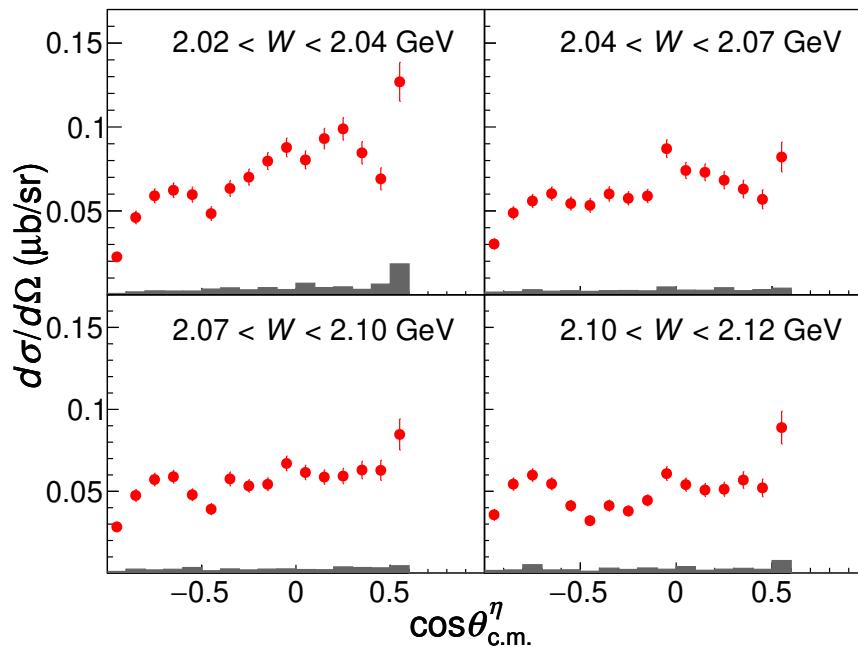


Figure 4.8: Differential cross sections $d\sigma/d\Omega$ as a function of $\cos\theta_{\text{c.m.}}^\eta$ for the reaction $\gamma p \rightarrow \eta p$ in the total energy W from 2.02 to 2.12. The current results are depicted using red solid circles, denoting statistical uncertainties. Corresponding systematic uncertainties are represented by gray histograms.

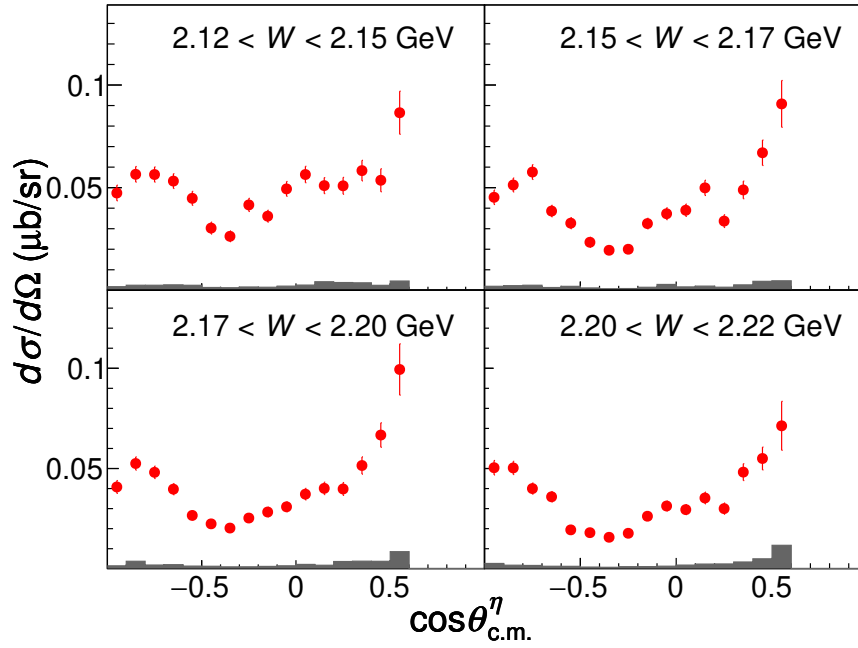


Figure 4.9: Differential cross sections $d\sigma/d\Omega$ as a function of $\cos\theta_{\text{c.m.}}^\eta$ for the reaction $\gamma p \rightarrow \eta p$ in the total energy W from 2.12 to 2.22. The current results are depicted using red solid circles, denoting statistical uncertainties. Corresponding systematic uncertainties are represented by gray histograms.

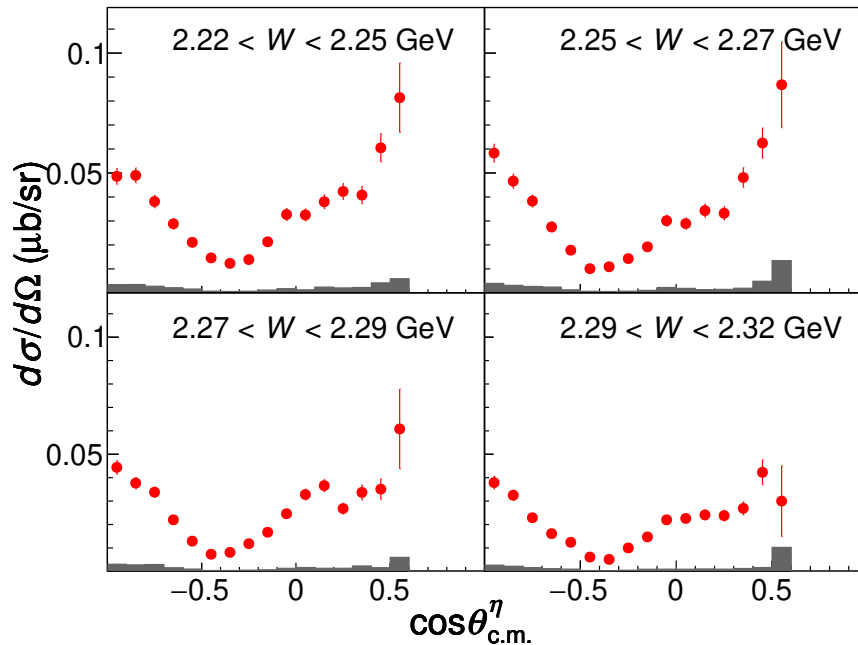


Figure 4.10: Differential cross sections $d\sigma/d\Omega$ as a function of $\cos\theta_{\text{c.m.}}^\eta$ for the reaction $\gamma p \rightarrow \eta p$ in the total energy W from 2.22 to 2.32. The current results are depicted using red solid circles, denoting statistical uncertainties. Corresponding systematic uncertainties are represented by gray histograms.

4.2 Photon beam asymmetry Σ

4.2.1 Formalism of Σ

The photon beam asymmetry Σ was determined by a fit to the azimuthal angular dependent yield:

$$f(\phi) = A(1 + B \cos(2\phi)) \quad (4.2)$$

The fitting parameter A in Eq. (4.2) is normalization factor. The fitting parameter B in Eq. (4.2) stands for the product of the degree of photon beam polarization P_γ and the photon beam asymmetry Σ . In order to reduce systematic uncertainties stemming from incomplete detector symmetry, horizontally and vertically polarized photon beams were employed alternately. The angles of polarization vectors for these beams were estimated to be -2.1 and 82.6 degrees from the horizontal plane in the laboratory frame, respectively. The degree of laser polarization typically reached 98%. P_γ ranged from 42% to 91%, with the highest polarization achieved at the Compton edge of the BCS photon beam.

4.2.2 Systematic uncertainties of Σ

Table 4.2: Systematic uncertainties of the photon beam asymmetry measurement

Source of systematic uncertainties	Typical value
Uncertainty of the template fitting method	0.001–0.03
Difference of two polarization data	0.003–0.05
Another binning of azimuthal angle	0.004–0.05
Ambiguity of polarization vector direction	0.001–0.008
Uncertainty of laser polarization degree	0.04% of $ \Sigma $

Systematic uncertainties affecting the measurement of photon beam asymmetries are itemized in Table 4.2. The values provided denote possible deviations in the Σ values, with estimated deviations distributed within the indicated range across kinematic bins. To reduce statistical uncertainty, neighboring kinematic bins were combined for certain uncertainty assessments. Primarily, uncertainties in yield estimations via the template fitting method were evaluated

by the same procedure for differential cross sections. Additionally, the difference between photon beam asymmetries in horizontal and vertical polarization data was examined to conservatively treat it as a possible systematic uncertainty. Furthermore, uncertainty stemming from different binning methods for azimuthal angles was estimated by shifting half a bin in the determination of bin ranges. Lastly, considerations were made for uncertainties in the polarization vector direction and laser polarization degree to estimate their impact on photon beam asymmetries. The total systematic uncertainties were determined to range from 0.008 to 0.09, obtained by summing the all of the above uncertainties in quadrature.

4.2.3 Angular distributions of Σ

Figures 4.11 and 4.12 show the photon beam asymmetries as a function of polar angle $\cos\theta_{\text{c.m.}}^\eta$. The binning of energy W and polar angle $\cos\theta_{\text{c.m.}}^\eta$ are 0.50 MeV and 0.2, respectively. The current results are depicted using red solid circles, denoting statistical uncertainties. Corresponding systematic uncertainties are represented by gray histograms. In this study, we have achieved precise Σ values in a broad angular range, marking the first instance of such precision at total energies surpassing 2.1 GeV. Notably, the photon beam asymmetries exhibit a dip structure around $\cos\theta_{\text{c.m.}}^\eta = -0.2$ for $W > 1.9$ GeV. This distinctive behavior has been proposed to be influenced by the helicity couplings associated with $N(1720)3/2^+$ and $N(1900)3/2^+$ [44]. Remarkably, this dip structure remains at higher energies, where the present analysis provides new data for the first time in the world.

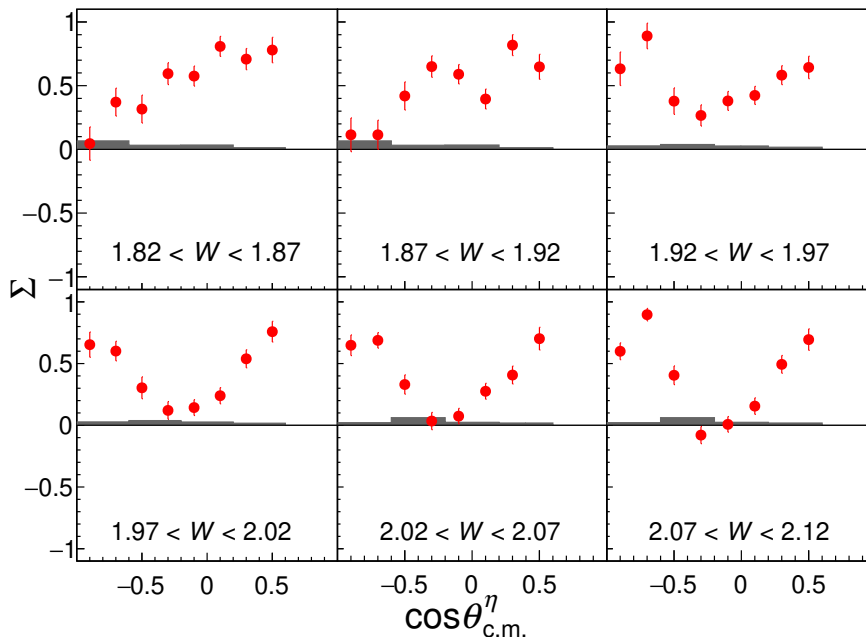


Figure 4.11: Photon beam asymmetries Σ as a function of $\cos\theta_{\text{c.m.}}^\eta$ for the reaction $\gamma p \rightarrow \eta p$ at the total energy W from 1.82 to 2.12 GeV. The current results are depicted using red solid circles, denoting statistical uncertainties. Corresponding systematic uncertainties are represented by gray histograms.

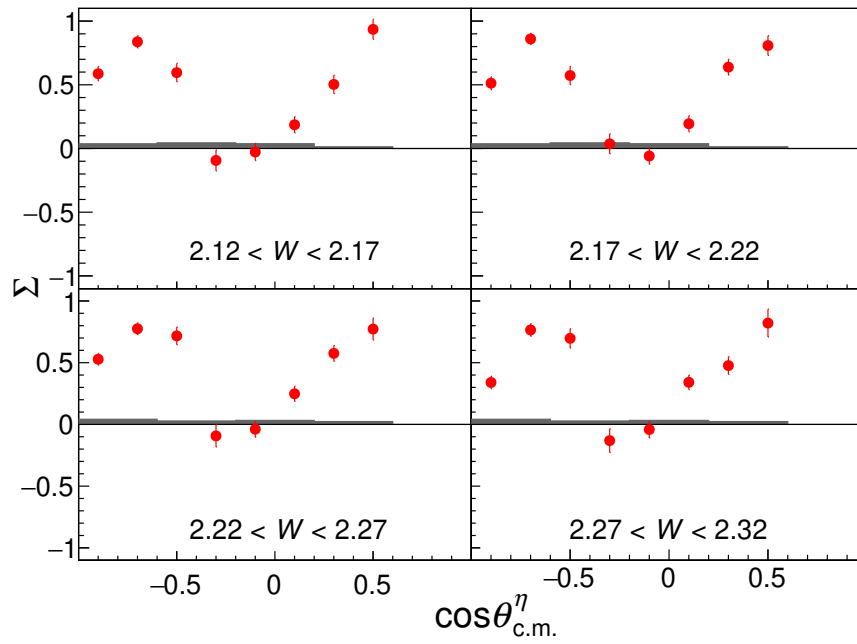


Figure 4.12: Photon beam asymmetries Σ as a function of $\cos \theta_{\text{c.m.}}^\eta$ for the reaction $\gamma p \rightarrow \eta p$ at the total energy W from 2.12 to 2.32 GeV. The current results are depicted using red solid circles, denoting statistical uncertainties. Corresponding systematic uncertainties are represented by gray histograms.

Chapter 5

Discussion

5.1 Differential cross section enhancement in $W = 2.0\text{--}2.3$ GeV

In this section, we discuss the cause of an enhancement of the differential cross section in $W = 2.0\text{--}2.3$ GeV at η backward angles. In Fig. 4.8-4.10, the polar angular dependent differential cross section above $W = 2.1$ GeV shows a backward rise at $\cos\theta_{\text{c.m.}}^\eta < -0.4$. Such behavior in the backward region is caused by a u -channel exchange or high-spin s -channel resonances.

5.1.1 u -channel contribution

According to Regge theory [47, 48], we can adopt a simple description of the smooth energy dependence for the u -channel cross section as $s^{2\alpha(u)-2}$, where s and $\alpha(u)$ represent the center-of-mass energy and a Regge trajectory function, respectively. Therefore the bump structures seen in a narrow range of $2.0 < W < 2.4$ GeV, as shown in Fig. 4.1, cannot be explained only by a u -channel contribution. The value of $(2\alpha(u) - 2)$ is expected to be negative within a small $|u|$ region as illustrated in Fig. 33 of Ref. [49]. In addition, the EtaMAID2018 calculation describes the non-resonant background as s - and u -channel Born terms and t -channel vector meson exchanges. This calculation suggests that the amplitude of the u -channel contribution is relatively small [22]. So the main contribution of the backward rise is expected to be s -channel contribution.

5.1.2 High-spin resonance contribution

The current data suggest that the sharp increase in backward region is likely associated with the decay of high-spin s -channel resonances. In photon-proton interactions, the helicity of the initial state is constrained to $|h| \leq 3/2$. Consequently, if an intermediate resonance has a high spin ($J \geq 5/2$), it can emit an η meson to the backward or forward polar angles in two-body decays, as understood by the discussion of helicity amplitudes with Wigner d -matrices [50]. The relationship between the spin parity of the intermediate state and the behavior of the differential cross section is illustrated in Fig. 1.9. In the forward region, the t -channel contribution becomes dominant as energy increases, while in the backward region, the t -channel makes little contribution. Therefore, the differential cross sections at backward η angles are particularly sensitive to the high-spin s -channel resonances. As mentioned in Sec. 4.1.4, the peak position seems to shift with energy in angular dependent differential cross sections. It suggests that there are contributions from different resonance states at different energies. Considering the angular distribution for a single EM multipole amplitude, the contribution from E_{3-} , M_{2+} , E_{4-} , and M_{3+} may appear in $2.11 < W < 2.25$ GeV. In higher energy regions, the contribution from E_{2+} , and M_{2-} may be dominant.

5.1.3 Comparison with other meson photoproduction results

Figure 5.1 shows the energy-dependent differential cross sections for the η , π^0 and ω photoproduction processes at backward regions measured by the LEPS2/BGOegg Collaboration. The red circles, green squares, blue triangles, and magenta inverted triangles indicate the results where the angles $\cos \theta_{\text{c.m.}}$ are -0.95 , -0.85 , -0.75 , and -0.65 , respectively. The differential cross sections of π^0 and ω photoproduction were published in Refs. [51] and [52], respectively. All of these photoproduction reaction studies were obtained on the same data set. The differential cross sections of the π^0 photoproduction in backward regions are slowly decreasing with increasing energy. Only when the polar angle $\cos \theta_{\text{c.m.}}^{\pi^0}$ is -0.95 , a slight enhancement of the differential cross sections is seen from $W = 2.1$ GeV, but no clear bump structures exist. The differential cross

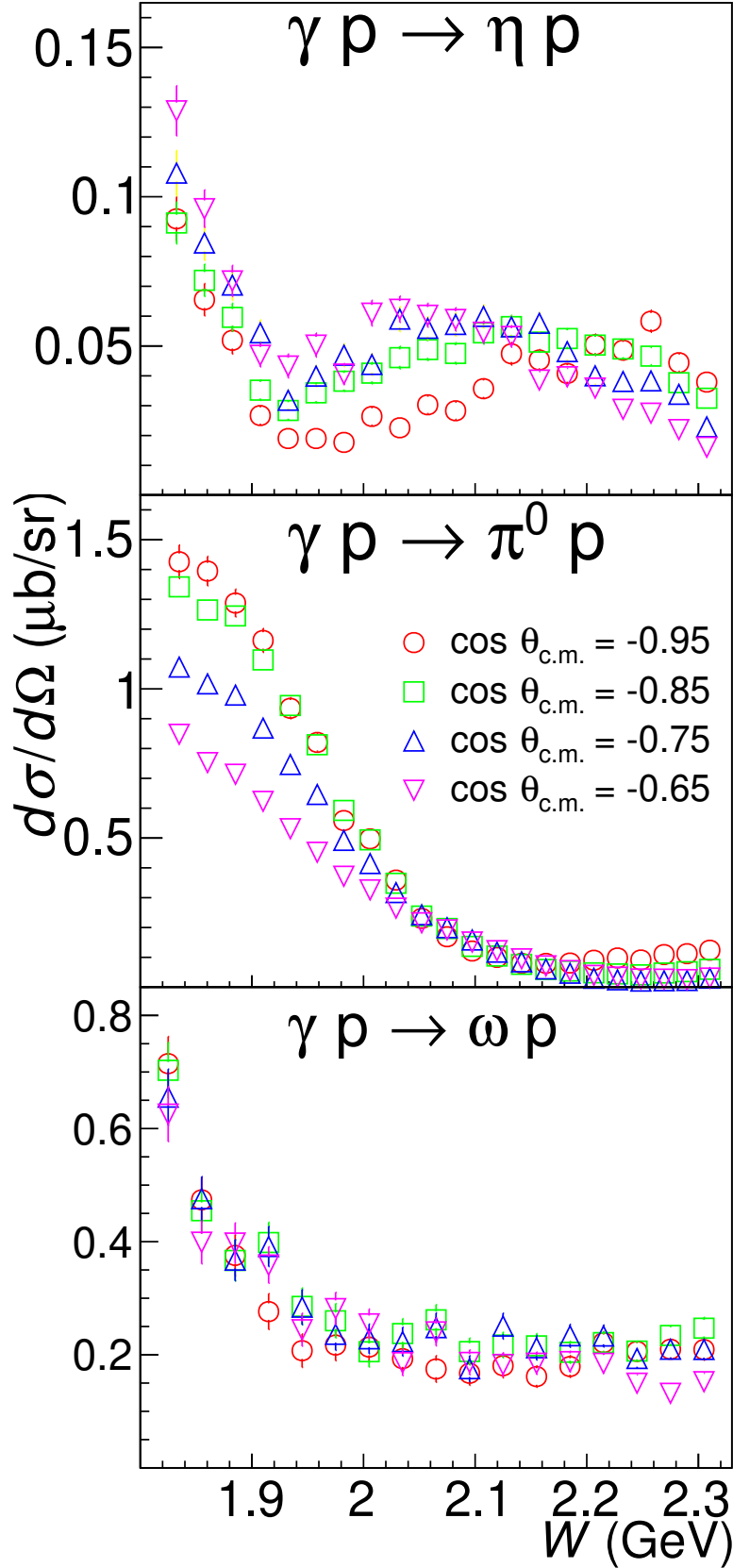


Figure 5.1: The differential cross sections of the η , π^0 and ω photoproduction processes as a function of the center-of-mass energy W [51, 52]. The red circles, green squares, blue triangles, and magenta inverted triangles indicate the results where the angles $\cos \theta_{\text{c.m.}}$ are -0.95 , -0.85 , -0.75 , and -0.65 , respectively.

sections of the ω photoproduction in backward regions also show declining behaviors. No structure of note is seen. In contrast, only the differential cross sections of the η photoproduction shows a clear bump structure at the center-of-mass energies above 2.0 GeV. The biggest difference between the η mesons and the π^0 and ω mesons is whether or not they contain $s\bar{s}$ quark pair as a component. Therefore, the observed bump structure in the differential cross sections of η photoproduction is likely associated with the nucleon resonances that have a large $s\bar{s}$ component and strongly couple to the ηN channel.

5.2 Comparison with other experimental results and PWA solutions

5.2.1 Differential cross section

The differential cross sections for the $\gamma p \rightarrow \eta p$ reaction were measured with the steps of 25 MeV in W and $0.1 \cos \theta_{\text{c.m.}}^\eta$, respectively. Figure 5.2 shows the energy-dependent differential cross sections for individual $\cos \theta_{\text{c.m.}}^\eta$ bins in present and previous experiments. The red solid circles and gray histograms indicate the our results and systematic uncertainties as described in Sec. 4.1.3. Also shown are the other experimental results. The black inverted triangles, green triangles, and blue squares represent the result of LEPS [20], CBELSA/TAPS [36], CLAS [35] experiments, respectively. The bin widths for the photon beam energy E_γ in LEPS and CBELSA/TAPS experiments were 100 and 50 MeV in all energy regions, respectively. In the CLAS experiment, the results are divided by center-of-mass energy W , and the step is 10 MeV for $1.68 < W < 2.10$ GeV and 5 MeV for $2.10 < W < 2.36$ GeV. All of those results were consistently binned with 0.1 steps in $\cos \theta_{\text{c.m.}}^\eta$.

The BGOegg experiment detected all the final-state particles in wide angular measurement. The coverage of polar angles is $-1.0 < \cos \theta_{\text{c.m.}}^\eta < 0.6$. In the LEPS experiment, the momentum of the forward emitted protons is precisely measured with a forward spectrometer, and events in which an η meson was produced were identified by a missing mass technique. This acceptance is limited to be $\cos \theta_{\text{c.m.}}^\eta < -0.6$. The CLAS experiments detected charged particles, including a proton and a $\pi^+\pi^-$ pair from an η meson decay $\eta \rightarrow \pi^+\pi^-\pi^0$. The

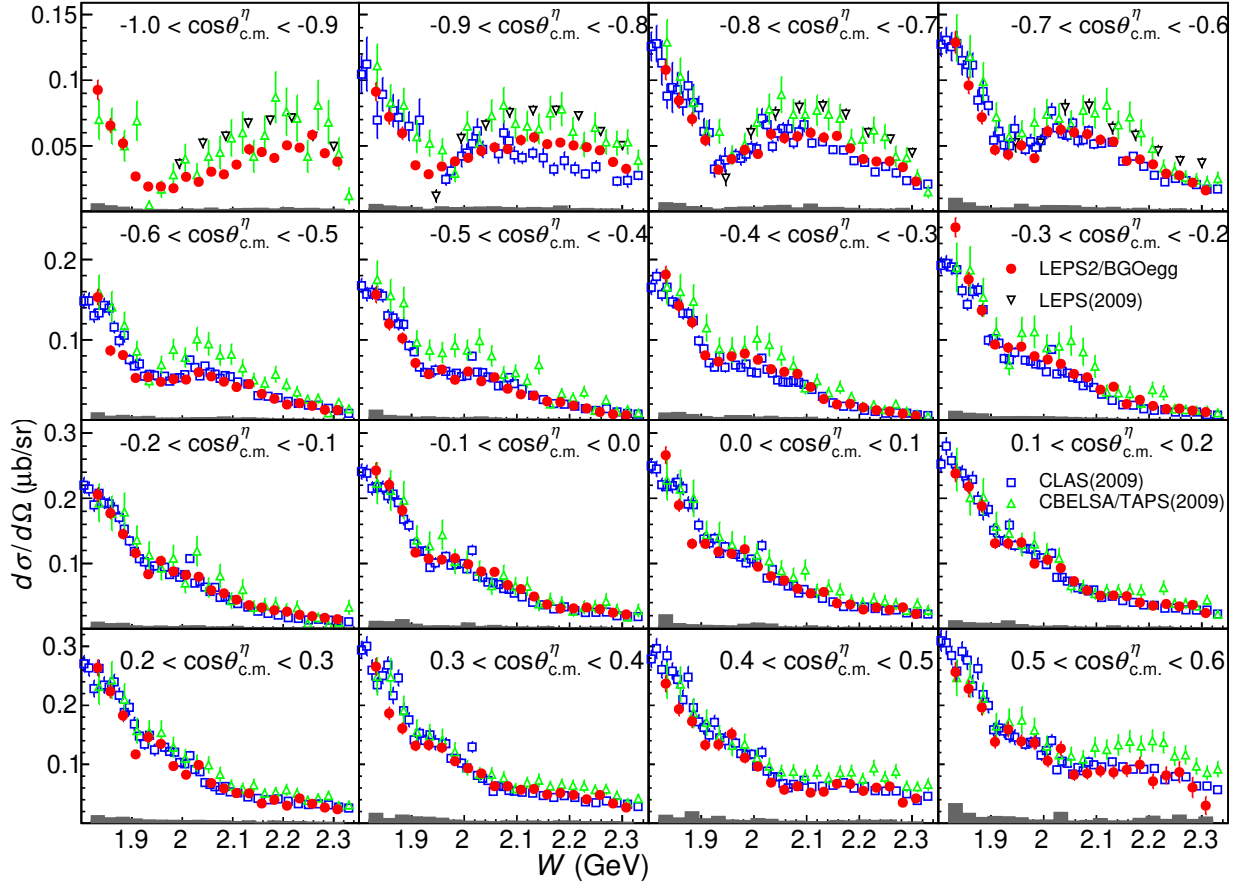


Figure 5.2: Differential cross sections $d\sigma/d\Omega$ as a function of center-of-mass energy W for the $\gamma p \rightarrow \eta p$ reaction. The individual panels correspond to different bins of the η emission angle in the center-of-mass system. The current results are depicted using red solid circles, denoting statistical uncertainties. Corresponding systematic uncertainties are represented by gray histograms. The results from CBELSA/TAPS [36], CLAS [35], and LEPS [20] Collaborations represent as green triangles, blue squares, and black inverted triangles, respectively.

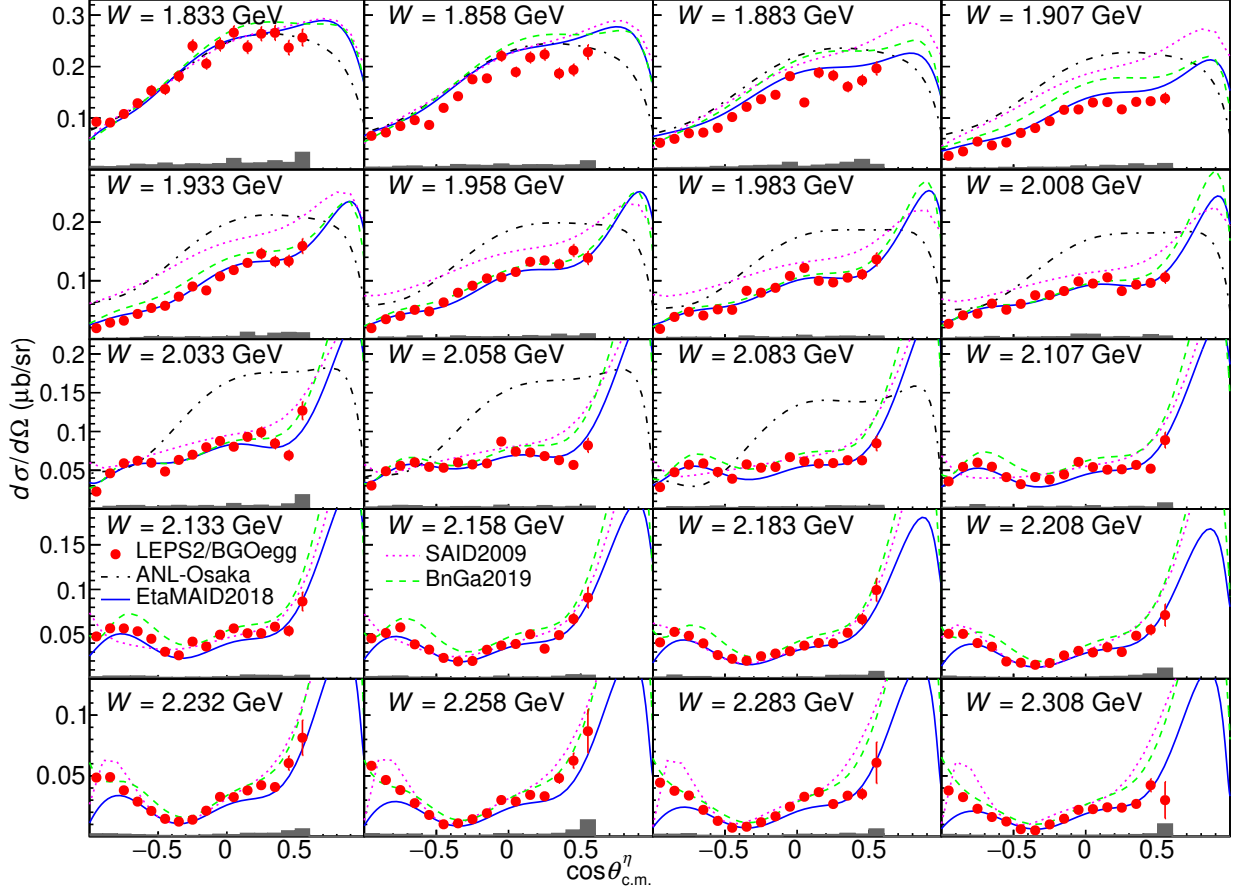


Figure 5.3: Differential cross sections $d\sigma/d\Omega$ as a function of $\cos\theta_{c.m.}^\eta$ for the reaction $\gamma p \rightarrow \eta p$. The current results are depicted using red solid circles, denoting statistical uncertainties. Corresponding systematic uncertainties are represented by gray histograms. The PWA model calculations from EtaMAID2018 [22], SAID2009 [38], Bonn-Gatchina2019 [23], and ANL-Osaka2016 [40] shows as blue solid, magenta dotted, green dashed, and black dash-dotted curves, respectively.

π^0 meson was treated as a missing particle in the kinematic fit. The experimental results of the CLAS Collaborations were most statistically accurate in a wide angular range $-0.855 < \cos \theta_{\text{c.m.}}^\eta < 0.8$. Unfortunately, there is no sensitivity in the most backward angle region which we were most interested in. The CBELSA/TAPS experiment detected all the final-state particles by using large acceptance calorimeters as we do. In addition, they identified η mesons in the two decay modes: $\eta \rightarrow \gamma\gamma$ and $\eta \rightarrow 3\pi^0 \rightarrow 6\gamma$. Their detectors covered a whole angular region including the missing backward η angles of the CLAS experiment. However, the statistical uncertainties were greater than one of other experiments.

The present results are in good agreement with the result in CLAS and CBELSA/TAPS experiments in any polar angular regions in the energy region $W < 2$ GeV. In $W > 2$ GeV, the BGOegg results are consistent with the CLAS data except for $\cos \theta_{\text{c.m.}}^\eta < -0.8$. The peak position of the differential cross section in $-0.9 < \cos \theta_{\text{c.m.}}^\eta < -0.8$ region in CLAS experiment are lower than one in previous experiment. The CBELSA/TAPS data provide larger cross sections compared to our results. Nevertheless, the statistical uncertainties for CBELSA/TAPS results are large, so it is consistent within the margin of three standard deviations. The behavior of the bump structure in CBELSA/TAPS is also similar to our behavior. The differential cross section obtained by LEPS experiment is significantly larger than the BGOegg results. The peak positions of two data are also similar in $-0.9 < \cos \theta_{\text{c.m.}}^\eta < -0.6$ regions, but different where $\cos \theta_{\text{c.m.}}^\eta$ is less than -0.9 .

Figure 5.3 shows the polar angular dependent differential cross sections and the several PWA model calculations. The red points and gray histograms represent the BGOegg results and associated systematic uncertainties. The blue solid, magenta dotted, green dashed, and black dotted-dashed lines indicate the PWA calculations by by EtaMAID2018 [22, 37], SAID2009 [38], Bonn-Gatchina2019 [23, 39], and ANL-Osaka2016 [40, 41], respectively. The EtaMAID2018 calculations reproduce the present data at total energies below 2.2 GeV. But the backward rise in above $W = 2.2$ GeV is not seen. The SAID2009 calculations disagree with our results in many respects. They overestimate differential cross sections in center-of-mass energy region $1.9 < W < 2.1$ GeV. Also, the peaking structure obtained by the SAID2009 calculation in

$\cos \theta_{\text{c.m.}}^\eta < -0.6$ and $W > 2.2$ GeV is not observed in the present data. The ANL-Osaka2016 does not reproduce our results overall, nor is it applicable to the center-of-mass energy region $W > 2.1$ GeV. The Bonn-Gatchina2019 calculations are in agreement with our results compared to other PWA calculations. Especially, the backward rise of the differential cross section in above $W = 2$ GeV is produced. On the other hand, some overestimations compared to the experimental results exist, and it cannot be said that they perfectly reproduce our results. In higher energy regions, the EtaMAID2018 utilizes only CLAS data and the Bonn-Gatchina2019 fits only CBELSA/TAPS data to create parameters for PWA calculations, and these differences are thought to reflect differences between experiments. A new PWA calculations including our data is needed for detailed analysis. In the next subsection, the effectiveness of the Bonn-Gatchina2019 model can be assessed through the newly measured photon beam asymmetries in the current analysis.

5.2.2 Photon beam asymmetry

In Fig. 5.4, our results and several other experimental results obtained by the GRAAL [42], CLAS [44], and CBELSA/TAPS [45] Collaborations are also plotted. Since each of these experimental results is divided by different energy bin widths, the results in each experiment are overlaid in the specific energy bin, where the center of energy bin is closest to the one in the BGOegg experiment. The black triangles indicate the GRAAL results which have 15 energy bins as photon beam energy E_γ in range of 0.7–1.5 GeV. They measured highly precise results below $W = 1.9$ GeV due to the high degrees of beam polarization at the Compton edge of the BCS photon. The green inverted triangles represent the CBELSA/TAPS results obtained for the photon beam energy bins of each 60 MeV in the range of $E_\gamma = 1.13$ –1.79 GeV. The energy bin width is 60 MeV as the photon beam energy. They observed drastic change in the angular distribution of photon beam asymmetry above $W = 1.9$ GeV. The photon beam asymmetries exhibit a dip structure around $\cos \theta_{\text{c.m.}}^\eta = -0.2$. The blue squares indicate the CLAS results divided into photon beam energy bins E_γ , and the step is 27 MeV for $1.071 < E_\gamma < 1.689$ GeV and 40 MeV for $1.689 < E_\gamma < 1.876$ GeV. The same dip structure can be seen. Our precise results are in agreement with the any other experimental results below $W = 2.1$ GeV.

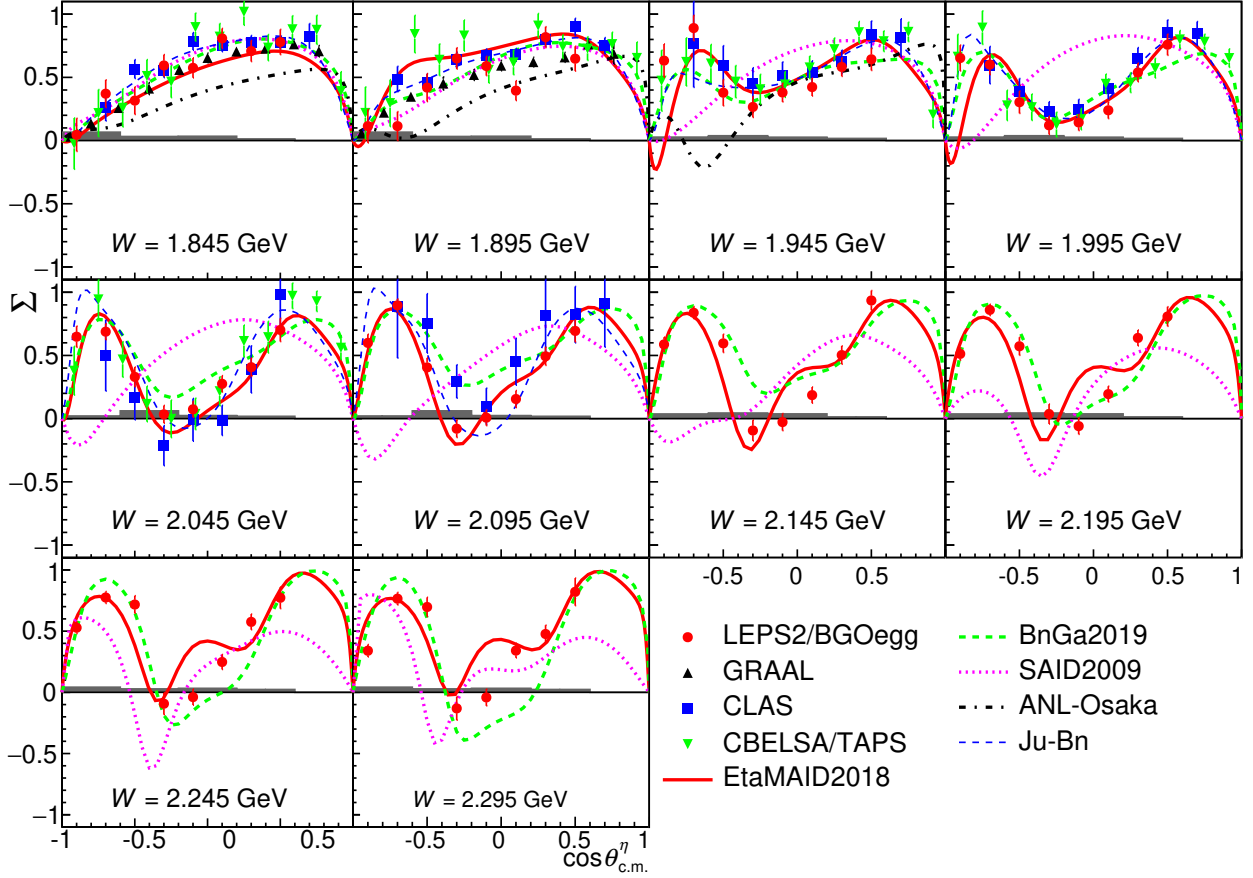


Figure 5.4: Photon beam asymmetries Σ as a function of $\cos \theta_{c.m.}^\eta$ for the η meson photoproduction. The current results are depicted using red solid circles, denoting statistical uncertainties. Corresponding systematic uncertainties are represented by gray histograms. The experimental result obtained by GRAAL [42], CLAS [44], and CBELSA/TAPS [45] Collaborations indicate the black triangles, blue squares, and green inverted triangles, respectively. The PWA predictions calculated by the EtaMAID2018 [22], Bonn-Gatchina2019 [23], SAID2009 [38], ANL-Osaka2016 [40], and Jülich-Bonn [46] models represent the blue solid, green dashed, magenta dotted, black dash-dotted, and blue long-dashed curves, respectively.

The PWA predictions calculated by the EtaMAID2018 [22], Bonn-Gatchina2019 [23], SAID2009 [38], ANL-Osaka2016 [40], and Jülich-Bonn [46] models represent the blue solid, green dashed, magenta dotted, black dash-dotted, and blue long-dashed curves, respectively. The EtaMAID2018 model calculations reproduce the present results below $W = 2.0$ GeV. The results of Bonn-Gatchina2019, and Jülich-Bonn models replicate our results as well. What these models have in common is that they fit the recent results for photon beam asymmetries from CLAS [44] and CBELSA/TAPS [45] experiments. The SAID2009 curve does not reproduce the dip structure above $W = 1.95$ GeV. The ANL-Osaka is only applicable in the region of $W < 1.95$ GeV because it does not include heavy-meson contributions such as an ω meson in the coupled-channel calculation. In the region above 2.0 GeV, no PWA results reproduce the BGOegg results.

The position of the bump structure shifts from $W = 2.02$ GeV at $\cos \theta_{\text{c.m.}}^\eta = -0.65$ to $W = 2.25$ GeV at $\cos \theta_{\text{c.m.}}^\eta = -0.95$, as mentioned in Sec. 5.1. This may be caused by the presence of multiple nucleon resonances. In the mass range of 2.1–2.3 GeV, several resonances with three or four stars are currently known based on the πN -decay channel (e.g. $N(2100)1/2^+$, $N(2120)3/2^-$, $N(2190)7/2^-$, $N(2220)9/2^+$, $N(2250)9/2^-$) [15]. However, the information about the ηN -decay of nucleon resonances is limited. The new BGOegg data of differential cross sections as well as photon beam asymmetries has high statistics at backward angles and provides additional constraints for the resonance search, particularly related to the bump structure.

5.3 Comparison with the existing PWA results

The differential cross sections and photon beam asymmetries measured in the present analysis are in fair agreement with the existing PWA results at lower energies. In contrast, the PWA results at higher energies show clear differences from the present data, as described in Sec. 5.2. The discrepancies in the photon beam asymmetries are particularly large. In addition, the PWA results are inconsistent with each other at the higher energies.

These discrepancies are clearly seen in Fig. 5.6, which compares the present data with existing PWA results calculated by the EtaMAID2018 ((a) and (b))

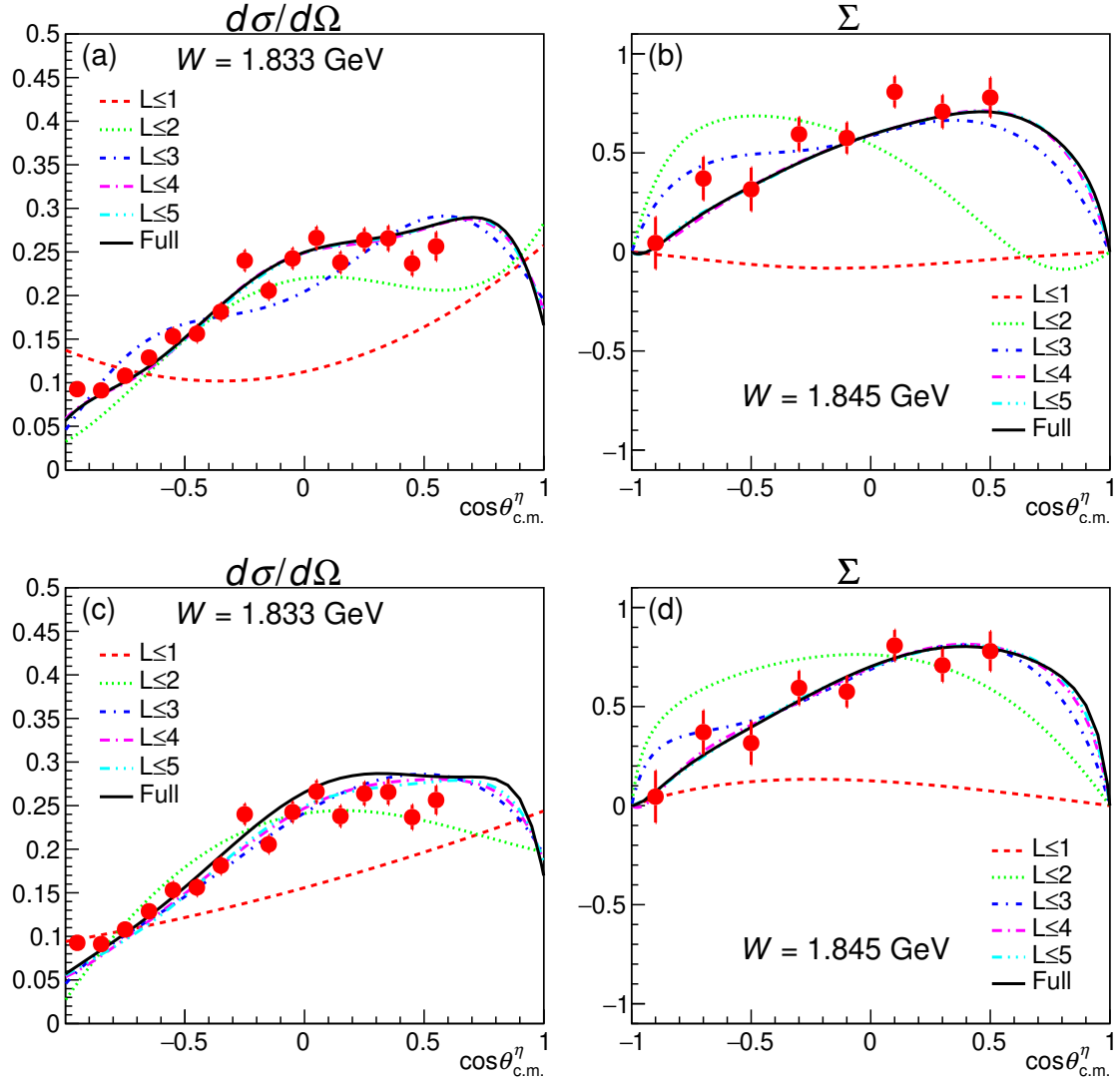


Figure 5.5: The existing PWA results calculated by EtaMAID2018 ((a) and (b)) and Bonn-Gatchina2019 ((c) and (d)) with the orbital angular momenta L up to 1 (red dashed lines), 2 (green dotted lines), 3 (blue dotted-dashed lines), 4 (magenta long dashed-dotted lines), and 5 (cyan dotted lines). The full PWA calculation with all the orbital angular momenta is shown by black solid lines. The BGOegg results are plotted as red circles.

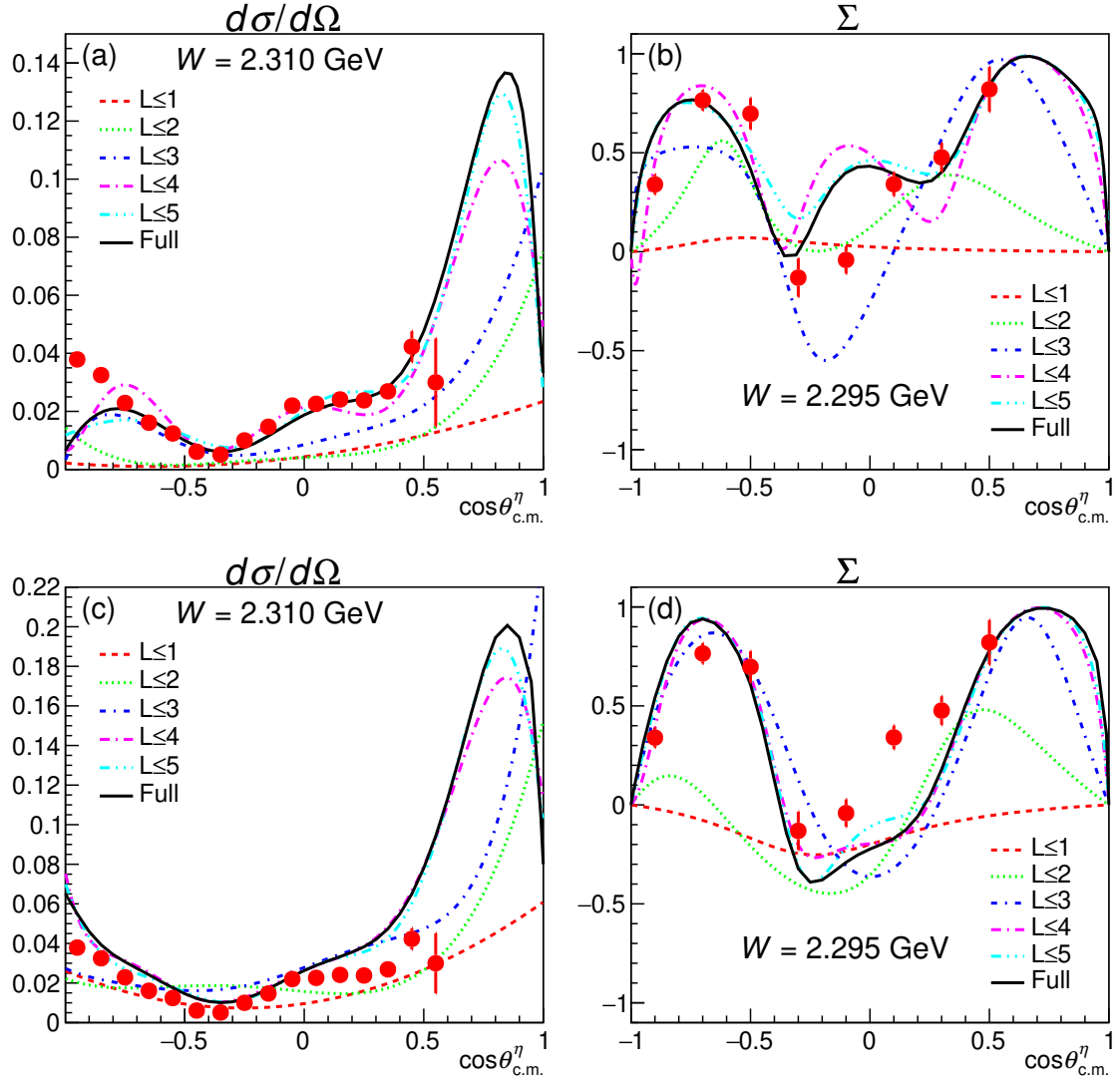


Figure 5.6: The existing PWA results calculated by EtaMAID2018 ((a) and (b)) and Bonn-Gatchina2019 ((c) and (d)) with the orbital angular momenta L up to 1 (red dashed lines), 2 (green dotted lines), 3 (blue dotted-dashed lines), 4 (magenta long dashed-dotted lines), and 5 (cyan dotted lines). The full PWA calculation with all the orbital angular momenta is shown by black solid lines. The BGOegg results are plotted as red circles.

and Bonn-Gatchina2019 ((c) and (d)) models at the highest energy bin near $W = 2.3$ GeV. Here, differential cross sections and photon beam asymmetries are plotted in the left ((a) and (c)) and right ((b) and (d)) sides, respectively. For drawing the PWA curves of EtaMAID2018 and Bonn-Gatchina2019, the electromagnetic amplitudes, containing the information about the partial waves, were obtained from Refs. [37] and [39], respectively. The multipole amplitudes were combined with the Legendre polynomials to construct the CGLN amplitudes [12], which are conventionally used for the pseudoscalar-meson photoproduction. In each panel, contributions from the partial waves up to the indicated orbital angular momenta (L) are also shown.

In Fig. 5.6 the EtaMAID2018 full calculation reproduces the measured differential cross sections except for the most backward η angles, where the experimentally observed backward rise does not exist in the calculated result. This calculation shows a small bump structure of photon beam asymmetry at $\cos \theta_{\text{c.m.}}^\eta \sim 0$, while it is not seen in the experimental data. On the other hand, the Bonn-Gatchina2019 results reproduce the backward shape of differential cross sections but its strength is overestimated compared to the present results. The calculated photon beam asymmetry has no small bump structures like the EtaMAID2018 calculation but it is underestimated compared with the experimental data around $\cos \theta_{\text{c.m.}}^\eta \sim 0$. Neither of these PWA models can reproduce the differential cross sections and the photon beam asymmetries simultaneously.

The different behaviors of backward cross sections in the two PWA results arise from the ambiguity of multipole contributions even at $L \leq 3$, as seen in Fig. 5.6. The different determinations of multipoles in the lower L region also cause a large difference between the calculated photon beam asymmetries especially at middle angles. It is clear that the current understanding of resonance and Born-term contributions is not enough even for lower L 's at high energies. In addition, higher L contributions are important to reproduce the experimental data accurately.

5.4 Jülich-Bonn calculation comparison

Recently the Jülich-Bonn model calculation was updated by a fit to the differential cross sections and photon beam asymmetries in the η photoproduction

measured by the CLAS experiment [44]. In this measurement, the photon beam asymmetries were obtained at $1.70 < W < 2.10$ GeV and $-0.8 < \cos \theta_{\text{c.m.}}^\eta < 0.8$. Before the fit was made, the $N(1900)3/2^+$ was found to be important in the analyses of $K\Lambda$ and $K\Sigma$ photoproduction by the Bonn-Gatchina group [53]. In order to confirm this resonance contribution, the CLAS Collaboration fitted two sets of possible solutions with and without a contribution from the $N(1900)3/2^+$ resonance by using the Jülich-Bonn model. The CLAS data indicated the weakness of the $N(1900)3/2^+$ contribution in the η photoproduction, but was not able to clarify its strength because the difference between the two fits to the photon beam asymmetries should appear at extremely backward η angles, which were out of the CLAS acceptance. In contrast, the present results of photon beam asymmetries cover the most backward angles, while they are consistent with the CLAS results in the overlapping angular region. A refit of the Jülich-Bonn model to present data must provide more accurate information about the strength of the $N(1900)$ contribution.

5.5 Future work

In order to extract detailed information of resonances from the experimental results, it is necessary to fit the present data with PWA models. A detailed PWA including our new experimental results is currently underway in cooperation with the Bonn-Gatchina group [23]. The BGOegg experiment also has data on liquid hydrogen targets that have not yet been analyzed, which together are expected to increase the statistics by a factor of 2.5. We plan to use the results of the PWA analysis to identify sensitive regions to the resonance contribution and refine the bin widths to investigate the behavior in more detail.

Chapter 6

Summary

The constituent quark models describe the ground-state baryons successfully. However, most of the excited states predicted in the constituent quark models have not been observed experimentally or have different masses than expected. Especially, in the energy region above $W = 1.8$ GeV, a significant number of predicted states have not been established by the experiments. Most of the observed states in first stage were found in πN scattering. During experiments involving πN scattering, the flavors of constituent quarks in the pion have an impact on the behavior of the excited nucleons. On the other hand, the photon induced reaction can couple to a $q\bar{q}$ pair including the strangeness in a few GeV energy. Here the η meson photoproduction is a good tool to study the resonances containing the strangeness. The η meson photoproduction on the proton has an advantage to search for isospin 1/2 resonances, because an η meson is isospin 0 and cannot produce intermediate states that are isospin 3/2. Moreover, the η meson contains hidden strangeness ($s\bar{s}$), so it is expected to couple to a baryon resonance with a large $s\bar{s}$ component.

We have measured the $\gamma p \rightarrow \eta p$ reaction at $E_\gamma = 1.3\text{--}2.4$ GeV to study a bump structure in the differential cross sections at $\cos\theta_{\text{c.m.}}^\eta < -0.6$ above $W = 2.1$ GeV. The experiment was carried out in the newly constructed LEPS2 beamline at SPring-8, by using a linearly polarized backward-Compton-scattering photon beam. The polarization is more than 70% above $W = 2.1$ GeV. The $\eta \rightarrow \gamma\gamma$ decay mode is used to identify the η meson. These decay products are detected by the BGOegg calorimeter and a recoil proton is detected by the BGOegg calorimeter or the DC. Event selection was performed

using kinematic fit with four-momentum conservation and energy conservation as constraints to suppress the background. The remaining background was subtracted using three background reaction templates: $\gamma p \rightarrow \pi^0 \pi^0 p$, $\gamma p \rightarrow \pi^0 \eta p$, and $\gamma p \rightarrow \omega p$, obtained from the MC simulation.

We obtained the differential cross section and photon beam asymmetries for the reaction $\gamma p \rightarrow \eta p$ in the energy range of $1.82 < W < 2.32$ GeV and the polar angle range of $-1.0 < \cos \theta_{\text{c.m.}}^\eta < 0.6$. The present analysis has achieved the precise and wide angular measurement by detecting all the final states, including a proton and an η meson which decays into $\gamma\gamma$. A bump structure above $W = 2.0$ GeV appears in the region of $\cos \theta_{\text{c.m.}}^\eta < 0$, and its strength becomes larger as the η emission angles get more backward. Similar bump structures have been observed in LEPS, CBELSA/TAPS, and CLAS results, but their strength and behaviors differ from each other. We compared our results with the Partial Wave Analysis calculations by Bonn-Gatchina2019, EtaMAID2018, SAID2009, and ANL-Osaka2016. No PWA calculations reproduce the behaviour and strength of the bump structure at η backward angles. Our results for photon beam asymmetries are consistent with other experimental results from the GRAAL, CBELSA/TAPS, and CLAS Collaborations in $W < 2.1$ GeV. In $W > 2.1$ GeV, we measured for the first time the photon beam asymmetries. No PWA calculations reproduce our experimental results and the discrepancy between the PWA results. Our data is useful to limit PWA calculations in this energy region.

We discussed the enhancement of the differential cross section at $\cos \theta_{\text{c.m.}}^\eta < -0.4$. One possibility is u -channel contribution, which is strongly enhanced at backward angle. The u -channel contribution is expected to have a smooth energy dependence from Regge theory. However, the bump-like energy dependence is seen and cannot be explained by the u -channel contribution alone. Other possibility is high-spin s -channel resonance. Since the helicity of the initial state is limited to $|h| \leq 3/2$, if an intermediate resonance has a high spin ($J \geq 5/2$), it can emit an η meson to the backward or forward polar angles in two-body decays. We compared the differential cross sections for π^0 and ω photoproduction derived from the same data set utilized in the current analysis. No visible bump structures are observed in backward angles. This observation can be attributed to the composition of the mesons within the framework of flavor

SU(3) quark models. The η meson comprises an $s\bar{s}$ quark pair, while the π^0 and ω mesons solely consist of $u\bar{u}$ and $d\bar{d}$ quark configurations. Consequently, the observed bump structure in the differential cross sections of η photoproduction is likely linked to nucleon resonances characterized by a significant $s\bar{s}$ component and a strong coupling to the ηN channel.

We have compared the model calculations in the various ranges of orbital angular momentum L . Our differential cross sections show a sharp backward rise at higher energies. By comparing this behavior with the two PWA results, EtaMAID2018 and Bonn-Gatchina2019, it is recognized that the determination of multipole contributions at $L \leq 3$ is still ambiguous in the existing PWAs and important to reproduce the data. The different determinations of multipoles in the lower L region also make a large difference in the angular dependence of calculated photon beam asymmetries. This indicates that the current understanding of resonance and born-term contributions is not enough even for lower L 's at high energies in both the PWA calculations. In addition, higher L contributions are important to accurately reproduce the measured photon beam asymmetries.

In order to investigate what might be the source of the bump structure observed in several previous measurements above $W > 2$ GeV, we precisely measured the differential cross section and photon beam asymmetry. Our experimental results suggest that this bump structure is caused by the high-spin resonances with large $s\bar{s}$ components, which strongly couple to ηN channel. Candidates for these resonances are $N(2060)5/2^-$, $N(2120)3/2^-$, $N(2190)7/2^-$, $N(2220)9/2^+$, $N(2250)9/2^-$ listed in the PDG. Information on these resonances comes from the πN -decay channel and less from the ηN -decay channel. This work provides additional constraints for the interpretation of the bump structure in the high energy region.

Acknowledgments

I would like to express the deepest appreciation to Prof. Masayuki Niiyama. He educated me for a total of thirteen years since I was a master student. His ideas and suggestions have always helped me in my research. I could not complete my doctoral thesis without his extensive support.

I am deeply grateful to Prof. Norihito Muramatsu, who is the leader of the LEPS2/BGOegg Collaboration. He provided invaluable assistance for the data analysis and carefully proofread my submitted paper.

I would like to offer my special thanks to Prof. Tomofumi Nagae. He is the leader of the Experimental Nuclear and Hadronic Physics Laboratory in Kyoto University. He gave me constructive suggestions to improve this thesis.

I appreciate Prof. Masaru Yosoi. He taught me how to handle gas chambers and various other experimental techniques. He also gave me a lot of advice on problem solving based on his vast experience.

I owe a debt to Prof. Takashi Nakano. I have learned the mindset and thinking of a researcher from him.

I want to thank Prof. Takatsugu Ishikawa. Under his guidance, I have acquired many experimental techniques and attitudes toward the physics experiment. He also advised me on my career path as a researcher.

I thank Prof. Toru Sato, and Prof. Hiroyuki Kamano for the assistance about Partial Wave Analysis calculation using ANL-Osaka2016.

I am grateful to Prof. Kirill Nikonov, and Prof. Farah Noreen Afzal. They provided many numerical data for this work.

I am indebted to all the members of the LEPS2/BGOegg Collaboration. We could successfully carry out experiment thanks to the collaborators. I especially thank Prof. Natsuki Tomida, Dr. Keigo Mizutani, Dr. Tran Hai Nam, Dr. Yuji Matsumura, Mr. Hiroto Hamano, Mr. Takuya Shibukawa, and Mr.

Ryuji Yamazaki. They performed important calibrations of detectors or some fundamental analysis for this experiment. I also thank Prof. Kenneth Hicks, Prof. Hideki Kohri, Prof. Mizuki Sumihama, Prof. Tomoaki Hotta, Prof Yuji Kato, Prof. Manabu Miyabe, Prof. Atsushi Tokiyasu, Prof. Takeshi Ohta, Dr. Yuki Yoshi Kon, Dr. Yusuke Tsuchikawa, Mr. Shintaro Tanaka, Mr. Hitoshi Katsuragawa.

I would like to acknowledge to the members of the Experimental Nuclear and Hadronic Physics Laboratory in Kyoto University.

Last but not least, I would like to thank my family for their support.

Appendix A

Helicity amplitude

Here we formulate the pseudoscalar meson photoproduction reaction using helicity amplitudes [13]. We define an amplitude A , related to the S matrix by

$$S = 1 + (2\pi)^4 i\delta^4(P_f - P_i) (8\pi W N) A, \quad (\text{A.1})$$

where $P_i = k + p_1$, $P_f = q + p_2$, and $N = (2k2\omega2E_12E_2)^{\frac{1}{2}}$. A is a spin-dependent 2×2 matrix whose column and rows refer to the initial and final nucleon spins. The elements of A are dependent on the photon polarization ε , the polar angle θ , and the total energy W .

$$A = (A_{fi}) = \begin{pmatrix} A_{\uparrow\uparrow} & A_{\uparrow\downarrow} \\ A_{\downarrow\uparrow} & A_{\downarrow\downarrow} \end{pmatrix}. \quad (\text{A.2})$$

$$\sigma_0(\theta) = \frac{1}{2} \frac{q}{k} \sum_{\text{spins}} |A_{fi}|^2 \quad (\text{A.3})$$

Once we quantize the initial and final spin along the direction of \mathbf{k} and \mathbf{q} in the c.m. system, then the elements of A are represented as the helicity amplitudes $A_{\mu\lambda}(\theta, \phi)$, where $\lambda = \lambda_k - \lambda_1$ and $\mu = \lambda_q - \lambda_2$ are the total initial and final state helicities, respectively. Since $\lambda_k = \pm 1$ for real photon and $\lambda_1 = \pm \frac{1}{2}$ for the proton, the initial state helicity λ takes the four values $+\frac{3}{2}$, $+\frac{1}{2}$, $-\frac{1}{2}$, and $-\frac{3}{2}$. Similarly, since $\lambda_q = 0$ for the meson and $\lambda_2 = \pm \frac{1}{2}$ for the proton, the final state helicity $\mu = -\lambda_2$ takes the two values $+\frac{1}{2}$ and $-\frac{1}{2}$. Combining the initial and final states allows eight helicity amplitudes $A_{\mu\lambda}$, though they are not independent. Using parity symmetry, the independent amplitudes are limited

to four, because the relationship between $A_{\mu,\lambda}$ and $A_{-\mu,-\lambda}$ is given by

$$A_{-\mu\lambda}(\theta, \phi) = -e^{i(\lambda-\mu)(\pi-2\phi)} A_{\mu\lambda}(\theta, \phi). \quad (\text{A.4})$$

If we let the four independent helicity amplitudes be $H_1, H_2, H_3,$ and H_4 with $\lambda_k = +1$ and choose $\phi = 0$ in the direction defined by the outgoing meson, then $A_{\mu,\lambda}(\theta, 0)$ is given in Table A.1. Using this formalism and Eq. A.3, the

Table A.1: Independent helicity amplitudes

		$\lambda_k = +1$		$\lambda_k = -1$	
		$+1/2$	$-1/2$	$+1/2$	$-1/2$
μ	$-\lambda_1$				
	$+1/2$	H_1	H_2	H_4	$-H_3$
	$-1/2$	H_3	H_4	$-H_2$	H_1

differential cross section for pseudoscalar meson photoproduction is represented in terms of helicity amplitudes in the following equation:

$$\sigma_0(\theta) = \frac{1}{2} \frac{q}{k} (|H_1|^2 + |H_2|^2 + |H_3|^2 + |H_4|^2). \quad (\text{A.5})$$

Thus, the differential cross sections are simply the sum of the squares of the absolute value of the helicity amplitudes.

Next we consider the asymmetry for linearly polarized incident photons. We define x and y axes of a coordinate system with z axis along \mathbf{k} and y axis along $\mathbf{k} \times \mathbf{q}$. Helicity states of the photon, $\lambda_k \pm 1$, correspond to circularly polarized photons with polarization vectors

$$\boldsymbol{\epsilon}_{\pm} = \mp \frac{1}{\sqrt{2}} (\hat{x} + i\hat{y}), \lambda_k = \pm 1. \quad (\text{A.6})$$

The polarization vectors of linearly polarized photons are oriented either perpendicular $\boldsymbol{\epsilon}_{\perp}$ or parallel $\boldsymbol{\epsilon}_{\parallel}$ to the production plane, respectively,

$$\begin{aligned} \boldsymbol{\epsilon}_{\perp} &= \hat{y} = \frac{i}{\sqrt{2}} (\boldsymbol{\epsilon}_+ + \boldsymbol{\epsilon}_-), \\ \boldsymbol{\epsilon}_{\parallel} &= \hat{x} = -\frac{1}{\sqrt{2}} (\boldsymbol{\epsilon}_+ - \boldsymbol{\epsilon}_-). \end{aligned} \quad (\text{A.7})$$

The helicity amplitudes in Table A.1 correspond to helicity states of ϵ_+ ($\lambda_k = +1$) and ϵ_- ($\lambda_k = -1$). We obtain the helicity amplitudes with linearly polarized photons given in Table A.2.

Table A.2: Helicity amplitudes for linearly polarized photons

		ϵ_\perp		ϵ_\parallel	
		$-\lambda_1$	$-\lambda_1$	$-\lambda_1$	$-\lambda_1$
$\mu = -\lambda_2$		+1/2	-1/2	+1/2	-1/2
+1/2		$\frac{i}{\sqrt{2}}(H_1 + H_4)$	$\frac{i}{\sqrt{2}}(H_2 - H_3)$	$-\frac{1}{\sqrt{2}}(H_1 - H_4)$	$-\frac{1}{\sqrt{2}}(H_2 + H_3)$
-1/2		$\frac{i}{\sqrt{2}}(H_3 - H_2)$	$\frac{i}{\sqrt{2}}(H_4 + H_1)$	$-\frac{1}{\sqrt{2}}(H_3 + H_2)$	$-\frac{1}{\sqrt{2}}(H_4 - H_1)$

The differential cross sections for linearly polarized photons σ_\perp (perpendicular) and σ_\parallel (parallel) can be obtained in the following equations:

$$\begin{aligned}\sigma_\perp(\theta) &= \frac{1}{2} \frac{q}{k} (|H_1 + H_4|^2 + |H_2 - H_3|^2), \\ \sigma_\parallel(\theta) &= \frac{1}{2} \frac{q}{k} (|H_1 - H_4|^2 + |H_2 + H_3|^2).\end{aligned}\tag{A.8}$$

The photon beam asymmetry Σ is defined as

$$\Sigma = \frac{\sigma_\perp(\theta) - \sigma_\parallel(\theta)}{\sigma_\perp(\theta) + \sigma_\parallel(\theta)}.\tag{A.9}$$

With this equation and σ_\perp and σ_\parallel from Eq. A.8, Σ is found to be

$$\begin{aligned}\Sigma &= \frac{\frac{1}{2} \left(\frac{q}{k}\right) (|H_1 + H_4|^2 + |H_2 - H_3|^2) - \frac{1}{2} \left(\frac{q}{k}\right) (|H_1 - H_4|^2 + |H_2 + H_3|^2)}{\frac{1}{2} \left(\frac{q}{k}\right) (|H_1 + H_4|^2 + |H_2 - H_3|^2) + \frac{1}{2} \left(\frac{q}{k}\right) (|H_1 - H_4|^2 + |H_2 + H_3|^2)} \\ &= \frac{q}{k} \frac{1}{\sigma_0(\theta)} \text{Re}(H_1 H_4^* - H_2 H_3^*).\end{aligned}\tag{A.10}$$

The photon beam asymmetry Σ are the interference between helicity amplitudes.

We consider the helicity amplitudes in terms of states of orbital angular momentum and parity. The partial-wave expansion of the helicity amplitude elements is expressed as follows [14].

$$A_{\mu\lambda}(\theta, \phi) = \sum_j A_{\mu\lambda}^j (2j + 1) d_{\lambda\mu}^j(\theta) e^{i(\lambda - \mu)\phi}\tag{A.11}$$

With the ϕ dependence from Eq. A.11 we can return to the elements of the A matrix in Table A.1 and include the ϕ dependence for each helicity amplitude, thus producing Table A.3.

 Table A.3: Independent helicity amplitudes with ϕ dependence

		$\varepsilon_+(\lambda_k = +1)$		$\varepsilon_-(\lambda_k = -1)$	
		$+1/2$	$-1/2$	$+1/2$	$-1/2$
μ	$-\lambda_1$	$+1/2$	$-1/2$	$+1/2$	$-1/2$
	$+1/2$	$H_1 e^{i\phi}$	H_2	$H_4 e^{-i\phi}$	$-H_3 e^{-2\phi}$
	$-1/2$	$H_3 e^{i2\phi}$	$H_4 e^{i\phi}$	$-H_2$	$H_1 e^{-i\phi}$

Combining Table A.3 and Eq. A.7 produces the ϕ -dependent helicity amplitudes for linearly polarized photons with ε_\perp and ε_\parallel , as given in Table A.4 and A.5.

 Table A.4: Helicity amplitudes with ϕ dependence for linearly polarized photons ε_\perp

		ε_\perp	
		$+1/2$	$-1/2$
$\mu = -\lambda_2$	$-\lambda_1$	$+1/2$	$-1/2$
	$+1/2$	$\frac{i}{\sqrt{2}}(H_1 e^{i\phi} + H_4 e^{-i\phi})$	$\frac{i}{\sqrt{2}}(H_2 - H_3 e^{-i2\phi})$
	$-1/2$	$\frac{i}{\sqrt{2}}(H_3 e^{i2\phi} - H_2)$	$\frac{i}{\sqrt{2}}(H_4 e^{i\phi} + H_1 e^{-i\phi})$

 Table A.5: Helicity amplitudes with ϕ dependence for linearly polarized photons ε_\parallel

		ε_\parallel	
		$+1/2$	$-1/2$
$\mu = -\lambda_2$	$-\lambda_1$	$+1/2$	$-1/2$
	$+1/2$	$-\frac{1}{\sqrt{2}}(H_1 e^{i\phi} - H_4 e^{-i\phi})$	$-\frac{1}{\sqrt{2}}(H_2 + H_3 e^{-i2\phi})$
	$-1/2$	$-\frac{1}{\sqrt{2}}(H_3 e^{i2\phi} + H_2)$	$-\frac{1}{\sqrt{2}}(H_4 e^{i\phi} - H_1 e^{-i\phi})$

We can obtain the ϕ -dependent differential cross section using this informa-

tion, as given in Eq. A.12 and A.13.

$$\begin{aligned}
\sigma_{\perp}(\theta, \phi) &= \frac{1}{2} \frac{q}{k} \sum_{\mu \varepsilon_{\perp} \text{states}} |A_{\mu \varepsilon_{\perp}}|^2 \\
&= \frac{1}{2} \frac{q}{k} (|H_1|^2 + |H_2|^2 + |H_3|^2 + |H_4|^2 + 2 \cos 2\phi \operatorname{Re}(H_1 H_4^* - H_2 H_3^*)) \\
&= \sigma_0(\theta) + \sigma_0(\theta) \Sigma \cos 2\phi \\
&= \sigma_0(\theta) (1 + \Sigma \cos 2\phi)
\end{aligned} \tag{A.12}$$

$$\begin{aligned}
\sigma_{\parallel}(\theta, \phi) &= \frac{1}{2} \frac{q}{k} \sum_{\mu \varepsilon_{\parallel} \text{states}} |A_{\mu \varepsilon_{\parallel}}|^2 \\
&= \frac{1}{2} \frac{q}{k} (|H_1|^2 + |H_2|^2 + |H_3|^2 + |H_4|^2 - 2 \cos 2\phi \operatorname{Re}(H_1 H_4^* - H_2 H_3^*)) \\
&= \sigma_0(\theta) (1 - \Sigma \cos 2\phi)
\end{aligned} \tag{A.13}$$

So far, we assumed that the polarization of the photon beam was 100%. Since the polarization is less than 100% in real experiments, so a multiplicative factor of P_{γ} has been introduced.

$$\begin{aligned}
\sigma_{\perp}(\theta, \phi) &= \sigma_0(\theta) (1 + P_{\gamma} \Sigma \cos 2\phi), \\
\sigma_{\parallel}(\theta, \phi) &= \sigma_0(\theta) (1 - P_{\gamma} \Sigma \cos 2\phi).
\end{aligned} \tag{A.14}$$

Finally, the relationship between CGLN amplitudes (F_1, F_2, F_3, F_4) and helicity amplitudes (H_1, H_2, H_3, H_4) is shown below.

$$H_1(\theta, \phi) = -\frac{1}{\sqrt{2}} e^{i\phi} \sin \theta \cos \frac{1}{2} \theta (F_3 + F_4) \tag{A.15}$$

$$H_2(\theta, \phi) = \sqrt{2} \cos \frac{1}{2} \theta \{ (F_2 - F_1) + \frac{1}{2} (1 - \cos \theta) (F_3 - F_4) \} \tag{A.16}$$

$$H_3(\theta, \phi) = \frac{1}{\sqrt{2}} e^{i\phi} \sin \theta \sin \frac{1}{2} \theta (F_3 - F_4) \tag{A.17}$$

$$H_4(\theta, \phi) = \sqrt{2} e^{i\phi} \sin \frac{1}{2} \theta \{ (F_1 + F_2) + \frac{1}{2} (1 + \cos \theta) (F_3 + F_4) \} \tag{A.18}$$

Appendix B

SPring-8 filling pattern

We summarize the several electron filling patterns at SPring-8 in the present experimental period [33]. We show illustrations of each bunch mode in Fig. B.1.

Table B.1: Several filling patterns in the second half of 2014.

Mode	Bunch mode	Bunch interval
A	203 bunches	23.6 ns
C	11 bunch train \times 29	145.5 ns
F	1/14-filling + 12 bunches	342 ns
H	11/29-filling + 1 bunch	1486 ns

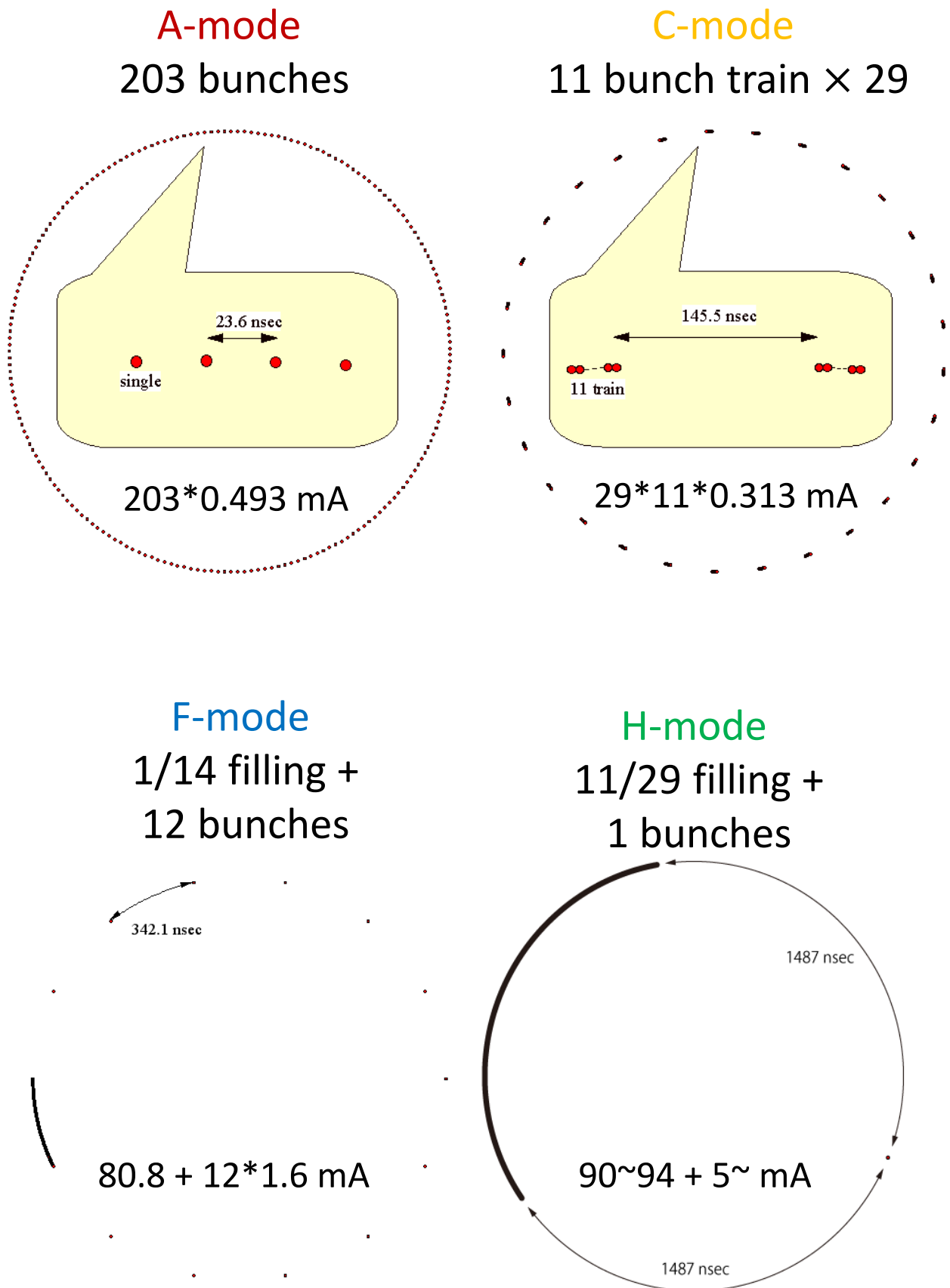


Figure B.1: Several electron filling pattern in the second half of 2014.

Appendix C

Dead time correction

The tagger scaler has dead time because of finite signal width (20 ns), so the tagger counting efficiency depended on the tagger rate and electron filling pattern. The dead time correction factors depending on tagger rate are simulated in each filling pattern and are fitted with the 4th polynomial function. These results are shown in Fig. C.1.

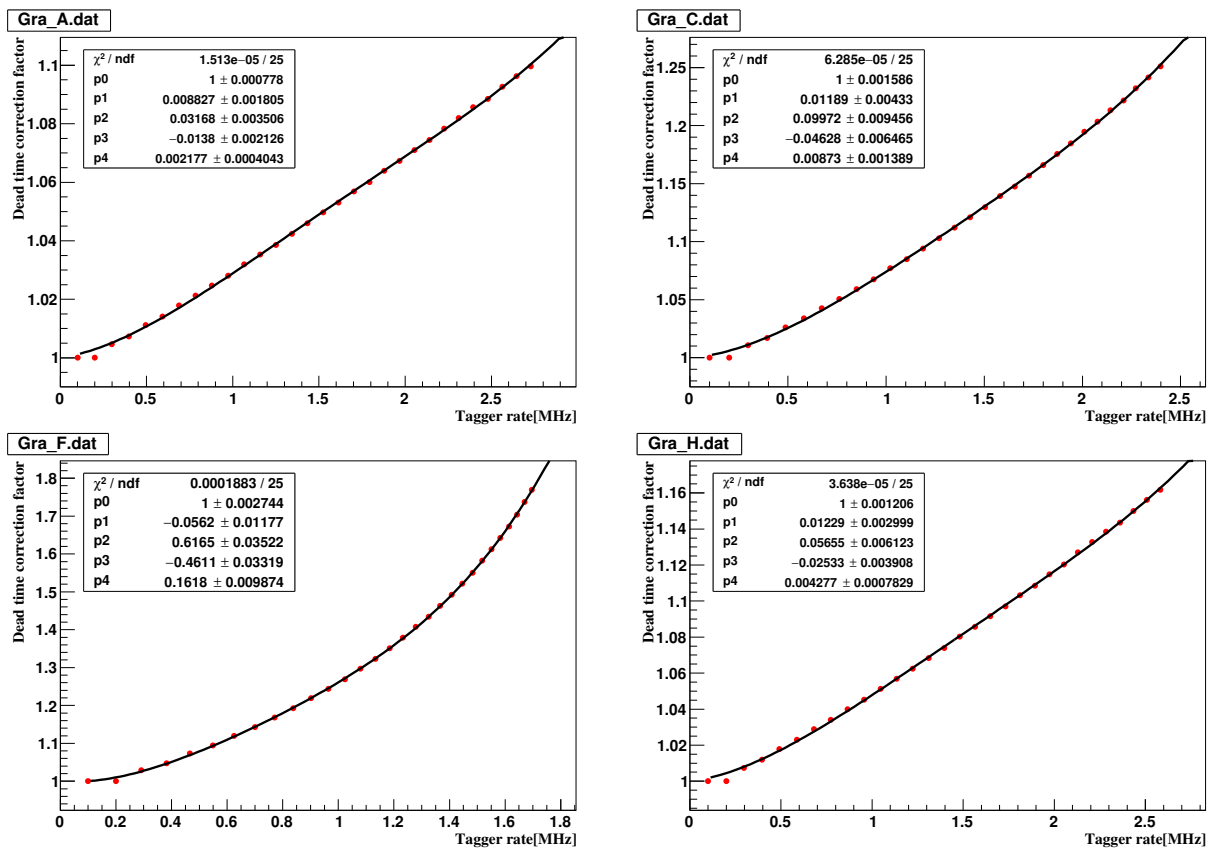


Figure C.1: The dead time correction function using 20 ns width in each filling pattern.

Appendix D

Photon energy measurement

We determined the energy of the photon beam by analyzing the recoil electrons produced by backward Compton scattering. The relationship between the photon beam energy and the position of the tagger fiber hits was evaluated using equations 3.2 and 3.2. These equations were derived by simultaneously fitting the expected photon energy for various reactions: (a) $\gamma p \rightarrow 2\pi^0 + p$, (b) $\gamma + p \rightarrow \pi^0/\eta + p_f$, and (c) the maximum photon beam energy, using data obtained from the liquid hydrogen target. In this analysis, the detection of π^0 , η , and p were detected using the BGOegg calorimeter and p_f was detected using the RPC. For the analysis of the reaction (a), a kinematic fitting technique was employed to evaluate the expected photon beam energy. For the analysis of the reaction (b), the missing mass of the $p(\gamma, p_f)$ reaction was calculated, and the photon energy corresponding to the mass of an π^0 or η meson was estimated. For the analysis of (c), the maximum photon beam energy was calculated to be 2.385 GeV, known as the Compton edge, and the tagger fiber number associated with the entries at the Compton edge was identified.

To evaluate the resolution of the photon energy, we utilized the $\gamma + p \rightarrow \pi^0\eta p_f$ reaction with the liquid hydrogen target. The photon beam energy was predicted through kinematic fitting using the measured momenta of η , π^0 , and p_f . The standard deviation of the difference between the measured and predicted photon beam energy was determined to be 16.8 ± 0.9 MeV. Additionally, a MC simulation was employed to estimate the contribution of detector resolu-

tion, which was found to be 11.8 ± 0.2 MeV. Subtracting the detector resolution, the photon beam energy resolution was estimated to be 12.0 ± 0.7 MeV.

Appendix E

Efficiencies

E.1 Tagger reconstruction efficiency

The tagger reconstruction efficiency was obtained from $\gamma + p \rightarrow \pi^0 + \pi^0 + p$ reaction with the liquid hydrogen target. We used kinematic fitting with the constraints by the two π^0 mass and the four-momentum conservation. The photon beam energy was treated as an unmeasured variable. These efficiencies are listed in Table E.1.

Table E.1: Tagger reconstruction efficiency

Total energy region	tagger reconstruction efficiency
$1.82 < W < 1.87$ GeV	0.8560 ± 0.0057
$1.87 < W < 1.92$ GeV	0.9199 ± 0.0052
$1.92 < W < 1.97$ GeV	0.8671 ± 0.0055
$1.97 < W < 2.02$ GeV	0.8876 ± 0.0057
$2.02 < W < 2.07$ GeV	0.9058 ± 0.0059
$2.07 < W < 2.12$ GeV	0.8743 ± 0.0062
$2.12 < W < 2.17$ GeV	0.8910 ± 0.0064
$2.17 < W < 2.22$ GeV	0.8985 ± 0.0068
$2.22 < W < 2.27$ GeV	0.8881 ± 0.0071
$2.27 < W < 2.32$ GeV	0.9244 ± 0.0085

E.2 Shower contribution

At the calculation of integrated photon beam flux, the tagger trigger counts are basically utilized. However, we know there is the shower contribution due to the

recoil electron hit to the beamline structure between the electron beam and the tagger. This amount was estimated from the special data which was taken with the lead glass counter, which was used to directly measure the photon beam energy. The template spectra for a BCS photon beam and a shower contribution were prepared for the template fit to separate them. The BCS photon spectrum was made by the MC simulation with the well-known Compton cross sections. The lower edge of the spectrum was cut off at 1268 MeV, corresponding to the edge of the tagger fiber forward layer. The energy resolution of the lead glass counter was estimated to be 129.4 MeV by the error function fit at the Compton edge, and the above BCS photon spectrum was smeared with this energy resolution. The template spectrum for the shower contribution was obtained from the lead glass data by requiring the tagger PL hits which are coincident at the corresponding forward and backward layers. A function with a Gaussian and a second order polynomial was fitted to the region below the tagger acceptance. The shower contribution was clearly observed at 1143.6 MeV with $\sigma = 82.9$ MeV. The Gaussian component was defined as the template spectrum of the shower contribution. The obtained template spectra for the BCS photon and shower components were fitted to the energy distribution of the lead glass data. At the template fit, the spectrum for the bremsstrahlung component was simultaneously fitted. The fraction of the shower contribution was estimated to be 0.0424 ± 0.0006 . This fraction was used to remove the shower contribution from the integrated tagger counts.

E.3 IPS proton detection efficiency

When protons are detected by BGOegg, IPS partly has no hits because of small energy deposits or slow timing. These events were identified as a neutral cluster by IPS. We evaluated the IPS proton detection efficiency using the $\gamma + p \rightarrow \eta + p$ reaction with the liquid hydrogen target. We used kinematic fitting without charge identification at IPS. The two γ 's combination with the maximum energy sum was treated as an η candidate and the remained cluster was assumed as a proton. The detection efficiency was the fraction of clusters assumed to be protons that are charged clusters. The IPS proton detection efficiency was estimated to be 0.9851 ± 0.0006 .

E.4 DC track reconstruction efficiency

The proton detection inefficiency at DC is caused by the events failed by the χ^2 probability cut for the DC track reconstruction. We evaluated the DC track reconstruction efficiency using the $\gamma + p \rightarrow \omega + p$ reaction with the liquid hydrogen target. We used kinematic fitting and required that the proton angle to be in the DC acceptance. The DC tracking efficiency was estimated to be 0.9824 ± 0.0044 . Not only the proton detection efficiency but also the overveto rate to be considered because DC has no timing resolution for the charged track detection. The tracks from different bunches, especially due to e^+e^- conversions, can be recorded simultaneously. In order to estimate this overveto rate, π^0 events were analyzed with the kinematic fitting, where all the DC track candidates were examined to estimate this overveto rates. The overveto efficiency at DC was estimated to 0.9804 ± 0.0010 . This value was treated as a correction factor for proton detection efficiency at DC.

E.5 RPC reconstruction efficiency

We evaluated the RPC reconstruction efficiency using the $\gamma + p \rightarrow \eta + p$ reaction with the liquid hydrogen target. We used kinematic fitting and required a track of proton in the DC and RPC acceptance. We obtained the RPC reconstruction efficiency to be 0.9589 ± 0.0232 .

Bibliography

- [1] David J. Gross and Frank Wilczek Phys. Rev. Lett. **30**, 1343 (1973).
- [2] M. Tanabashi *et al.* [Particle Data Group], Phys. Rev. D **98**, no.3, 030001 (2018).
- [3] F. Bulos *et al.*, Phys. Rev. Lett. **13**, 486 (1964).
- [4] R. Prepost, D. Lundquist, and D. Quinn, Phys. Rev. Lett. **18**, 82 (1967).
- [5] C. Bacci *et al.*, Phys. Rev. Lett. **20**, 571 (1968).
- [6] C. DeTar and J. Kogut, Phys. Rev. Lett. **59**, 399 (1987).
- [7] B. S. Zou, Nucl. Phys. A **790**, 110c (2007).
- [8] L. David Roper, Phys. Rev. Lett. **12**, 340 (1964).
- [9] Zhenping Li, Volker Burkert, and Zhujun Li, Phys. Rev. D **46**, 70 (1992).
- [10] O. Krehl, C. Hanhart, S. Krewald, and J. Speth, Phys. Rev. C **62**, 025207 (2000).
- [11] N. Suzuki, B. Juliá-Díaz, H. Kamano, T. S. H. Lee, A. Matsuyama and T. Sato, Phys. Rev. Lett. **104**, 042302 (2010).
- [12] G.F. Chew, M.L. Goldberger, F.E. Low, and Y. Nambu, Phys. Rev. **106**, 1345 (1957).
- [13] R. L. Walker, Phys. Rev, **182**, 1729 (1969).
- [14] M. Jacob and G. C. Wick, Annals Phys. **7**, 404–428 (1959).
- [15] P. A. Zyla *et al.* [Particle Data Group], PTEP **2020**, no.8, 083C01 (2020).

- [16] F. Renard *et al.*, Phys. Lett. B **528**, 215 (2002).
- [17] V. Crede *et al.*, Phys. Rev. Lett. **94**, 012004 (2005).
- [18] B. Krusche, J. Ahrens, G. Anton, R. Beck, M. Fuchs, A. R. Gabler, F. Harter, S. Hall, P. Harty and S. Hlavac, *et al.* Phys. Rev. Lett. **74**, 3736–3739 (1995).
- [19] M. Dugger *et al.*, Phys. Rev. Lett. **89**, 222002 (2002).
- [20] M. Sumihama, *et al.*, Phys. Rev. C **80**, 052201 (2009).
- [21] D. Elsner, *et al.*, Eur. Phys. J. A **33**, 147 (2007).
- [22] L. Tiator, *et al.*, Eur. Phys. J. A **54**, 210 (2018).
- [23] CBELSA/TAPS Collaboration (J. Müller, *et al.*), Phys. Lett. B **803**, 135323 (2020).
- [24] "Spring-8 web site", <http://www.spring8.or.jp/en/>
- [25] A. D'Angelo, O. Bartalini, V. Bellini, P. Levi Sandri, D. Moricciani, L. Nicoletti and A. Zucchiatti, Nucl. Instr. Meth. A455 (2000) 1.
- [26] N. Muramatsu, *et al.*, Nucl. Instr. Meth. A **737**, 184 (2014).
- [27] N. Muramatsu, *et al.*, Nucl. Instr. Meth. A **1033**, 166677 (2022).
- [28] T. Ishikawa, *et al.*, Nucl. Instr. Meth. A **837**, 109 (2016).
- [29] N. Tomida, *et al.*, JINST **9**, C10008 (2014).
- [30] N. Tomida, *et al.*, JINST **11**, C11037 (2016).
- [31] I. Nagasawa *et al.*, ELPH annual report 2011–2013, 194 (2013).
- [32] T. Ishikawa *et al.*, ELPH annual report 2011–2013, 175 (2013).
- [33] https://www.spring8.or.jp/ja/users/operation_status/schedule/bunch_mode_b14/

- [34] S. Agostinelli, *et al.*, Nucl. Instr. Meth. A **506**, 250 (2003); J. Allison, *et al.*, IEEE Trans. Nucl. Sci. **53**, 270 (2006).
- [35] M. Williams, *et al.*, Phys. Rev. C **80**, 045213 (2009).
- [36] V. Crede, *et al.*, Phys. Rev. C **80**, 055202 (2009).
- [37] <https://maid.kph.uni-mainz.de/eta2018/etamaid2018.html>
- [38] <https://gwdac.phys.gwu.edu/>
- [39] <https://pwa.hiskp.uni-bonn.de/>
- [40] H. Kamano, S. X. Nakamura, T-S H. Lee, and T. Sato, Phys. Rev. C **94** 015201 (2016).
- [41] Private communication with T. Sato.
- [42] O. Bartalini, *et al.*, Eur. Phys. J. A **33**, 169 (2007).
- [43] O. Bartalini, *et al.*, Eur. Phys. J. A **26**, 399 (2005).
- [44] P. Collins, *et al.*, Phys. Lett, B **771**, 213 (2017).
- [45] F. Afzal, *et al.*, Phys. Rev. Lett. **125**, 152002 (2020).
- [46] D. Rönchen, *et al.*, Eur. Phys. J. A **51**, 70 (2015).
- [47] P.D.B. Collins, *An Introduction to Regge Theory and High Energy Physics*, Cambridge, Univ. Press. (1977).
- [48] J.K. Storrow, Rep. Prog. Phys. **50**, 1229, (1987).
- [49] J.M. Laget, Prog. Part. Nucl. Phys. **111**, 103737 (2020).
- [50] C.G. Fasano, Frank Tabakin, and Bijan Saghai, Phys. Rev. C **46** 2430 (1992).
- [51] N. Muramatsu, *et al.*, Phys. Rev. C **100**, 055202 (2019).
- [52] N. Muramatsu, *et al.*, Phys. Rev. C **102**, 025201 (2020).

- [53] A.V. Anisovich, R. Beck, E. Klempt, V.A. Sarantsev, U. Thoma, Eur. Phys. J. A **48**, 88 (2012).
- [54] A.M. Sandorfi, S. Hoblit, H. Kamano, and T-S. H. Lee, J. Phys. G: Nucl. Part. Phys. **38**, 053001 (2011).
- [55] S. Capstick and W. Roberts, Prog. Part. Nucl. Phys. **45**, S241 (2000).
- [56] Barker I S, Donnachie A and Storrow J K, Nucl. Phys. B **95** 347 (1975).
- [57] Donnachie A and Shaw G, Appl. Phys. **37** 333 (1966).
- [58] Drechsel D and Tiator L, J. Phys. G: Nucl. Part. Phys. **18** 449 (1992).
- [59] Knöchlein G, Drechsel D and Tiator L, Z. Phys. A **352** 327 (1995).
- [60] D. Elsner, *et al.*, Eur. Phys. J. A **39**, 373 (2009).
- [61] K. Livingston, CLAS note 2011-020, <https://misportal.jlab.org/ul/Physics/Hall-B/clas/viewFile.cfm/2011-020.pdf?documentId=656> (unpublished).
- [62] T. Nakano, *et al.*, Phys. Rev. Lett **91**, 012002 (2003).
- [63] R. Aaji, *et al.*, Phys. Rev. Lett **115**, 072001 (2015).
- [64] S. -K. Choi, *et al.*, Phys. Rev. Lett **91**, 262001 (2003).